FIBER OPTIC SENSORS FOR EXTREME ENVIRONMENTS

by

Tong Chen

B.S. in Physics, Nanjing University, 2002

M.S. in Physics, University of Pittsburgh, 2006

Submitted to the Graduate Faculty of

Swanson School of Engineering in partial fulfillment

of the requirements for the degree of

Doctor of Philosophy

University of Pittsburgh

2012

UNIVERSITY OF PITTSBURGH

SWANSON SCHOOL OF ENGINEERING

This dissertation was presented

by

Tong Chen

It was defended on

March 28, 2012

and approved by

Sung Kwon Cho, PhD, Associate Professor, Department of Mechanical Engineering and

Material Science

Mahmoud El Nokali, PhD, Associate Professor, Department of Electrical and Computer

Engineering

Guangyong Li, PhD, Assistant Professor, Department of Electrical and Computer Engineering

Minggui Sun, PhD, Professor, Department of Electrical and Computer Engineering

Dissertation Director: Kevin P. Chen, PhD, Associate Professor, Department of Electrical

and Computer Engineering

FIBER OPTIC SENSORS FOR EXTREME ENVIRONMENTS

Tong Chen, Ph.D.

University of Pittsburgh, 2012

Optical fiber based sensors offer several important advantages over electronic sensors, including low manufacturing cost, miniature and flexible structures, immunities to electromagnetic fields, and the capability of distributive and multi-parameter sensing on a single fiber. Extreme harsh environments such as temperature >800°C or as low as a few Kelvin, present unique challenges and opportunities to fiber optic sensors. For example, hydrogen gas leak detection in cryogenic environment is critically important in the production and use of liquid hydrogen fuels. But the sensitivity of conventional Palladium (Pd) coated hydrogen sensors degrade rapidly when temperature decreases. Another example is the quick diminishing of conventional type-I gratings with temperature range beyond 500°C, which prevent the FBG implementation in numerous high temperature applications.

The objective of this thesis is to explore new fiber sensing technologies that have significant performance enhancements, or were previously not possible in extreme environment applications. Optically heated fiber sensors were developed for cryogenic Hydrogen gas and liquid level sensing in environments as well as room temperature gas flow sensing. Regenerated gratings were developed for high temperature pressure sensing. Novel in-fiber sensing techniques such as Rayleigh and Raman scattering were also exploited for fully distributed sensing operations. These technologies and devices offer reliable and flexible sensing solutions extreme environments in energy, transportation and telecom industry.

TABLE OF CONTENTS

LIST OF FIGURES

ACKNOWLEDGEMENTS

Firstly, I would like to thank Dr. Kevin Chen for funding the entire work. I have learned tremendous from him in the field of photonics, both in theory and experimental techniques. Without his guidance, none of these would be possible. I would also like to thank Dr. Sun Kwon Cho from department of mechanical engineering, Dr. Mahmoud El Nokali, Dr. Guangyong Li and Dr. Minggui Sun of our department for agreeing to join my Ph.D proposal committee.

I would also acknowledge my colleagues in Kevin's group, Michael Buric, Rongzhang Chen, Dr. Baojun Liu, Ben McMillen, Dr. Chuck Jewart, Qingqing Wang, Dr. Di Xu and Dr. Botao Zhang, for the great help in our collaborations and for maintaining such a good research environment inside our group. Special thanks to our worldwide collaborators, Dr. Phil Swinehart and Dr. Mokhtar Maklad from Lakeshore Cryotronics, Fei Ye and Dr. Li Qian from University of Toronto, Dr. Ping Lu and Dr. Qiying Chen from Memorial University of Newfoundland, Eric Lindner from IPHT Germany and Dr. Kevin Cook and Dr. John Corning from University of Sydney. Finally, I would thank my parents and my beloved wife Chenjie for just being there.

1.0   INTRODUCTION

Optical fiber as the lightwave guiding media has been proposed and developed since '60s. But it is not until '80s that the first silica based low-loss fiber was fabricated for optical communication system. Since then, there has been an explosive development in fiber optical communication and fiber based lightwave system has become the backbone for the "information age". On the other hand, fiber optical components such as fiber Bragg gratings (FBGs) and fiber interferometers have also found wide applications in the field of optical sensing. Compared with their traditional electronic counterparts, fiber Optic Sensors (FOS) offers several key advantages. They are immune to radiation and electromagnetic interferences, chemically inert and spark free. The miniaturized sizes, low transmission loss of optical fiber, and the existing low-cost fiber components in telecom industry make FOS feasible for remote and distributed sensor network operations. Most importantly, a large number of FOSs can be multiplexed on a single piece of fiber and interrogated with a single unit to perform distributed, multi-parameter sensing. Compared with distributed multipoint using electronic sensors, this optical multiplexing technology greatly reduced the costs and implementation efforts with excessive electrical wiring.

There have been a lot of efforts in developing FOSs for harsh environments due to the excellent properties of silica fiber in the last few years. Of particular interests are extreme temperatures. Low temperature environments present numerous challenges to existing sensing technologies. The performances of room temperature sensors, such as sensitivities, response

1

times, and lifetime degrade rapidly when temperature gets lower. For example, Palladium (Pd) is the most widely adopted sensing material for hydrogen leakage detection. However, the kinetics of Palladium-hydrogen absorption slows down significantly as temperature drops. Another example would be for liquid condition monitoring, in which the discrimination between cryogenic liquid and gas phase became extremely difficult due to the small index difference between cryogenic gas and liquid. Local heating techniques such as electrical heating have been applied to enhance the ambient temperature for the sensor to enjoy its room temperature performances. However, electrical heating of FOS are not permitted in situations such as the storage and transportation of flammable and explosive liquids such as liquid hydrogen. Other issues with electrical heating include liquid conductivity and chemical corrosion. More importantly, the advantages of all-optical fiber sensing cannot be fully exploited with the compromising of electrical heating approach. As a part of this dissertation, we introduced an original all-optical heating technique based on high attenuation fibers (HAFs). All-fiber operations of hydrogen sensors, liquid level sensors and gas flow sensors are demonstrated for a wide range of temperatures. Both grating based point sensors and Rayleigh scattering based fully distributed sensors were presented.

High temperature pressure sensing is a challenging but indispensible task for a wide spectrum of applications in energy and aerospace industries. They play critical role to ensure safe and efficient operations of fossil-fuel and nuclear power generation systems. The rapid diminishing of conventional type-I FBG limited the implementation of the most powerful and widely adopted sensing device in high temperature applications. Here we successfully regenerated high temperature resisted type I grating in pressure sensitive twin-hole microstructure fibers and demonstrate the capability of measuring pressure and temperature

2

simultaneously in 24-800°C for 0-2400 psi. In-fiber Rayleigh scattering technique were also employed with microstructure fiber for high temperature pressure sensing.

The accurate measurement of gas concentrations in combustion processes ensures high efficiency and safe operation of power plant and engines. Coherent Anti-stoke Raman Spectroscopy (CARS) is a powerful tool to determine both the gas concentrations and temperature with enhanced sensitivities. Traditional CARS technique requires the spatial and temporal overlapping of the pump, probe and Stokes beams to ensure efficient generation of the anti-Stoke signal. In the last part of this dissertation, we combine hollow core photonic crystal fiber and the pulse shaping technique of broadband ultrafast laser pulse to present for the first time some preliminary results of in-fiber single beam CARS measurement for gas sensing.

The thesis is organized as following.

Chapter 2 introduces the basic operating principles for major fiber optic sensing techniques including fiber Bragg gratings (FBGs), fiber interferometers, in-fiber Rayleigh backscattering and in-fiber Coherent Anti-stoke Raman Spectroscopy (CARS).

Chapter 3 focuses on low temperature hydrogen gas sensors. First, a Pd-coated FBG sensor inscribed in high attenuation fibers (HAFs) is reported for low temperature Hydrogen gas detection. This new design with HAFs shows high heating efficiencies and great flexibilities for sensor multiplexing. It also eliminates the local hot spots and heating un-uniform with previous in-fiber self-heating design. Fast detection of Hydrogen concentrations from 0.5% to 10% is demonstrated at -50°C, -100°C and -150°C. Secondly, preliminary results on full distributed hydrogen sensing were reported using in-fiber Rayleigh scattering with electrically heated Pd-coated fiber without the need for grating inscription.

In chapter 4 of this thesis, liquid level sensing were performed with three different sensor designs. Firstly, we present one of the simplest fiber based level sensors, with two fiber tapers forming a Mach-Zehnder interferometer sensitive to the ambient refractive index changes. Then we present an Al-coated FBG sensor array inscribed in HAF for cryogenic liquid level sensing. An array of four FBGs with different Bragg wavelength, and another array of three FBGs with overlapping Bragg wavelength are presented, and the test results are reported in liquid nitrogen (LN2) at 77K. Finally, Rayleigh scattering based continuous level sensing were demonstrated using both electrical and optical heated fiber for both liquid nitrogen at 77K and liquid helium at 4.2K.

An all-fiber gas flow sensor was introduced in chapter 5 using self-heated fiber and in-fiber Rayleigh scattering. A single piece of metal coated fiber were bent into a 4 layer grid and heated with electrical current. The gas-flow-induced heat loss on each section of the grid was analyzed to determine the local flow velocity vector. And the information from all sections were synthesized together to get a comprehensive 3-D pictures of the measured gas flows.

Chapter 6 focused on high temperature sensing. Thermal regenerated FBGs in twin-hole fiber were demonstrated for simultaneous measurements of temperatures from 25-800°C and pressure from 15-2400 psi. Both polarization-maintained all-silica photonic crystal fiber and twin-hole fiber were investigated as the pressure sensing elements using frequency domain Rayleigh scattering techniques.

Preliminary results of single-beam in-fiber CARS measurement were reported for gas sensing in Appendix A. Chapter 7 summarized the dissertation.

4

2.0   SENSING PRINCIPLES

In the past 20 years, the inventions, developments and implementations of fiber optic devices have revolutionized not only the telecommunication industry, but also people's daily life. Meanwhile, fiber optic sensor technology also benefit from the decreasing costs and improving performances of telecom fiber optic components. Compared with conventional electronic base sensors, fiber optic sensors has many advantages, including low manufacturing loss and miniature size, immunity to electromagnetic fields (IMFs), multiplexible capability and large bandwidth, and potentials of working in harsh environments such as high and low temperature, IMF interferences and corrosive environments. In this chapter, we are going to introduce the principles of two major workhorses of fiber optic sensors, fiber Bragg gratings (FBGs) and fiber interferometers. And in the last portion of the chapter, more advances fiber sensing techniques, i.e., in-fiber Rayleigh scattering, and in-fiber Raman scattering and their unique potentials of working under harsh environments will also be introduces.

2.1   FIBER BRAGG GRATING SENSORS

The photosensitivity and Bragg grating in optical fiber was first discovered by Ken Hill *et al.* [1] in 1978, when the reflection of light launched into an optical fiber was found to increase over time. A refractive index Bragg grating was written in the core of the fiber due to the standing

wave intensity pattern between two ends of the fiber. It was later determined that the photosensitivity was related with two-photon absorption of the visible laser radiation. In 1989, Gerry Meltz *et al.* first demonstrated the technique of holographic writing of fiber Bragg grating (FBG) with single-photon absorption from a 244nm laser [2]. Compared with Hill's internal writing, the gratings were inscribed from side, and the Bragg wavelength can be tuned with the two interference light beams. Numerous efforts were made since then to improve the index modulation and functionality of FBGs, including using phase mask, point by point writing and thermal polings. Lemarie et al. [3] discovered that hydrogen loading was essential for the "photosensitization" of conventional optical fibers. With hydrogen pre-loading, UV excimer lasers and phase mask, FBG with index modulation $>10^{-4}$ and reflectivity $> 99.9\%$ can be readily made nowadays in both optics research labs and photonic industry.

After this brief history of FBG, the principles of photosensitivity and FBG are presented in the next part of the section, followed by different FBG fabrication techniques. Facilities and results from our research lab are introduced in the last section.

The induced polarization in a nonlinear medium can be described by,

$$D = \varepsilon_0 E + P = \varepsilon_0 \left(E + \chi^{(1)} E + \chi^{(2)} E^2 + \chi^{(3)} E^3 + \cdots \right) \tag{2.1}$$

Where the linear permittivity is,

$$\varepsilon_r = 1 + \chi^{(1)} \tag{2.2}$$

So the refractive index can be related to the linear and nonlinear permittivity as,

$$\frac{D}{\varepsilon_0 E} = \varepsilon_r + \Delta\varepsilon = n^2 = (n_0 + \Delta n)^2 \approx n_0^2 + 2n_0\Delta n \tag{2.3}$$

And the index change can be described with the induced electric field as,

$$\Delta n = \frac{1}{2n_0} \left(\chi^{(2)} E + \chi^{(3)} E^2 + \cdots \right) \tag{2.4}$$

In glass fiber (fused silica),

6

$$\chi^{(2)} = 0 \tag{2.5}$$

And with a moderate $\chi^{(3)} \sim 10^{-22} m^{-2} V^{-2}$, large internal change deposition is needed for a significant refractive index change, which can be conveniently induced by strong external electrical field, as in fiber poling methods, or by the defects in glass (SiO_2). A more direct pathway between the defects and the refractive index modulation is through the Kramers-Kronig model.

For the GeO defect in glass, an oxygen atom is missing and the Germania atom has an extra dangling bond with adjacent Si/Ge atom. The bond has an absorption peak at 240-nm. Once the bond is broken with UV radiation, free electron can be release and the molecule can be reconfigured, which possibly causes the change of refractive index. The concentration of defects in Ge doped Silica fiber can be increased with different methods, including boron and tin co-doping, and hydrogenation, in which the highest UV inscribed refractive index modulation was reported [3]. With the presence of hydrogen molecules in Ge doped silica, the formation of hydroxyl ions (Si-OH and Ge-OH) and GeH can be greatly stimulated, which accordingly changes the local refractive index.

When the refractive index modulation happens periodically along the optical fiber core, a Bragg grating is formed, the resonance wavelength of which is given by the expression,

$$\lambda_B = 2n_{eff}\Lambda \tag{2.6}$$

Where n_{eff} is the effective index of the fiber core and Λ is the grating pitch. When a spectrally broadband light is transmitted through the FBG, light component of the Bragg wavelength is reflected. The reflectivity is related to the coupling coefficient, as,

$$\kappa_{ac}L = tanh^{-1}\left(\sqrt{R}\right) \tag{2.7}$$

And the bandwidth of the reflective component, as defined by the spectral spacing between first zeros (FWFZ) is related to the grating length, as,

$$2\Delta\lambda = \frac{\lambda^2}{\pi n_{eff}L}\sqrt{(\kappa_{ac}L)^2 + \pi^2} \qquad (2.8)$$

And the refractive index modulation can also be calculated from fringe visibility and the coupling coefficient, as,

$$\kappa_{ac} = \frac{\pi v \Delta n}{\lambda} \qquad (2.9)$$

According to the above equations, a very weak 4-mm-long FBG with refractive index modulation of merely 10^{-7} can be readily detected with a 0.1nm resolution Optical Spectrum Analyzer (OSA). The reflection peak would be >20dB high from the noise floor. For a strong 4-mm-long grating with refractive index modulation $>10^{-4}$, the reflection at Bragg wavelength is approaching 100%. The FBG strength can be determined by the corresponding spectral dip in the transmission measurement. For example, a 30-dB dip means 99.9% reflection.
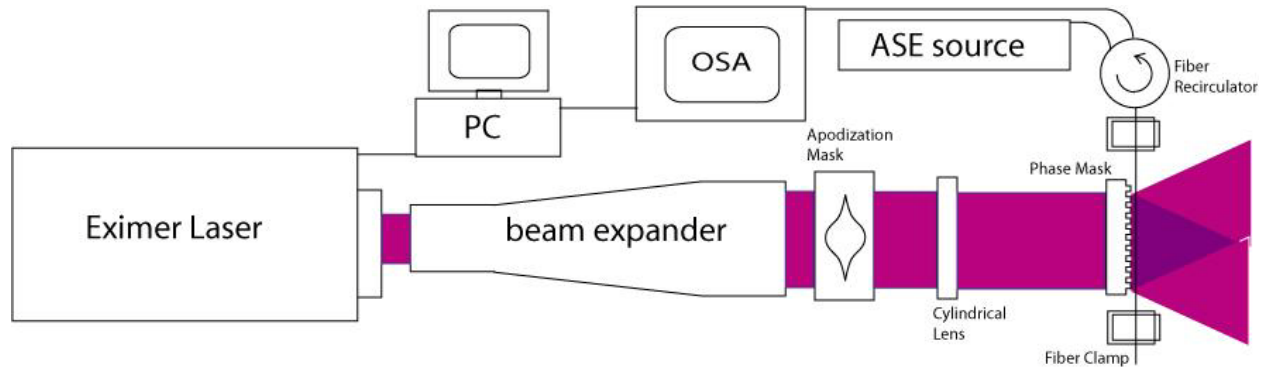
Figure 2.1 The schematic of FBG fabrication setup.

The most simple and reliable method for FBG fabrication is the phase mask interference method. As shown in figure 2.1, for the phase mask a one dimensional grating is inscribed onto a glass plate. 1070nm grating pitch is chosen for 1550nm Bragg grating in glass fiber with refractive index of 1.46. The angle of the phase mask grating is designed such that it maximizes the ±1st order diffraction and minimizes the zero's and higher order. The 193nm or 248nm UV

8

radiation from an Excimer laser passes through the phase mask, and projects ±1st order diffraction interference pattern onto a piece of photosensitive fiber. As was shown from the above equations, the Bragg wavelength is determined by the phase mask pitch and refractive index of the fiber core. The intensity and linewidth of the FBG is determined by the FBG length and fringe visibility.

Figure 2.1 shows the schematic of our FBG fabrication setup and Figure 2.2 shows the actual apparatus we built in our lab. A GSI Lumonics Pulse Master 244 laser is controlled with a personal computer and produces up to 1.2J laser pulse at 248 nm at a repetition rate up to 50 Hz. The laser beam is expanded and passes through multiple spatial mask to optimize the beam quality. A cylindrical lens focuses the beam onto the photosensitive fiber, which is clamped onto a 6-axis stage behind the phase mask. The cylindrical lens, phase mask and fiber has to be aligned perpendicular to the beam axis. The spacing between phase mask and fiber is monitored with a CCD camera mounted overhead, as shown in figure 2.2. The bottom left inset picture in figure 2.2 shows the interference pattern of between the +1 and -1 order diffraction of the phase mask during FBG writing. The real time reflection spectrum of the FBG is monitored with an ASE broadband light source and an OSA behind a fiber recirculator, and automated with a personal computer.

Figure 2.3 shows the transmission and reflection spectra of a strong FBG written in our lab. The Corning SMF-28 fiber was loaded in Hydrogen gas chamber at 2000 psi for 2 weeks, and then exposed to 248nm Excimer laser radiation with repetition rate of 25Hz, pulse energy of 300mJ, and pulse duration of approximately 2ns, for 20 minutes. The FBG is then annealed at 120°C for 24 hours for stabilization. The resulting FBG has a transmission dip of 30dB below the broadband background, which corresponds to reflection >99.9%.
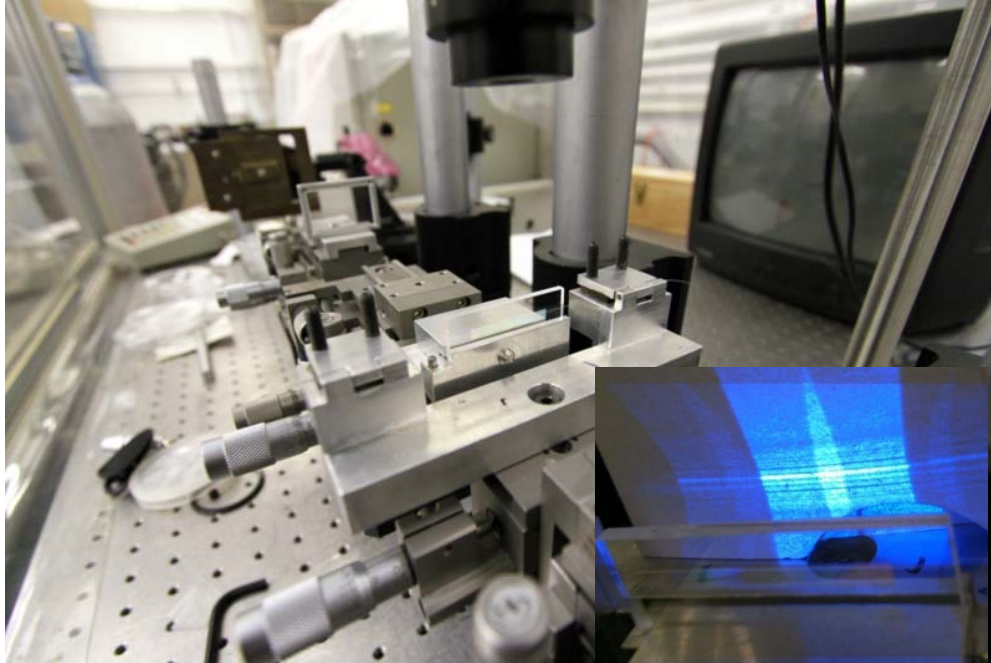
Figure 2.2 The picture of our FBG fabrication setup

The inset picture shows the interference pattern of between the +1 and -1 order diffraction of the phase mask.
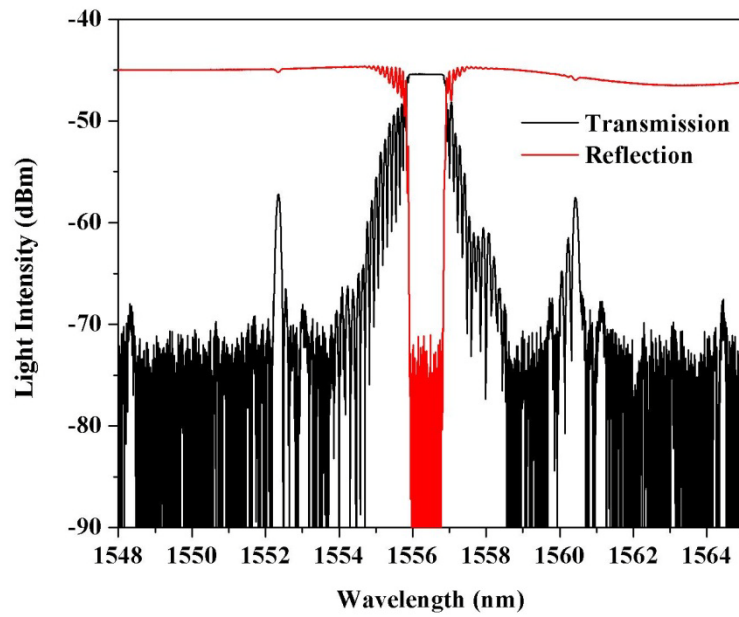
Figure 2.3 The transmission and reflection spectra of a 30-dB strong FBG.

Compared with other types of fiber sensors, such as fiber interferometers, grating sensors have great flexibilities in both time and frequency domain multiplexing. Gratings with different Bragg wavelengths can be inscribed on the same fiber and interrogated at the same time with broadband light source and optical spectrum analyzer. Weak gratings with the same Bragg wavelengths can also be inscribed on the same fiber and interrogated with timely gated pulses. In the following chapters, different FBG sensors are fabricated with this setup and further functionalized for different sensing applications.

2.2   FIBER INTERFEROMTER SESNORS

Another major league of widely adopted fiber sensors belongs to fiber interferometer sensors. Interferences occur between different longitudinal modes in a fiber microcavity, or between different transverse modes collected by the fiber core. The interferences are extremely sensitive to external perturbations such as temperature, strain, pressure and ambient refractive index (RI) changes, which can be easily and accurately interrogated with optical spectrum analyzer in a broadband cases, or photodiodes in narrow band cases.

The most widely adopted fiber interferometer design is the Fabry-Perot interferometer (FPI). Figure 2.4 shows a FPI formed by fusion splice two pieces of single mode fiber with a hollow core fiber. Interferences are generated at the interfaces of different fibers. With enhance fiber end coatings such as a gold mirror coating, the Fabry-Perot cavity can have a very high Q factor for ultrahigh sensitivities to cavity length changes.
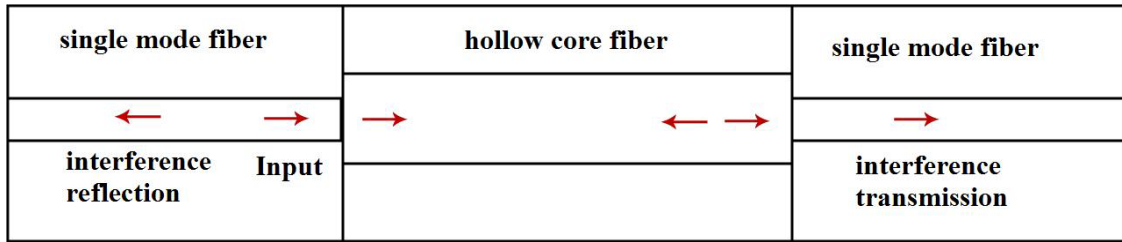
Figure 2.4 Fabry-Perot interferometer
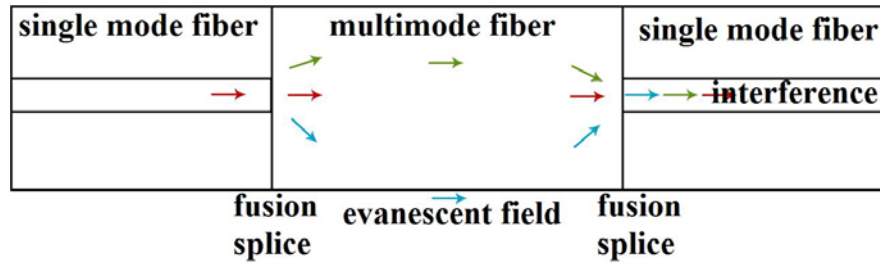
Figure 2.5 Single-mode/Multimode/Single-mode (SMS) modal interferometer.
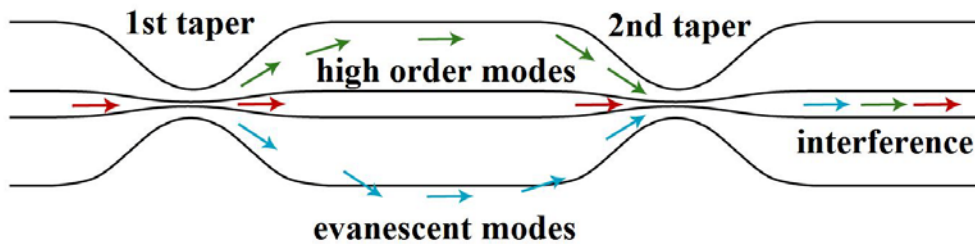
Figure 2.6 A double-taper modal interferometer.

Figure 2.5 shows another type of fiber interferometer, in which a section of multimode fiber is sandwitched by two single-mode fiber, and interferences are generated between different orders of transverse modes with phase differences. When the cladding of the multimode fiber is removed, a significant portion of high order mode power can be propagating outside the multimode fiber. Thus environmental perturbations such as RI changes can be gauged with the shifting of interference pattern.

A similar modal interferometer design is shown in figure 2.6, where two fiber tapers were made with commercial fusion splicer. The 1st taper abrupt the single-mode light propagation and

12

generates high-transverse-order modes in the fiber cladding. The 2nd taper collects the modes and interferences can be seen in the transmission spectrum.

Compared with grating type fiber sensors, such as FBGs and long period gratings (LPGs), fiber interferometers are easy and low cost to make. The lack of photosensitive structure also made fiber interferometers more suitable for high temperature applications.

2.3   IN-FIBER RAYLEIGH SCATTERING FOR DISTRIBUTED SENSING

The telecom grade optical fiber itself, being a perfect silica waveguide, can also be used as a distributed sensing device without any modification. The temperature and strain induced refractive index changes along the optical fiber can be interrogated using different techniques including Raman, Brillouin and Rayleigh scattering. In Raman and Brillouin scattering fiber sensing, optical time domain reflectrometry technique (OTDR) is usually employed, in which the system is probed by fast laser pulses and the spatial resolution is limited by the pulse duration. Faster optical pulses and faster electronics increases the noise level and reduces the dynamic range of the measurement. Typical spatial resolution of OTDR is around 1 meter.

Rayleigh scattering is the elastic scattering of light by subwavelength-size particles during light propagation. In optical fibers, the density fluctuations of silica material give rise to the Rayleigh scattering loss, which is the fundamental loss limit of optical fibers. The Rayleigh scattering coefficient in optical fiber can be defined as [4],

$$\alpha_{Rayleigh} = \frac{8\pi}{3\lambda^4}(n^8 p^2)(kT_f)\beta \tag{2.10}$$

Where n is the refractive index, p is the photoelastic coefficient, k is the Boltzmann constant, β is the isothermal compressibility, and T_f is the fictive temperature at which the density fluctuations are frozen. From the equation, the Rayleigh scattering signature along an optical fiber can be interrogated to measure the local refractive index changes induced by the environmental changes such as temperature, strain and transverse stress. Moreover, contrary to the cases in Raman and Brillouin scattering, the high special resolved optical frequency domain refrectrometry (OFDR) can be applied in Rayleigh scattering measurement in optical fiber [5].
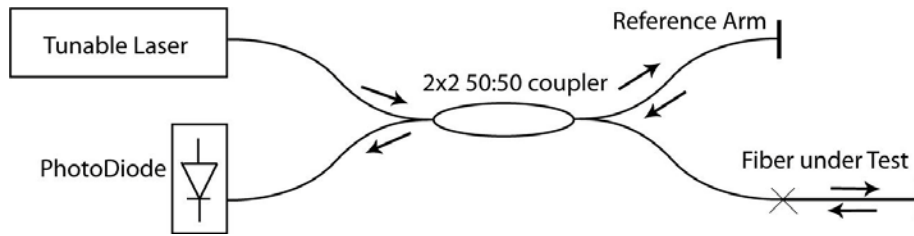
Figure 2.7 Block diagram of OFDR.

The basic idea of OFDR can be explained in the block diagram in figure 2.7. A highly coherent CW laser is linearly swept from $\lambda_0 - \Delta\lambda/2$ to $\lambda_0 - \Delta\lambda/2$ and coupled through a 2x2 50:50 bidirectional fiber coupler into the reference and test arm. A long piece of fiber under test is connected to the test arm. The reflections from both reference and test arms are coupled back through the same fiber coupler and mixed at the photodetector. Time delay between the test and reference arms is $\tau = 2\,nx/c$ at position x of the fiber under test. During this time delay, the optical frequency changes by $\Omega = \tau(d\omega/dt)$. This beating frequency observed on the photodetector determines the position x of the fiber under test, and its amplitude determines the strength of local backscattering. The spatial resolution of the measurement is directly related to the spectral bandwidth of the frequency scan as,

$$\Delta z = (\lambda_0 - \Delta\lambda/2)(\lambda_0 + \Delta\lambda/2)/2n\Delta\lambda \tag{2.11}$$

For example, 20μm spatial resolution is available with a scanning range from 1535nm to 1575nm. The maximum fiber length, on the other hand, is related to the scanning rate of the tunable laser and the sampling rate as,

$$L_{max} = cR_s/4n(\partial\omega/\partial t) \qquad (2.12)$$

With a sampling rate of 2MS/s and a tuning rate of 20nm/s, a maximum fiber length of 40 meters can be measured.
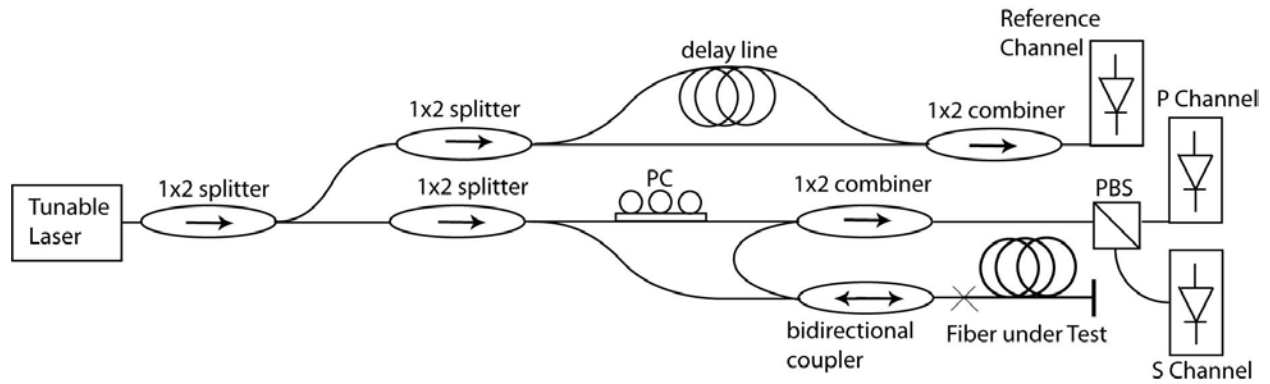
Figure 2.8 Block diagram of polarization resolved OFDR for Rayleigh scattering fiber sensing.

PC: polarization controller, PBS: polarized beamsplitter.

To measure the local Rayleigh scattering, which is due to random fluctuation in the refractive index profile in the fiber core, a more comprehensive interrogation setup is needed, as shown in figure 2.8. The scanning light from a tunable laser is split into two channels. In the reference channel, a fiber interferometer is used to monitor the phase error of the laser tuning. The absolute optical frequency can also be calibrated with a HCN gas cell. In the measurement channel, the scanning light is split and recombined with two 50/50 fiber couplers, and the weak backscattering from the fiber under test is mixed with the polarization controlled reference light at the polarized beamsplitter, where the interference signal from orthogonal polarizations can be measured with respect of the time delay as,

$$E_{s,p}(t) = 2r_\tau g_{s,p}(\tau)(\vec{E}_{meas} \cdot \vec{E}_{ref})\cos\left((\omega_0 + \gamma t)\tau + \varphi\right) \qquad (2.13)$$

15

Where t is the laboratory time for the frequency scan, and τ is the time-of-flight delay with respect to the reference arm, r_{τ} is the reflectivity from the Rayleigh scattering location and $g_{s,p}(\tau)$ is the Rayleigh gain coefficient. $E_{s,p}(\tau)$ can be calculated via fourier transform of (2.13) with respect to t. The total reflection can be calculated as the vector sum,

$$r(\tau) = \sqrt{\left|E_s(\tau)\right|^2 + \left|E_p(\tau)\right|^2}$$

(2.14)

Noted that $= 2\,nx/c$, (2.14) gives the spatially resolved Rayleigh response along the fiber. Compared with the direct approach in figure 2.7, this two-channel polarization resolved acquisition avoids any polarization uncertainty induced by the fiber under test [5].

By cross-correlating with a pre-measured reference, Rayleigh spectral shifts induced by external perturbations such as temperature along the FUT can also be spatially interrogated as [6],

$$r_{measure}(\omega) \otimes r_{ref}^*(\omega) = FFT\left[r_{measure}(\tau) \cdot r_{ref}^*(\tau)\right]$$

(2.15)

$$K_T \Delta T = \Delta\lambda/\lambda = -\Delta v/v$$

(2.16)

Where K_T is the effective temperature response coefficient combining the elasto-optic and thermal expansion coefficient. To obtain a higher temperature resolution, a larger cross-correlation window is needed, at the cost of spatial resolution. The space-temperature resolution product can be expressed as [7],

$$\Delta L(\Delta\lambda/\lambda) = \Delta L(K_T \Delta T) = \lambda/4n$$

(2.17)

A 1-cm cross-correlation window is needed for temperature resolution of 0.1°C or strain resolution of 1-µstrain.
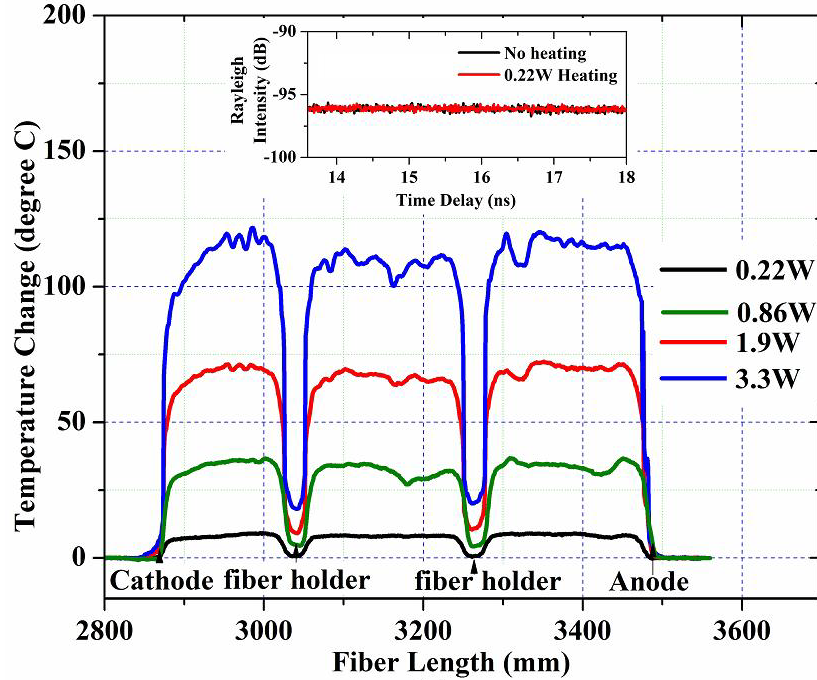
Figure 2.9 Temperature profile of a piece of electrically heated optical fiber

Obtained by in-fiber Rayleigh backscattering measurements; inset: the time domain Rayleigh signal with heated and

unheated fiber measured by OFDR.

Figure 2.9 shows the measurements of temperature profiles on a piece of electrically heated optical fiber using the Rayleigh scattering technique. The Rayleigh signals vs. time delay for the heated and unheated (reference) conditions, as described with formula (2.13) are shown in the inset of Figure 2.9. Temperature profiles are obtained by doing cross-correlation of the two traces and convert the Rayleigh spectral shifts into temperature changes using the effective thermal-optic coefficients of the specific fiber.

When the sensing operation is performed in extreme environment, such as in a high temperature high pressure gas turbine, the number of feedthroughs for the sensor inducement needs to be minimized for both performance and safety reasons. Multicore polarization maintained microstructure fibers, combined with the distributed Rayleigh scattering OFDR

system, provide a solution for spontaneous and distributed measurement of multiple parameters using a single fiber feedthrough.

2.4   IN-FIBER SINGLE BEAM CARS FOR GAS SENSING

Coherent anti-stokes Raman spectroscopy (CARS) is a multi-photon nonlinear process that addresses the vibrational structures of molecules under test. This vibrational frequency is accessed by the frequency difference between pump and stokes laser beam, and the anti-stokes beam is consequently excited by the probe beam in a four wave mixing process (FWM), which has frequency of $\omega_{AS}= \omega_{Pump+} \omega_{Probe}- \omega_{Stokes}$. An energy diagram is shown in figure 2.10, in which different vibrational states can be interrogated with an ultrabroadband laser source, that covers the frequency of pump, and different stock and probe lines.
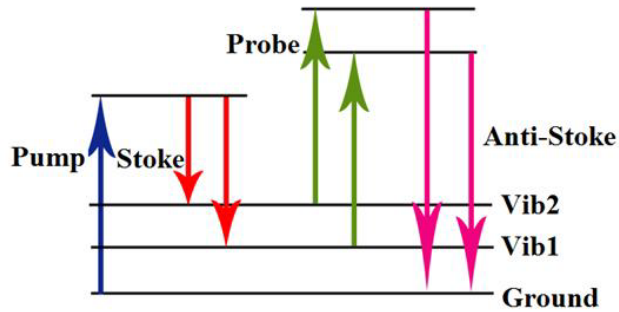
Figure 2.10 Energy diagram of multi-modal CARS.

The ultrabrandband source is readily available with in-house Ti:sapphire ultrafast laser oscillator, which with the help of nonlinear photonic crystal fiber, could deliver highly coherent broadband light spectrum that has bandwidth exceeding one octave, i.e., 500-1000nm. A wide variety of vibrational signatures can be measured simultaneously. But one serious problem is how to identify the unique vibrational signature from the broadband anti-stokes spectrum with

the measurement. One way is to notch out a phase shifted probe signal to print the signature in the broadband spectrum, as is shown in figure 2.10. A similar notch will be observed in the anti-Stokes spectrum at shorter wavelength due to the interference between the broadband pump signal and sharp probe signal [8]. And Raman shifts of the measurants can be identified as the difference between the two notches. With an ultrafast laser output of 700-820nm, multiple Raman traces of $>2000cm^{-1}$ bandwidth can be interrogated with a single pulse shot.
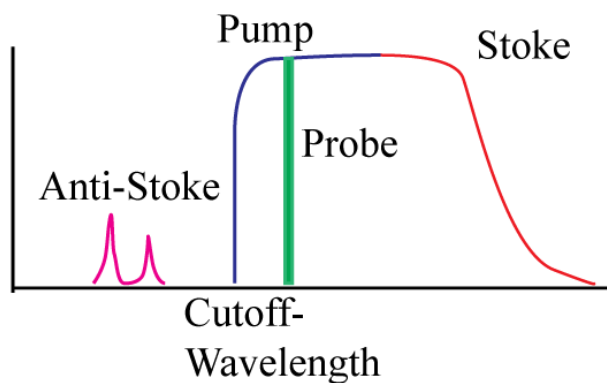
Figure 2.11 Spectra of broadband single-beam CARS with phase notched probe.

3.0   CRYOGENIC HYDROGEN GAS SENSORS

3.1   HYDROGEN FIBER SENSING AND SELF-HEATING TECHNIQUES

Cryogenic fuels such as liquid hydrogen, oxygen, and liquefied natural gas are often considered as major energy alternatives to coal and petroleum based fossil fuels for cleaner power generation [9]. To ensure the safe storage, transfer, and dispensing of liquidified fuels, highly sensitive and highly reliable sensor networks are required to provide continuous monitoring of multiple parameters in multiple locations for on-demand, real-time fuel management in cryogenic environments. For example, due to its explosive nature, leak detection of hydrogen fuel is always of critical importance. However, continuous monitoring of other condition parameters such as flow, pressure, temperature, and liquid level are also necessary.

Compared with other optical and electronic sensing devices, in-fiber optical sensing offers several important advantages, including low manufacturing costs, immunity to electromagnetic fields (IMFs), long lifetime, high sensitivity, and the capability of working in harsh environments. The miniaturized structures and low transmission losses of optical fibers enable the deployment of sensor networks for multi-point and long-distance remote sensing. Fiber Bragg gratings (FBGs) are a key component for in-fiber optical sensing, and Pd-based FBGs provide an all-fiber and explosion-proof solution for measuring hydrogen gas leakage [10-12]. A thin layer of palladium (<1µm) is coated on the bare surface of the FBG, as shown in

figure 3.1. Expansion of the palladium film due to the hydrogen absorption induces longitudinal strain in the underlying FBG. This in turn shifts the FBG reflection peak toward longer wavelengths, and the spectral shift can be interrogated using either a broadband source or a tunable laser. Figure 3.3 shows the operation of a 350-nm thick Pd coated FBG sensor to 0.2-5% hydrogen concentration at 90ºC, measured by our collaborators at Lakeshore Cryotronics. Several different Pd based fiber hydrogen sensor are compared in figure 3.3, in which different optical parameters are measured with respect to the Pd hydrogen absorption.
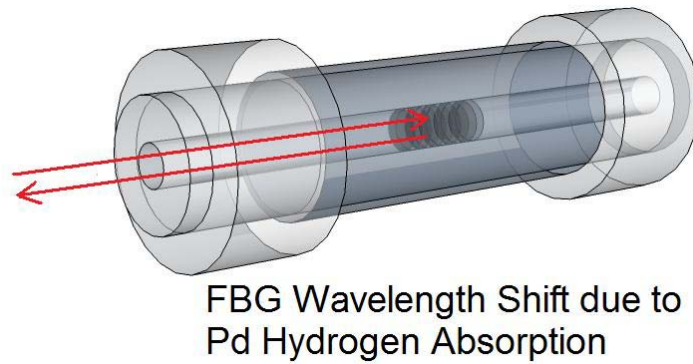
Figure 3.1 Palladium (Pd) coated hydrogen sensor.
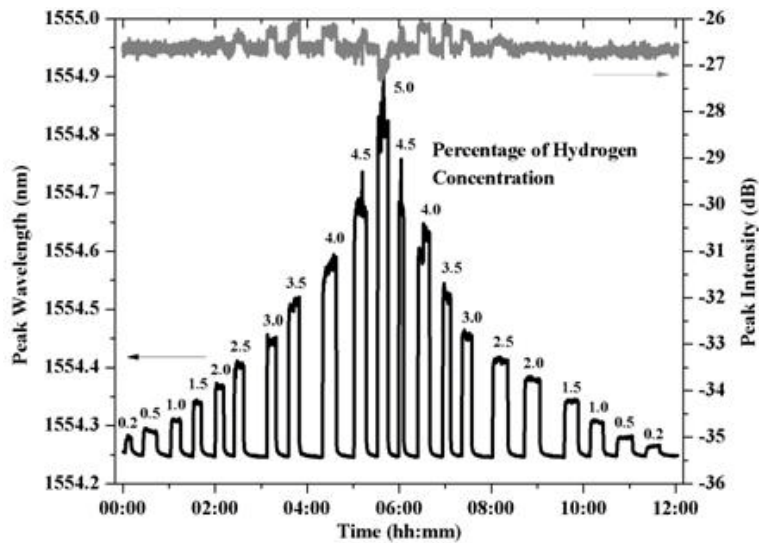
Figure 3.2 Sensor response of Pd coated FBG to 0.2-5.0% hydrogen at 90ºC.

21

	FBG	Evanescent Taper	Micromirror	Surface Plasmon
Measurement Mechanism	Wavelength Shift	Transmission	Reflection	Transmission
Multiplexibility	Yes	No	No	Limited
Robustness	Good	Poor		Poor
Low Temp Performance	Poor	Poor	Poor	Poor
Response Time 300K	90sec (50pm sweep)	16 sec	erratic	74-150 sec
Response Time 240K	900 sec	140 sec	N/A	N/A

Figure 3.3 Comparison chart of Pd-based optical hydrogen detectors.
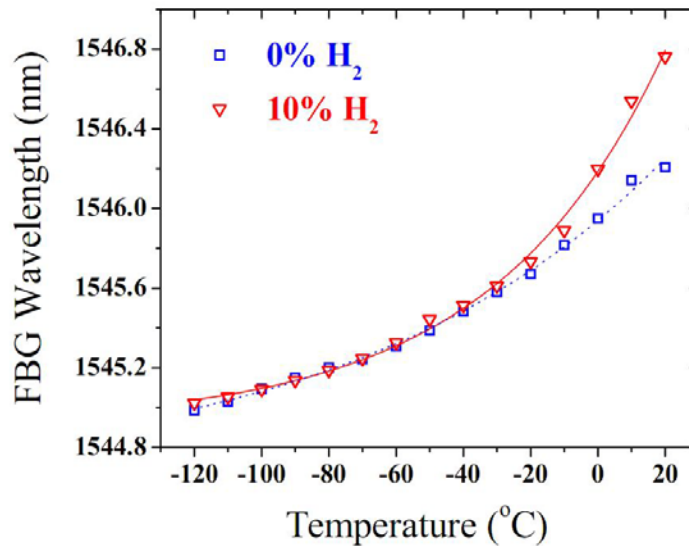
Figure 3.4 Temperature dependent response of Pd FBG sensor [13].

However, the strong temperature-dependence in the hydrogen absorption by Pd presents a serious problem for hydrogen sensing in the cryogenic environment. Because the kinetics of the Pd hydride formation slow down considerably as temperature decrease, both the sensitivity and response times of Pd-based hydrogen sensors rapidly diminish at cryogenic temperatures. Figure 3.4 shows the Pd-coated FBG sensor response vs. different temperature, for 0% and 10%

22

Hydrogen concentration previously measured by our research group [13]. The peak shifts became imperceptible below -20ºC. To overcome this problem, various methods including on-fiber electrical heating have been developed [12-15] to locally increase the sensor temperature in cryogenic ambient. Despite these progresses, a common drawback for on-fiber electrical heating remains. The solution demands electrical cable running with the optical fiber to provide current to the on-fiber heaters. The additional cabling, however, leads to many problems for cryogenic fuel sensing applications, including an increase in manufacturing cost for electrical contact, packaging and multiplexing, and potential hazards of electrostatic sparking in explosive environments.

While electrical heating may improve the performance and functionality of an active fiber optical component, this improvement is achieved at the expense of many intrinsic advantages possessed by the fiber component itself. One solution to this dilemma is to power the fiber optical sensors and sensor networks with in-fiber light and, removing the need for electric cabling. The first fiber sensor with optical heating was reported by X. Bevenot and his colleagues in 2000 [15], in which an optical heated fiber end-mirror sensor was employed for low temperature hydrogen sensing. But the sensor multiplicity was limited by the end-mirror design. Previously, we proposed the concept of in-fiber heating for multiplexible active in-fiber devices [13]. In contrast to a passive sensor or an electrical heated sensor, the optical power is delivered together with a sensing signal through a fiber that also contains in-fiber devices such as FBGs. An optical tap is fabricated in desired sections of the optical fiber to release high-power laser light as an energy source and an optical conversion membrane coated outside of the optical fibers serves as a transducer, converting high-power laser energy to thermal and other forms of energy. The fiber coatings can be further functionalized to actuate the underlying FBG. The

23

concept was realized and implemented into different sensing applications, including a vacuum sensor [16], a two dimensional flow sensor [17], a liquid level sensor [18] and a hydrogen sensor [13].
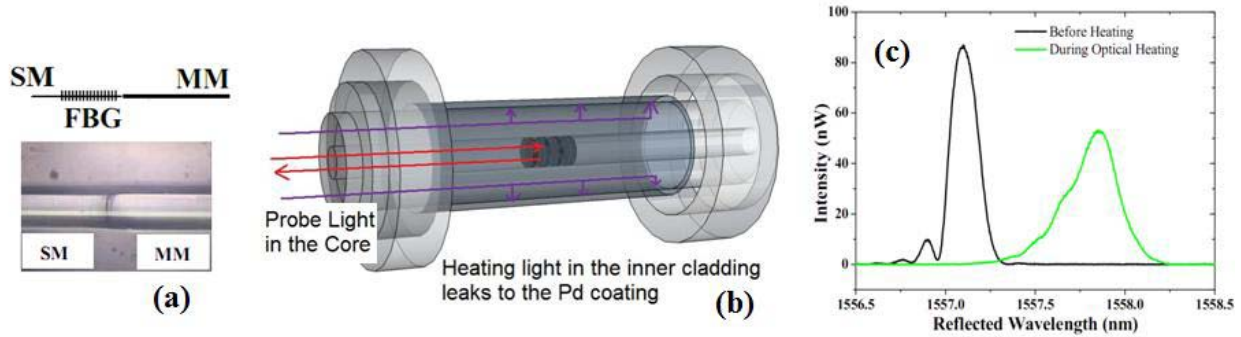
Figure 3.5 Previous in-fiber heating results

(a) Local in-fiber heating with multimode optical power [16]; (b) An improved in-fiber self-heating design with double-clad fiber; (c) the FBG peak chirping due to the ununiform heating profile.

The first realization of our in-fiber heating concept was a multimode fiber design [16, 17]. The heating power was delivered from the core of the multimode fiber to the cladding of single mode fiber through fusion splicing, as shown in figure 3.5a. By producing an intentional exponential loss of light through the cladding, the metal coating outside the FBG was heat up. 90% of the light was lost within 100-mm of the single mode fiber section from the splicing joint. The high optical loss over a short distance of fiber prevents any practical multiplexing of fiber sensors. Moreover, severe chirping of FBG response compromises the sensing resolution.

In a latter design [13, 18], a double-clad optical fiber was used to deliver optical power, as shown in figure 3.5b. While the sensing light interacted with the FBG in the fiber core, the heating light propagated in the inner cladding of the fiber. In the FBG section, the plastic outer cladding was stripped and a layer of metal film was directly coated outside the inner cladding. This allowed the optical heating of the metal coating through the absorption of the leaked optical energy. The rest of the power light continued to propagate in the inner cladding, and is used to

heat further fiber sensors down the fiber feed-through. However, the direct contact and power transfer between thermal tap (the inner cladding) and the actuator (metal coating) presented certain disadvantages here. For example, any defects of the metal coating results in local hot spots and distortion of the signal. Figure 3.5c shows the FBG peak chirping during the heating of a double-clad sensor. Also, the inability to control the excess loss of optical power at single thermal tap reduced the multiplexing of self-powered FBG sensors.

In this chapter, we present a new in-fiber heating sensor design using high attenuation fibers (HAFs). This configuration prevents direct contact between thermal tap and metal coatings, eliminates the effect of local coating defects, and drastically improves the uniformity of optical heating and sensor multiplexing. In addition, an all-fiber sensing system with in-fiber light source, sensors and interrogators is developed for cryogenic fuel sensing applications. Using HAF, Pd-FBG sensors are shown to be heated by in-fiber light to more than 300K above the ambient temperature without significant chirping or generation of local hot spots. This enables rapid and sensitive hydrogen sensing using traditional Pd-FBG sensors at the liquefaction temperature of hydrogen. In addition, multiplexing operation of cryogenic liquid level sensing are also demonstrated with four aluminum coated FBG sensors using HAF.

In section two of this chapter, the principles and designs of the in-fiber heating sensor and heating light source are described in detail. In section 3 and 4, experimental results of a low-temperature hydrogen sensor and a cryogenic liquid level sensor array are presented.

3.2   OPTICAL HEATING USING HIGH ATTENUATION FIBER

High attenuation fiber was recently developed and commercialized for precise loss control of optical signals. The core of the HAF is heavily doped with Cobalt and Germanium to provide measurable photon scattering and energy loss during the single mode light propagation. It has been reported that active thermal tuning of FBG was realized with FBG inscribed into HAF [19]. There are two advantages of using HAF as thermal tap in the in-fiber heating design. First, the power loss in the HAF core can be precisely controlled by the selection of different doping and fiber length. Second, the metal coating has no direct contact with the thermal release core of the fiber. The heat transfer in the fiber cladding ensures more uniform heating profile and eliminates local hot spots due to coating defects.
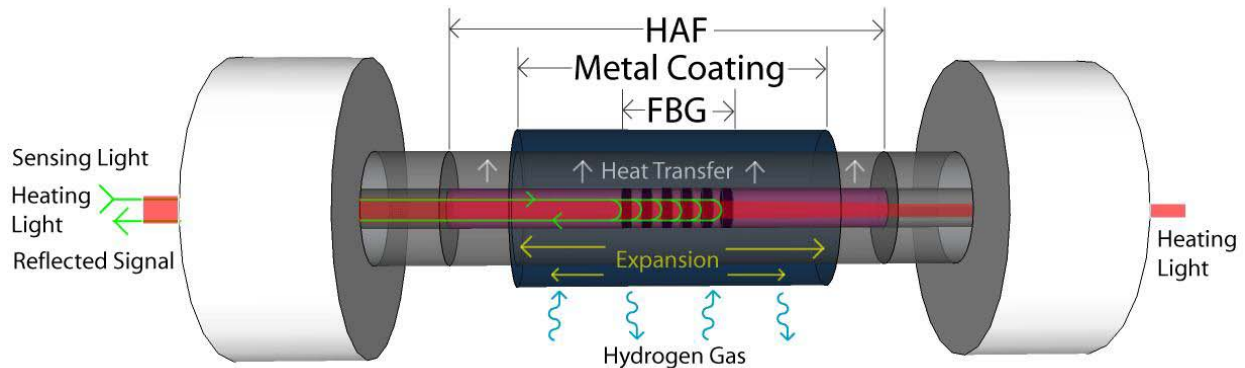
Figure 3.6 Schematic sketch of an in-fiber heating sensor with HAF.

Figure 3.6 depicts the design of in-fiber heating sensor using HAFs. A short section of 1-cm long HAF (0.2-dB/cm, 0.5-dB/cm and 1dB-/cm attenuation at 1300-1600-nm, CorActive, Inc.) was fusion spliced between two standard pigtail fibers (Corning SMF-28e). The splicing loss was less than 0.02dB. The fiber assembly was then hydrogen loaded at room temperature in 2200 psi pressure hydrogen for a week to increase the photosensitivity. FBGs were inscribed into the HAF core using a 248nm KrF Excimer laser and a phase mask with λ_B = 1545 nm.

Subsequent annealing for 12 hours at 120C stabilized the Bragg grating. A sputtering coating process then was used to deposit layers of metal coating onto the surface of FBGs. For palladium coating with thickness of 150-450nm, a 20-nm thick layer of glue metal was deposit first on silica fiber to improve adhesion. The thickness of the aluminum coating for the level sensors was estimated to be 150-nm. After the sputtering coating, the two fusion splicing joint was recoated with UV curable epoxies to reinforce the sensor structure.
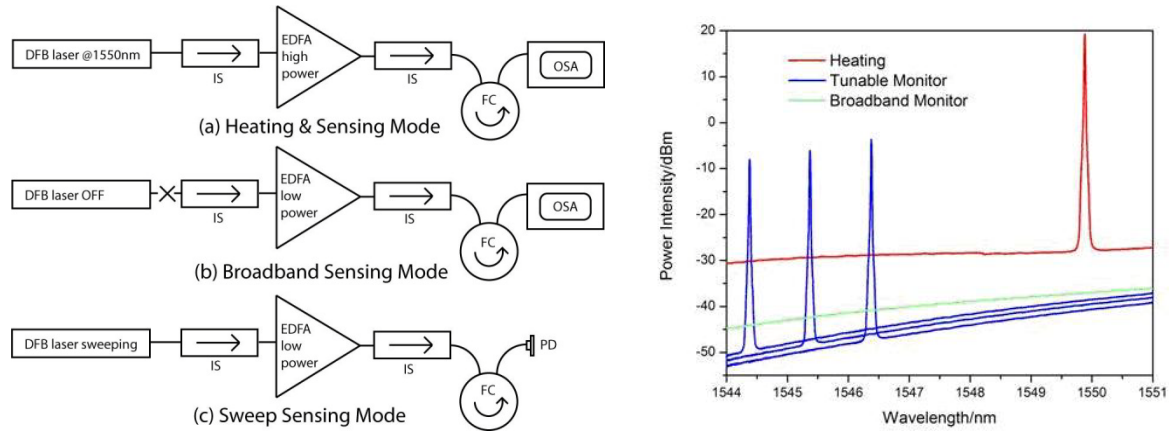
Figure 3.7 Schematic of the multi-functional light source

(a) high power heating and sensing mode; (b) low power sensing mode (c) sweep sensing mode (DFB laser: distributed feedback laser; IS: in-line isolator; EDFA: Erbium-doped fiber amplifier; FC: fiber circulator; OSA: optical spectrum analyzer; PD: photodiode). Right: the output spectrum of different operation modes.

A multifunctional light source was built for evaluating the self-heated fiber sensor, as shown in Figure 3.7. A single-mode tunable Distributed Feedback (DFB) laser source (HP 8168) was coupled into a custom made, multistage Erbium-doped Fiber Amplifier (EDFA). The gain fibers in each amplification stage were carefully chosen to balance the amplifications between DFB peak and the amplified spontaneous emission (ASE) background. As shown in Figure 3.7, there are three different modes of operation. First, the heating mode provides up to 1100mW of in-fiber heating power, peaked at 1550-nm. A weak and smooth ASE background 50dB below the heating peak was also present in this mode, and an Optical Spectrum Analyzer (OSA, Ando

6317B) can be used to monitor FBG reflection spectra during the heating. To monitor FBG response without optical heating, in the second mode the DFB seeding laser is turned off and the amplifier pump power is turned down to produce a weak ASE background with less than 1-mW optical power At this power level, the in-fiber heating is negligible. Finally, to resolve spectral structure with resolution higher than the OSA resolution, there is also a third "sweeping" mode for higher spectral resolution. With the peak frequency of the DFB seeding laser continuously sweeping in 1-pm resolution, the amplification pump power is turned down to the unity gain for minimal in-fiber heating, and the spectral response from the sensor can be measured using a photodiode.
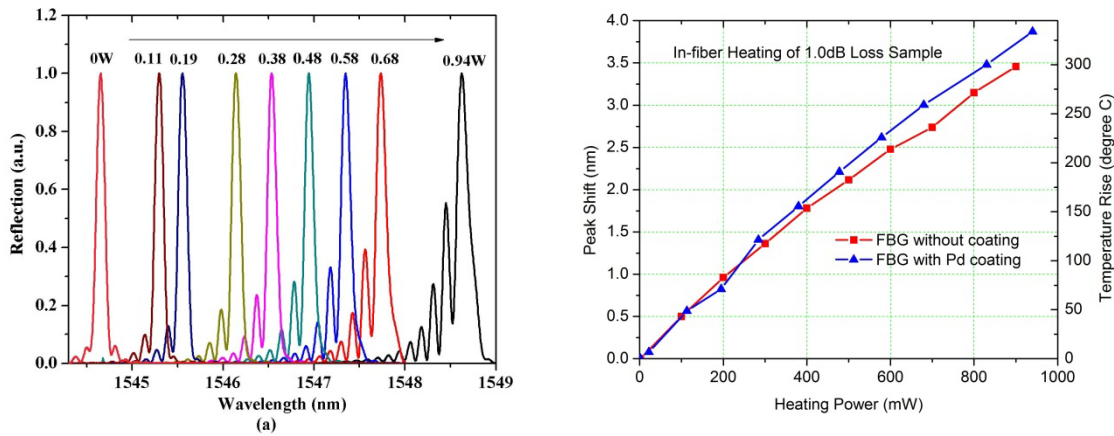
Figure 3.8 1.0dB HAFBG heating results

Left: the reflective spectra of a Pd coated 1.0dB FBG sensor with different heating power; Right: the peak shift vs. input power for Pd coated 1.0dB FBG at room temperature.

By measuring the Bragg grating reflection spectra with an OSA and a fiber re-circulator, the heating of high attenuated FBG sensors is evaluated at both room and cryogenic temperatures. The left part in figure 3.8 shows the normalized reflection spectra of a Pd coated 1.0dB/cm FBG sensor heated with different input power at room temperature. With 940-mW input power, the peak of Bragg grating shifts 3.78-nm to longer wavelength. Compared with

28

previous report [18], it is noted that FBG reflection spectra were only slightly chirped and minimally distorted, which confirms a uniform heating profile of this sensor design using HAF. The right part in figure 3.8 shows the correlation between applied laser power and sensor response for Pd-coated and un-coated 1.0dB HAF-FBG sensor at room temperature of 20ºC. A combined thermal-optical coefficient of 11.3-pm/K at room temperature is used to estimate the heating temperature from peak shift. At 940-mW input power, the 1.0dB sensor is heated up by approximately 300K above the ambient temperature. The Bragg grating peak shifts of the metal-coated sensor is slightly larger than that of uncoated sensor due to the additional thermal expansion of metal coating.

In this section, we demonstrated that the new design of in-fiber heating system for optical sensing using HAF. A custom-built fiber amplification source provides both the heating light and sensing light to the sensor. Measurements of heating characteristics show that the in-fiber heating in HAF sensor is uniform and efficient. Moreover, the local heating source using HAF fibers can be precisely controlled and multiplexed in one fiber.

3.3   LOW TEMPERATURE HYDROGEN GRATING SENSOR
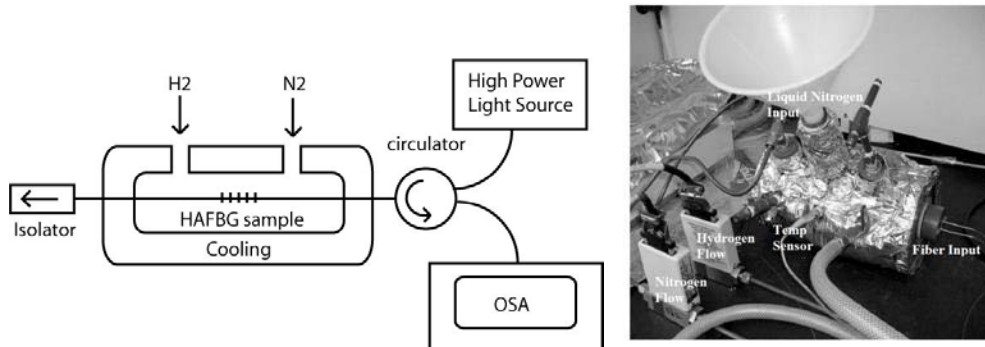
Figure 3.9 Experimental setup for low temperature hydrogen sensing measurement.

In this section, we describe a fiber optical hydrogen sensor for the cryogenic environment operation. The local heating source using HAF enables rapid sensor response with improved sensitivity.

The 450-nm thick Pd coated 1.0-dB loss HAF-FBG sensors were tested in a temperature regulated chamber described in figure 3.9. Testing of the sensor was performed in a sealed temperature-regulated chamber capable of maintaining -120 – 120$^{\mathrm{o}}$C through the use of encapsulating liquid nitrogen cooling or recirculating fluid heating. Fiber feed-throughs were placed at either end of the chamber for sensor access. Two mass flow controllers provided a variable hydrogen and nitrogen mix for 0-10% H_2. Chamber pressure, temperature, and gas flow were monitored continuously. The test is performed at atmospheric pressure. Minimum tension (<20g) is applied to the test fiber. The reflection spectra of FBG are measured with an OSA behind a fiber recirculator.
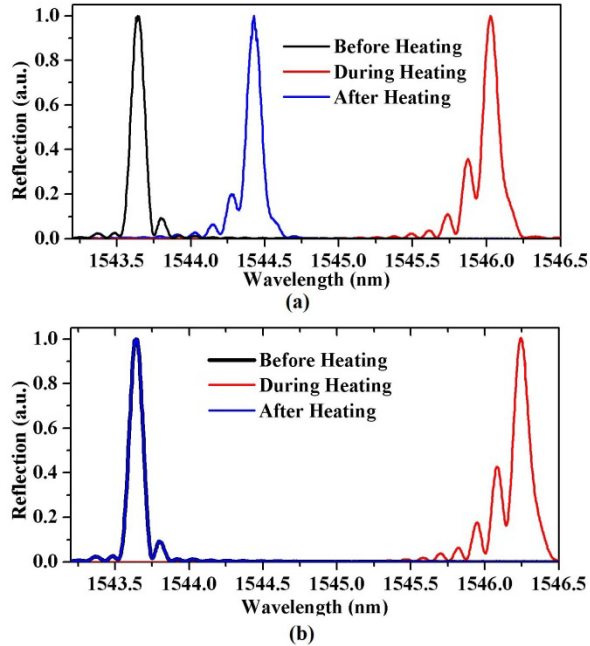
Figure 3.10 Heated sensor responses at -100°C with and without 10% hydrogen.

The hydrogen sensors' performances were characterized at -50°C. Previous work [18] has shown that a passive Pd-based FBG sensor starts to lose its performance at -25°C (248K), which were re-confirmed in this work. The un-heated Pd-FBG sensors were exposed in 10% hydrogen for 30 minutes without any observable peak shift at -100°C. The optical heating effects on the Pd coated hydrogen sensors are shown in Figure 3.10. The Bragg grating peak shifts more than 2nm (red) from its ambient position (black) with 0.7 W of the input laser power. After a brief 60 second period of optical heating in 10% hydrogen, the power light was turned off. The Pd-FBG sensor was immediately cooled back to the -100°C ambient but the sensor retained residual strain due to the accelerated Pd hydride formation during heating. 782 pm FBG peak shift is shown in Fig 3.10(a) (blue). The control experiment was also performed as shown in figure 3.10(b). The same optical heating and cooling cycles were applied to the sensor without the present of hydrogen (100% nitrogen). No appreciable peak shift was observed. We also noted that heating efficiency is higher in 100% nitrogen than in 90% nitrogen/10% hydrogen combination, because

31

hydrogen molecules have relatively higher thermal mass than that of nitrogen. The whole hydrogen absorption process was completely reversible and repeatable. A control cycle of 60 seconds and 0.7W optical heating in 100% nitrogen completely removes the 782pm peak shift and strain residue due to hydrogen absorption. This allows intermittent sensor heating and hydrogen leakage detection in a real-time monitoring system.
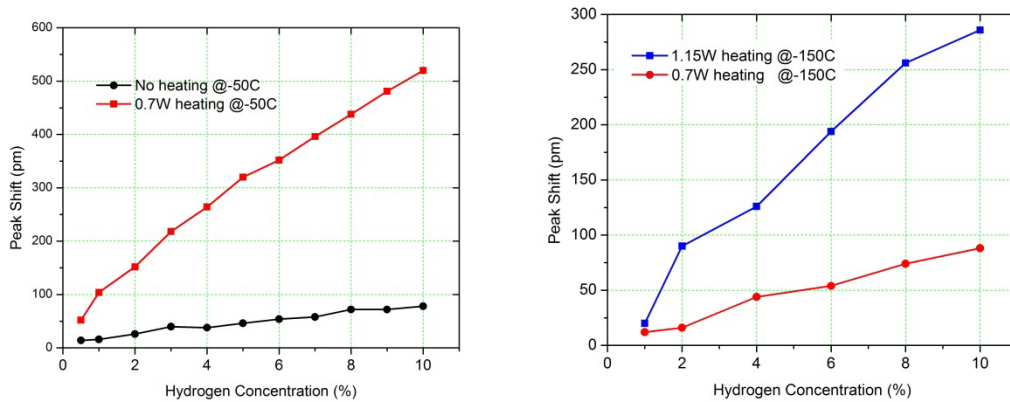
Figure 3.11 Sensor response to hydrogen concentration and input power.

The observed spectral shifts with variable ambient hydrogen concentrations and temperatures were delineated. Figure 3.11(a) details the results at -50°C. The sensor calibration was performed for hydrogen concentrations from 0.5% to 10% with 30 seconds exposure time. The 0.7W input power heats the sensor 200°C above the ambient temperature (with 2.5-nm peak shift according to figure 3.10(a)) and increase the sensor response by 7 times compared with unheated sensor. At the minimum hydrogen concentration of 0.5% (apparatus limited), the sensor response is 51-pm. Figure 3.11(a) shows that hydrogen concentration well below the explosive threshold of 4% can be readily detected at -50°C. And Figure 3.11(b) shows the results at -150°C. Both 0.7 and 1.15W of laser heating power are applied for 30s hydrogen exposure and the subsequent absorption shift is compared. The 0.7W laser power is able to raise the local temperature of Pd-

coated FBG sensor ~200K above the ambient, while the 1.15W of laser heating power can heat the sensor ~300K. For hydrogen concentration of 10%, the sensitivity is enhanced by ~2.8 times with 1.15W comparing with 0.7W. But only marginal improvement was observed at 1% hydrogen concentration, at which a 27-pm Bragg wavelength shift was observed.

Even stronger local heating is possible with higher input power and higher HAF doping. For the 1.0dB loss sensor used in this experiment, approximately 20% of laser light was absorbed by a single sensor. If the FBG and the HAF were shortened, substantial less power light is needed to raise the sensor temperature to the same level. It is therefore feasible to multiplex multiple (5-10) hydrogen sensors in a single fiber.

3.4   DISTRIBUTED HYDROGEN SENSING

A more challenging issue is to develop distributed sensing technology so sophisticated hydrogen system can be completely monitored using a single interrogation unit. Multipoint quasi-distributed hydrogen sensing has been reported with FPI sensors multiplexed in parallel with fan-out fiber coupler [20] and FBG sensors multiplexed in serial on a single fiber [21-23], both of which provide excellent centimeter spatial resolution with their compact sizes. However, the distributed sensing capabilities of FPI and FBG point sensors are fundamentally limited by their multiplexing density and the consequent high manufacturing cost. A more efficient approach is to use the optical fiber itself as a continuous hydrogen sensing device. Sumida *et. Al.* [24] reported 1-meter spatial sensing resolution in a Pd-coated fiber evanescent field sensor design using optical time domain reflectometry (OTDR). More recently, Yang, *et. al.* [25] enhanced the sensing resolution to 10-cm using acoustically generated traveling LPG in Pd-coated fiber.

In this section, we reported 1-centimeter-resolution distributed hydrogen sensing based on Optical Frequency Domain Reflectometry (OFDR) measurements of Rayleigh scattering in Pd/Cu coated optical fibers. This technology has recently been applied to provide distributed sensing solution for temperature and axial strain measurements [26]. Herein Pd/Cu coated single-mode fibers are used to extend its application for distributed hydrogen sensing. By measuring the in-fiber Rayleigh spectral shift, local axial strain induced by Pd-hydrogen absorption is interrogated in 1-centimeter resolution over a piece of fiber under test (FUT). At room temperature, hydrogen sensing operations are performed for hydrogen concentration from 1-10% and sensing time from 1-20 min. It is also shown that the hydrogen sensitivity is significantly enhanced with distributed on-fiber heating, which improves the low temperature sensing performances. By using the optical fiber itself as fully distributed sensing element, the technique demonstrated in this letter completely eliminates the need of using individual FBG and FPI point sensors and cost associated with the manufacturing process. Hereby it provides a practical and inexpensive solution for distributed hydrogen leak detection with a record-breaking distributed spatial resolution comparable to point sensors.
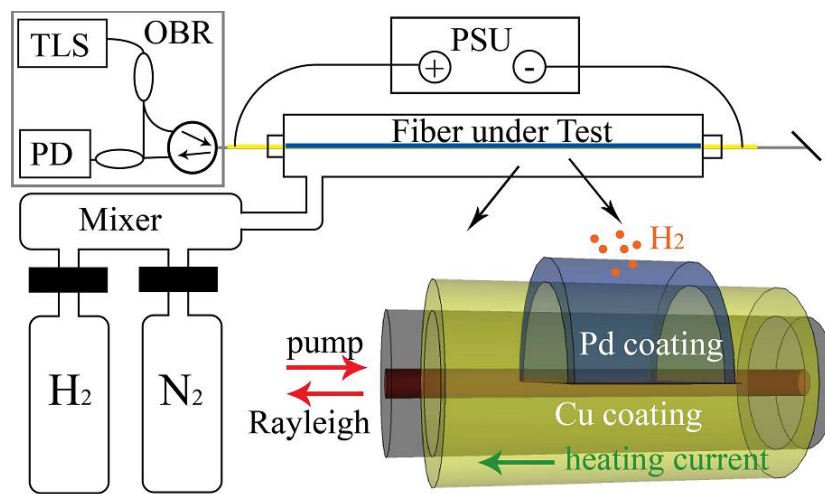
Figure 3.12 Schematic of distributed hydrogen sensing using electrically heated optical fiber.

OBR: Optical backscatter reflectometer; TLS: Tunable Laser Source; PD: Photodiode; PSU: power supply.

34

As shown in Fig. 3.12, proof-of-concept experiments were performed at room temperature (20°C) using a commercial optical backscatter reflectometer (OBR) from Luna Technologies (OBR 4600) [26] connected with a piece of fiber under test (FUT). The single-mode silica FUT was coated with 20-µm thick Cu alloy and further sputter-coated with 1-µm thick Palladium on one side of the fiber surface. 2-m long of Pd/Cu fiber coatings were fabricated in the laboratory with good uniformity. Longer and distributed coatings are also possible. 350-mm long Pd/Cu coated FUT is inserted into the gas test chamber, sealed at both ends with fiber ferrules. Gases from a pure nitrogen gas tank and a 10% concentration hydrogen gas tank are pre-mixed and sent into the test chamber at atmosphere pressure (14.7 psi or 1 bar). The hydrogen concentration under test is controlled with two mass flow meters. The FUT can be electrically heated using a regulated current supply.

The sensing principle of OFDR Rayleigh scattering measurement is introduced in the second chapter of this thesis. In this particular experiment, 1-cm long cross-correlating window is chosen in the experiment to obtain ~1-pm spectral resolution, which corresponds to ~0.67µε strain resolution for the FUT at 1550-nm wavelength. This choice of window size is a careful balance between the required spatial resolution and the Rayleigh sensitivity needed for reliable detection of hydrogen below 4% threshold.
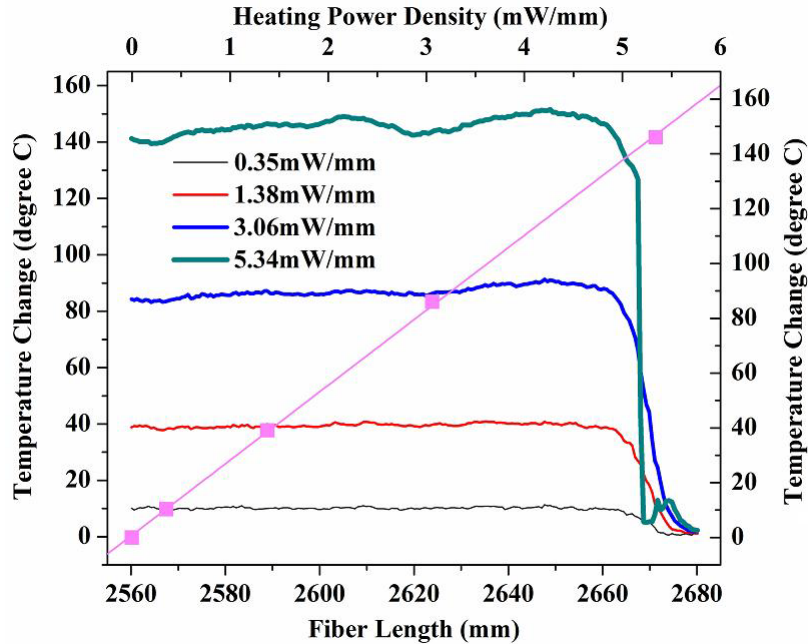
Figure 3.13 Temperature changes of electrically heated fiber measured by Rayleigh scattering.

Firstly the on-fiber heating performance of the sensor is tested in 100% nitrogen. The distributed Rayleigh spectral shifts measured with OFDR are associated with in-fiber temperature changes. Thermal-optic coefficient of 0.06 °C/pm is used for the 20-µm thick copper coated fiber [7], which is approximately half of the value for plastic coated SMF-28 fiber at room temperature. The additional thermal expansion effect from 1-µm thick one-side Pd coating is neglected. Both the heating profile along the fiber and the heating efficiency is illuminated in Fig. 3.13 for different heating current and electrical power densities. Uniform, linear and efficient electrical on-fiber heating is observed along the FUT at smaller current. The fiber can be heated up to 146±5°C using 5.24mW/mm electrical power.
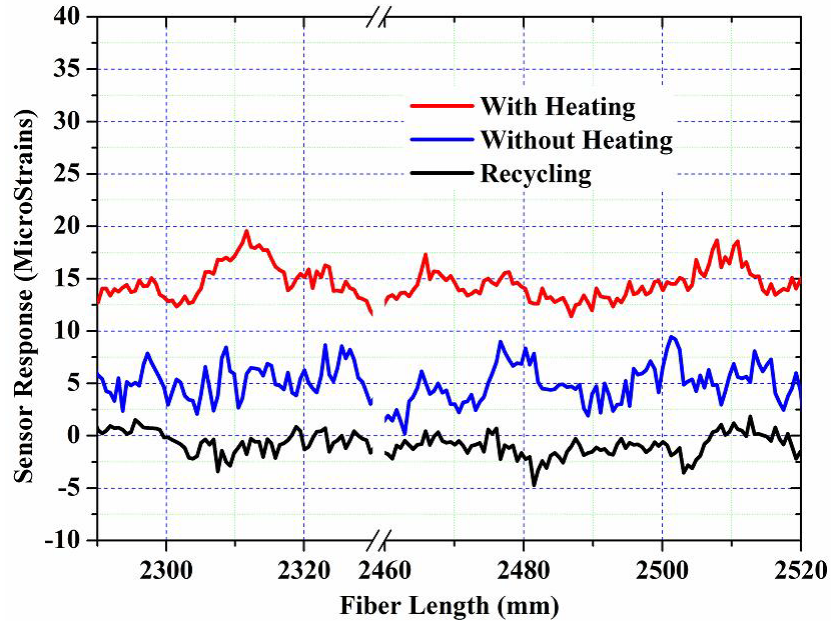
Figure 3.14 Strain response to hydrogen exposure at different position on the same fiber.

To test the distributed hydrogen sensing capability, two portions of the FUT at 2290-2330-mm and at 2460-2520-mm respectively are exposed to 4% explosive-threshold concentration hydrogen for 2-min long with and without the 5.34mW/mm on-fiber heating (e.g. ~140°C on-fiber temperature). The results are shown in Fig. 3.14. Immediately after the hydrogen exposure and shut-down of the on-fiber heating, the distributed Rayleigh spectral shifts are measured. The measurement results are then computed with pre-measured reference to calculate in-fiber strain changes induced by the Pd hydrogen absorption. The heated sensor response is ~3 times larger than unheated response. And 1-centimeter spatial resolutions are obtained for both portions on the FUT. The uneven sensor response could come from the un-uniform coating profile of the Pd coating.
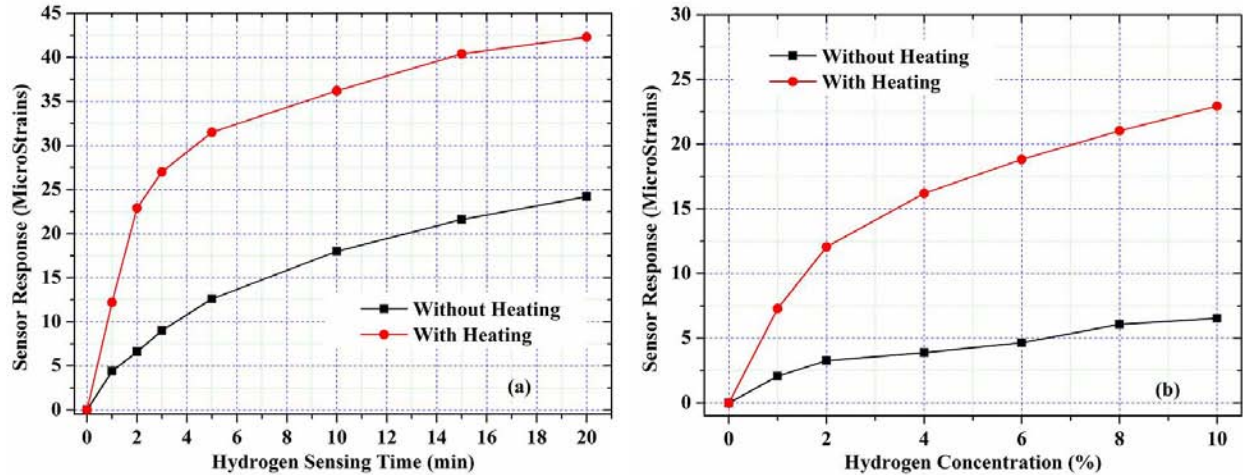
Figure 3.15 Hydrogen sensor responses.

The sensor response with and without electrical heating to (a) hydrogen exposure time from 0-20 min for fixed 10% hydrogen concentration; (b) hydrogen concentrations from 1-10% for fixed 2-min exposure time.

The hydrogen sensor responses are also studied systematically for different hydrogen exposure times and different hydrogen concentrations both with and without the 5.34mW/mm on-fiber electrical heating. The results are detailed in Fig. 3.15. Fig. 3.15a shows that 10% concentration hydrogen can be readily detected within exposure time as short as 1-min. And for a exposure time of 2-min, hydrogen concentration as small as 1% can be readily detected with the chosen Rayleigh sensitivity, as shown in Fig. 3.15b. In both cases, sensor responses are significantly enhanced with on-fiber heating, which eliminates possible detection errors, and more importantly makes this technology promising for low temperature sensing environment.

In summary, we have demonstrated the effective operation of an all-fiber hydrogen sensing system for fully distributed hydrogen leak detection. This technique employs wavelength-swept Rayleigh backscattering interferometry in OFDR fashion to obtain 1-centimeter spatial resolution for hydrogen sensing continuously along a single piece of Pd/Cu coated fiber. The sensor response is enhanced with uniform and efficient electrical on-fiber heating, which makes the sensor feasible for low temperature operation. Further improvements in

38

sensing performances, including response time, sensitivity and detection range are possible through optimization of the Pd/Cu coating recipe. By tuning the heating current and the thickness distribution of Cu coating along the fiber, the electrical heating can be applied flexibly on optical fiber. Spark hazard can be minimized with additional isolation and below threshold heating current. It is also possible to obtain better spatial range and resolution using OFDR components with faster speed and larger range. Temperature cross-sensitivites can be discriminated from the hydrogen strain responses by employing polarization maintained fiber as FUT [27]. Furthermore, using multimode fibers and high attenuation fibers, optical on-fiber heating [22-23] can be employed instead of electrical heating to completely eliminate the spark hazard, but the sensing length is limited to 100-200 mm long and uniform heating profile cannot be guaranteed. In our opinion, this section of the thesis demonstrates a fully distributed all-fiber hydrogen sensing solution with good prospects for practical applications.

4.0   LIQUID LEVEL SENSORS

Liquid level sensors are indispensible devices in fields such as chemical processing, fuel storage and transportations on the ground and in space. They provide location information of liquid/gas interface to ensure safe and efficient liquid utilizations. Historically, both mechanical and electrical liquid level sensors have been widely adopted and proved their reliability in practical usage for the room temperature environment. Compared with traditional electrical level sensors, optical fiber based level sensors offers many advantages including their non-conducting, electromagnetic interference (EMI) immune and corrosion resistant natures, and the ability to perform multipoint, multi-parameter measurements with a single device in harsh environments. In this chapter, we will introduce our liquid level sensing results using fiber interferometers, fiber gratings and in-fiber Rayleigh scattering.

4.1   TAPERED FIBER INTERFEROMETER SENSOR

Fiber-grating-based level sensors have been demonstrated in recent years with different techniques employed to discriminate between gas and liquid phases. For example, fiber Bragg grating (FBG) was mounted on a bending cantilever beam to monitor the liquid level mechanically [28]; Self-heated FBG arrays were able to thermally differentiate cryogenic liquid from gas phase [29]; level sensing using long-period gratings (LPGs) [30] and etched FBGS [31]

have also been demonstrated by monitoring abrupt refractive index (RI) changes cross the liquid and gas interface. But the preparation of fiber gratings involves costly and time-consuming processes including photolithography, photosensitization, UV radiation and post-annealing. Moreover, the level sensing range is limited by the short physical length of the fiber gratings, which are mostly used as point sensors.

Recently, modal interferometer based in-fiber sensors were demonstrated [32-34] for accurate liquid RI measurement. In these devices, interference was induced by coupling guided lights in and out the fiber core mode into fiber cladding modes. The cladding mode phase shifts due to RI changes in the evanescent field result in the spectral shifting of interference patterns. In this section of the thesis, we demonstrate for the first time to our knowledge a tapered fiber Mach-Zehnder Interferometer (FMZI) sensor for liquid level measurement. When the liquid level around FMZI increases, the effective RI of the cladding mode increases due to a higher ratio of liquid to air in the evanescent field. The resulting shift in the interference spectrum can be used for continuous level sensing using one fiber over a much longer distance than that used FBG-based sensors. Temperature influence to the FMZI can also be discriminated from the level response by simultaneously monitoring the spectral shifts in dual optical bands. The proposed FMZI level sensor is low-cost, easy to make and able to measure a longer level range than its grating based counterparts with millimeter sensing resolution.

Two identical tapers were fabricated in a single-mode fiber (Corning SMF-28e) using a fusion splicer (Ericsson FSU-975FA) as shown in Fig. 4.1a. Appropriate splicing parameters were chosen to ensure low loss and high interference contrast. A 190 mm long FMZI were mounted vertically inside a cylindrical container and gradually immersed into distilled water. The water level was monitored by a ruler with millimeter resolution. Light from a broadband

source (BBS, MPB EBS-7210, 1520-1620nm) was injected into the FMZI and the transmission spectrum was recorded by an optical spectrum analyzer (OSA, Ando 6317B). The transmission spectrum minimum which can be obtained by subtracting the broadband source spectrumfrom the FMZI transmission is the peak wavelength of the attenuation spectrum.
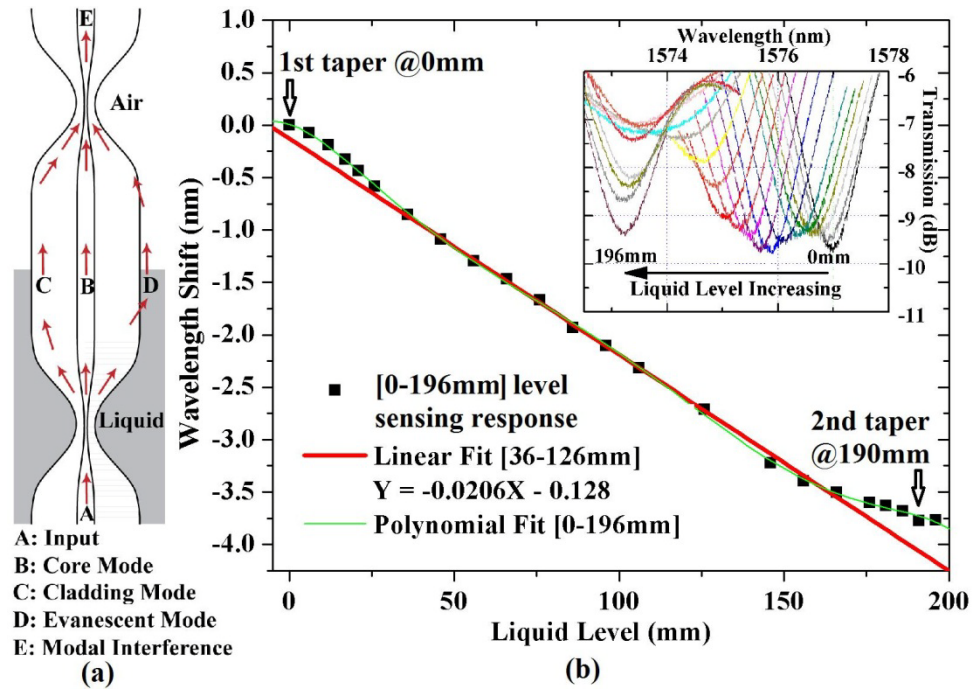
Figure 4.1 fMZI level sensor

(a) The schematic of the fMZI liquid level sensor; (b)Dependence of the spectra wavelength shifts on liquid level for a 190mm long FMZI. Inset: the shifts of transmission spectra when increasing the liquid level.

The shifts of transmission spectrum minima at 1577nm were monitored with respect to the change of submerging water level, and the result is shown as Fig. 4.1b. Blue-shift of 3.77nm was obtained as the level increased from the lower taper position of 0 mm to the higher taper position of 190 mm. The linear response range is 90 mm long from 36 – 126 mm, with level sensitivity of 20.6 pm/mm. Sensing resolution of ~1mm is achieved with spectral resolution of 20 pm for the Ando OSA, which can be further improved by employing a tunable laser as light source, or by applying advanced data processing method such as spectrum differential

integration to a wider spectral range [39]. The FMZI is also able to operate beyond the linear response range by fitting the entire range of 0-196 mm with high order polynomials, as is shown with the green curve in Fig 4.1b.
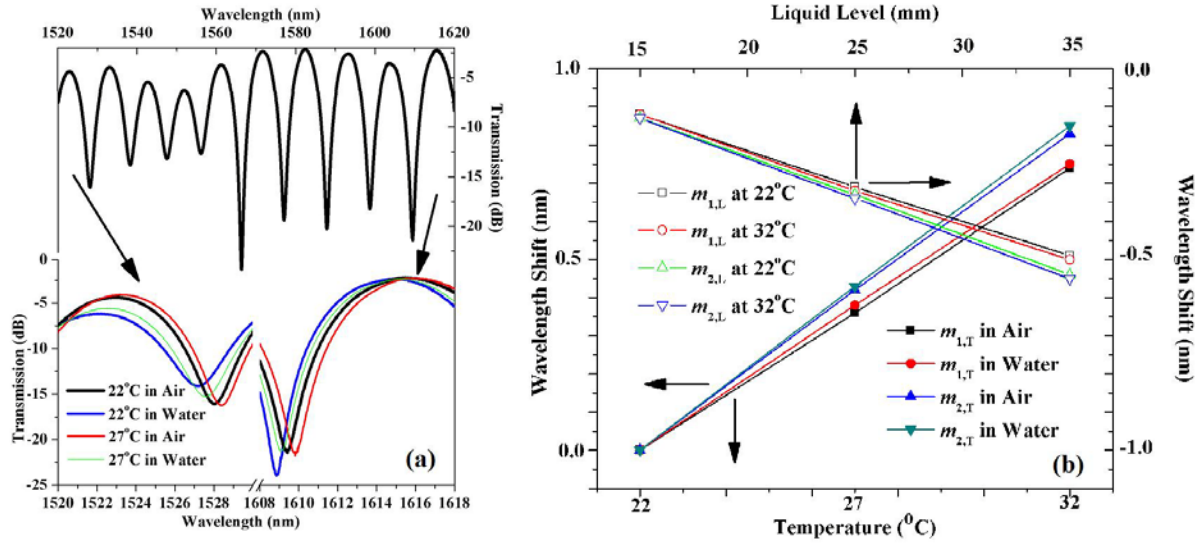
Figure 4.2 fMZI temperature discrimination.

(a)The transmission spectra of a FMZI and the spectral shifts due to temperature and liquid level changes; (b) Dependence of the spectra wavelength shifts on temperature and liquid level for a FMZI for two interference orders (m_1 and m_2).

When the environmental temperature rises, red-shift can be observed in the spectrum due to the increase of RI contrast between core and cladding. Both temperature and level response are dependent on the interference order of the attenuated spectrum, which can be utilized for parameter discrimination [34]. To demonstrate this, a FMZI was mounted vertically in a container with thermal water bath. With careful thermal isolation, the temperature difference between air and water inside the container is <0.1°C. The spectral shifts according to temperature and level changes were monitored at two different interference orders around 1520 nm and 1620 nm. As shown in Fig. 4.2a, the in-fiber sensor responds differently at two

43

interference orders for different temperature at 22 and 27°C and for sensor completely in and out of water. Level responses were recorded when the lower taper at 15, 25 and 35 mm below the water level under 22, 27, and 32°C, respectively. The results were shown in Fig. 4.2b, and can be linearly interpolated into the following sensor response matrix,

$$\begin{pmatrix} \Delta\lambda_{m1} \\ \Delta\lambda_{m2} \end{pmatrix} = \begin{pmatrix} 0.074\,nm/^\circ C & -0.017\,nm/mm \\ 0.084\,nm/^\circ C & -0.021\,nm/mm \end{pmatrix} \begin{pmatrix} \Delta T \\ \Delta x \end{pmatrix}$$

(4.1)

Level sensitivities of -0.017 nm/mm and -0.021 nm/mm, and temperature sensitivities of 0.074 nm/°C and 0.081 nm/°C are achieved for interference orders at 1520 nm and 1620 nm respectively.

In this section, we have demonstrated a tapered fiber Mach-Zehnder interferometer for simultaneous measurement of liquid level and temperature. Compared with fiber grating based level sensors, the FMZI device provides a low-cost, large-range and high accuracy solution to continuous liquid level sensing applications.

4.2   SELF-HEATED GRATING LEVEL SENSOR

Liquid level sensing is an important sensing application for a wide range of industry applications such as fuel transportation and chemical processing. Optical fiber level sensors have been extensively studied in recent years for this application due to their non-conducting, elecromagnetic interference immune and corrosion resistant natures that make them suitable for chemical processing and liquid fuel management. Compared with traditional electrical level sensors, fiber level sensors also have their advantages in multiplexing capabilities and field

ruggedness to withstand extreme environments. A majority of fiber level sensing technologies are based on the refractive index differences between air and the liquid of interest [31-32, 35-36]. However, cryogenic fluids such as liquid hydrogen, liquified nature gas, and liquid oxygen have much smaller refractive indices than water. Thus, the discrimination between cryogenic liquids and gases is more difficult than those in conventional cases [36].

Discrimination of thermal properties between liquid and gas became a prime choice for cryogenic liquid level sensing. Currently, the temperature and level of liquid hydrogen in cryogenic fuel tanks is monitored with a silicon diode sensor array. Excess electric current (tens of mA; measuring current is ~10μA) is delivered to the local silicon sensor and heats it up. The voltage drop across the sensor is monitored to gauge the temperature rise. Due to the larger specific heat capacities and thermal convection rates of liquid hydrogen, the temperature rise in the liquid is much smaller than in the gas. In high-g and microgravity environments in the space program, the spatial distribution of the liquid hydrogen fuel becomes unpredictable and a sensor array with many more sensing points and a more complicated spatial arrangement than those used for ground applications are needed. A larger number of wire feedthroughs are introduced for both power delivery and sensor interrogation, which increases the heat leakage and the potential mechanical and electrical failures.

In this section, we apply the HAF in-fiber heating design to demonstrate an Al-coated four sensor array for cryogenic fuel level sensing. With the choice of fiber doping level and length of HAF for individual sensors, precise control of power loss, sensor temperature and more uniform FBG heating profile can be achieved. The one-fiber active sensor technology demonstrated in this section enables a practical prospect for large numbers of active sensor multiplexing in one fiber.
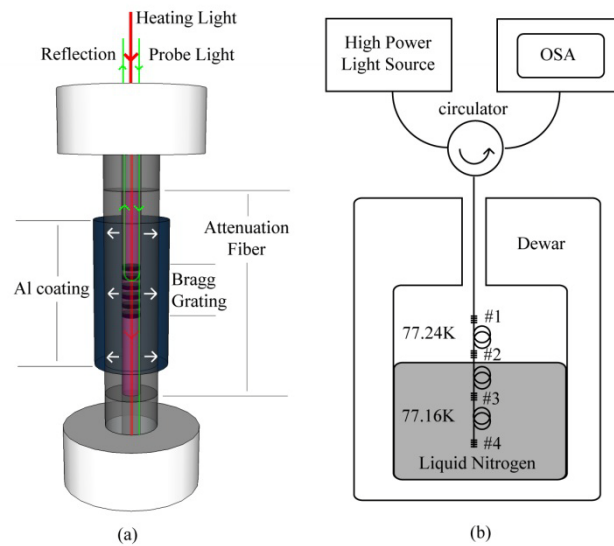
Figure 4.3 Experimental setup for testing the liquid nitrogen level sensor array.

The manufacturing process of the Al-coated FBG liquid level sensor is detailed in the second part of this chapter. FBGs with different peak wavelengths are inscribed into 0.2dB/cm loss and 0.5dB/cm loss HAFs. The sensors were coated with 150-nm thick Al layer using a sputtering coating process. Figure 4.3 shows the sensor design and the experimental setup. HAF-FBG sensors were fusion spliced into a single fiber, passed through a feedthrough and lowered down to the liquid nitrogen level inside a cryogenic dewar. The temperature of liquid nitrogen was measured by a silicon diode temperature sensor (Lake Shore Cryotronics DT-670) to be 77.16±0.02K. And the temperature distribution of saturated nitrogen gas from 0-15cm above the liquid nitrogen level is uniform at 77.24±0.02K, thanks to the long neck, thick wall design of cryogenic dewar. Reflection spectra of the FBG were measured using a fiber circulator and an OSA (Ando 6317B).

One single FBG sensor with 150nm thick Al coating and 0.5dB loss was first evaluated for liquid/gas discrimination and the results are shown in Figure 4.4. Without in-fiber heating, the sensor response can be used as a conventional FBG temperature sensor. The black and blue

curves show that the sensor responses above and below the liquid nitrogen level are indistinguishable due to the nominal temperature difference. When the sensor was submerged below the liquid nitrogen level and heated with 1.07W input power at 1550nm (red trace), the sensor was slightly stretched and the Bragg wavelength shifted only 0.05nm to a longer wavelength due to the large specific heat capacity and thermal convection rates of the liquid. With the same amount of heating power, the 1-cm length sensor was then gradually pulled out of the liquid nitrogen. When the sensor was partially above the liquid level, the Bragg grating peak was severely chirped due to the extreme gradient due to the difference of sensor heating efficiencies between gas and liquid ambient. When the sensor was eventually above the liquid nitrogen level, the Bragg wavelength shifted 1.30nm to a longer wavelength. The Bragg wavelength shift of the sensor was calibrated from 77.16K to 298K and the temperature rise in the fiber core can be estimated using the calibration. The 0.05nm shift below liquid nitrogen level shows only approximately 8K temperature rise, while the 1.30nm shift above the liquid nitrogen level corresponds to approximately 100K temperature rise above the ambient. This excessive heating for a 0.5dB loss sensor leads to slight chirping and distortion of the Bragg reflection peak. However, the heating uniformity using HAF in this work shows significant improvements from the previous in-fiber heating designs [18]. For practical applications, a few Kelvin heating above the ambient will be sufficient to distinguish the liquid level. The chirping and distortion in a less heated FBG with either less optical power, or the use of HAF with less doping, will be minimal.
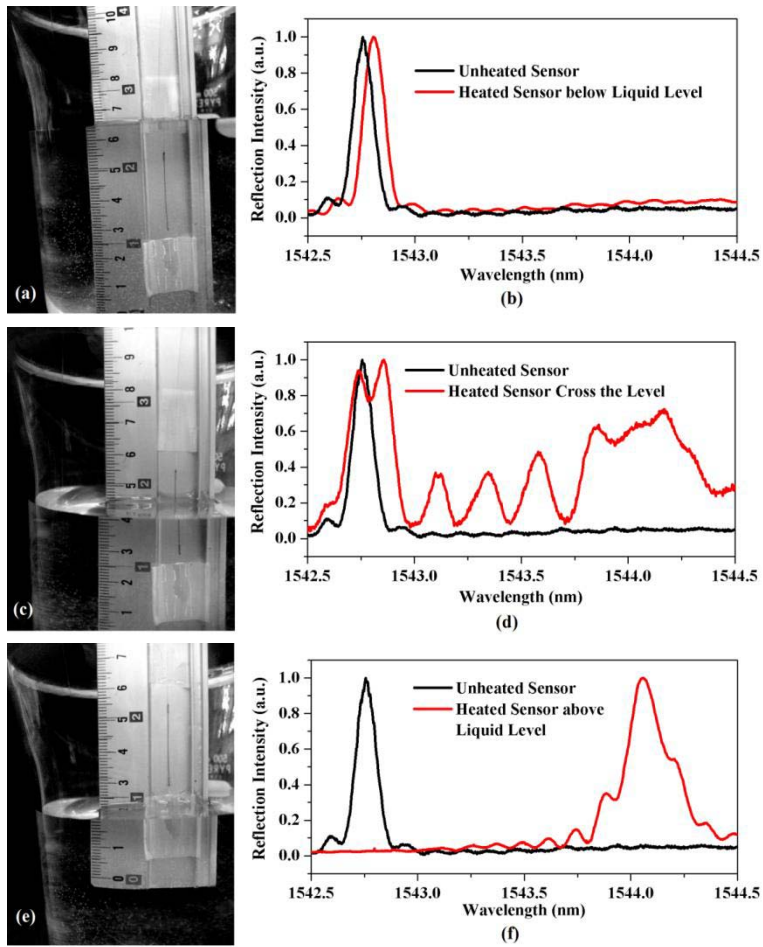
Figure 4.4 Bragg grating response of a 0.5dB loss sensor to different liquid nitrogen levels
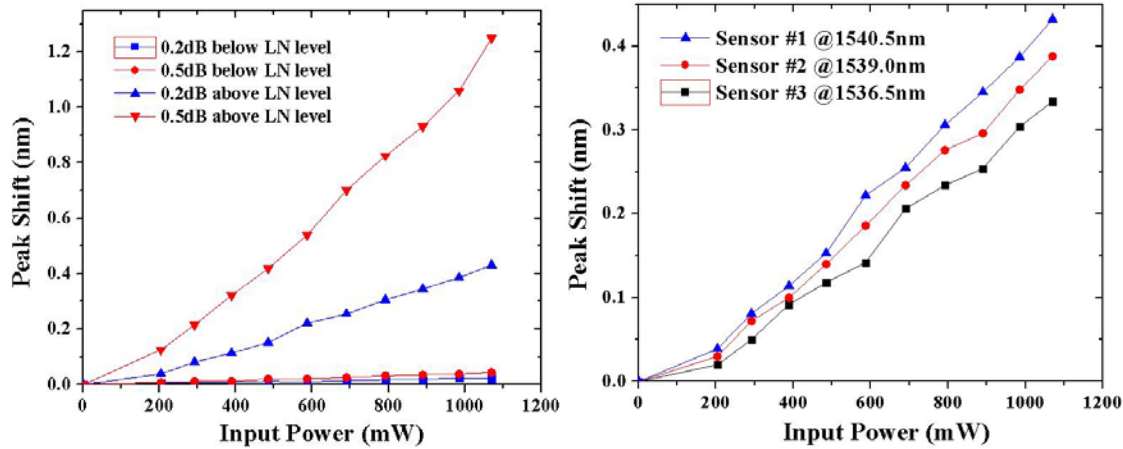
Figure 4.5 The heating efficiency of level sensor.

Left: 0.2dB and 0.5dB sensors above and below the LN level; right: three 0.2dB sensors in a row above the LN level.

The results of heating efficiency measurements for individual sensors are summarized in Figure 4.5. Above the liquid nitrogen level at 77.24±0.2K, the slope efficiency ratio of 2/5 was observed between the FBG in 0.2dB/cm HAF and that in 0.5dB/cm HAF. An exception is also noticed for the final two points on the loss curve using the 0.5 dB/cm HAF, where the sensor is overheated. The sensor responses below the LN level at 77.16±0.2K were also linear but much weaker due to the much larger specific heat of liquid nitrogen compared to that of nitrogen gas. In the interest of multipoint level detection, four FBGs with different Bragg wavelengths in 0.2-dB/cm HAFs were fusion spliced in one fiber separated by 70-cm long lengths of standard fibers. FBG wavelengths, from top to bottom as shown in Figure 4.3, are 1536.5nm, 1539.0nm, 1540.5nm, and 1543nm.

Figure 4.6 Spectral response of a four sensor array pulling out of the LN2

(cont'd next page)
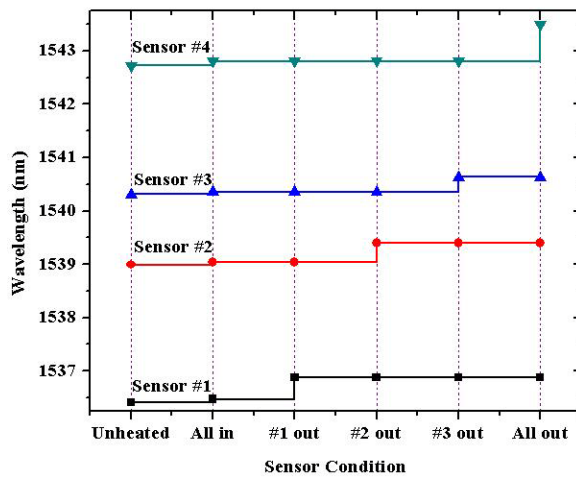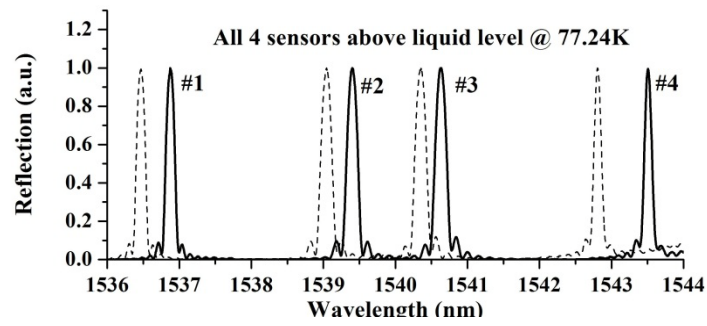
Fig 4.6: Spectral response of a four sensor array pulling out of the LN2 (following previous page)
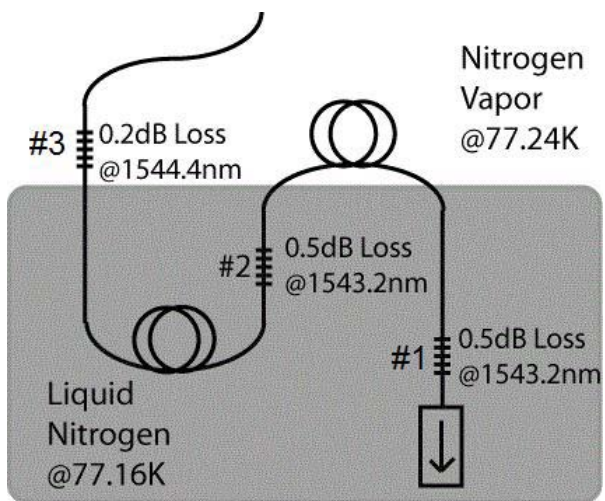
Figure 4.7 Sensor configuration of 3 sensor array with overlapping Bragg wavelengths.

51

Figure 4.6 details experimental results of FBG sensor arrays. With all four sensors above the LN level, every heated sensor shows a significant wavelength shift with respect to their positions at the ambient temperature (dash lines). Minimal peak chirpings and distortions were observed owing to the uniform optical heating. The sensor peak shifts back to its dash line position when the specific sensor was lowered below the LN level. The process is instant and highly reproducible, which demonstrates the feasibility for liquid level detection and sensor multiplexing using HAFs.

In the interest of maximize the sensor multiplexing density, three FBGs with overlapping Bragg wavelengths were fusion spliced in one fiber, and separated 70-m from each other. The FBG wavelengths and optical loss for each sensor from top to bottom as shown in figure 4.3, are 1533.2nm and 0.5dB for sensor #3, 1533.2nm and 0.5dB for sensor #2, and 1544.4nm and 0.2dB for sensor #2. The three FBGs were mounted on a vertical motion stage with 3-cm separation in vertical position from each other, to guarantee temperature uniformity inside the limited space of LN dewar. The heating efficiency measurements of #1-3 sensors indicates that less than 15% of heating power is consumed by a single 0.5dB sensor, and less than 10% of heating power is consumed by a single 0.2dB sensor. And after sensor #3 and sensor #2, more than 70% input power reach the third sensor.
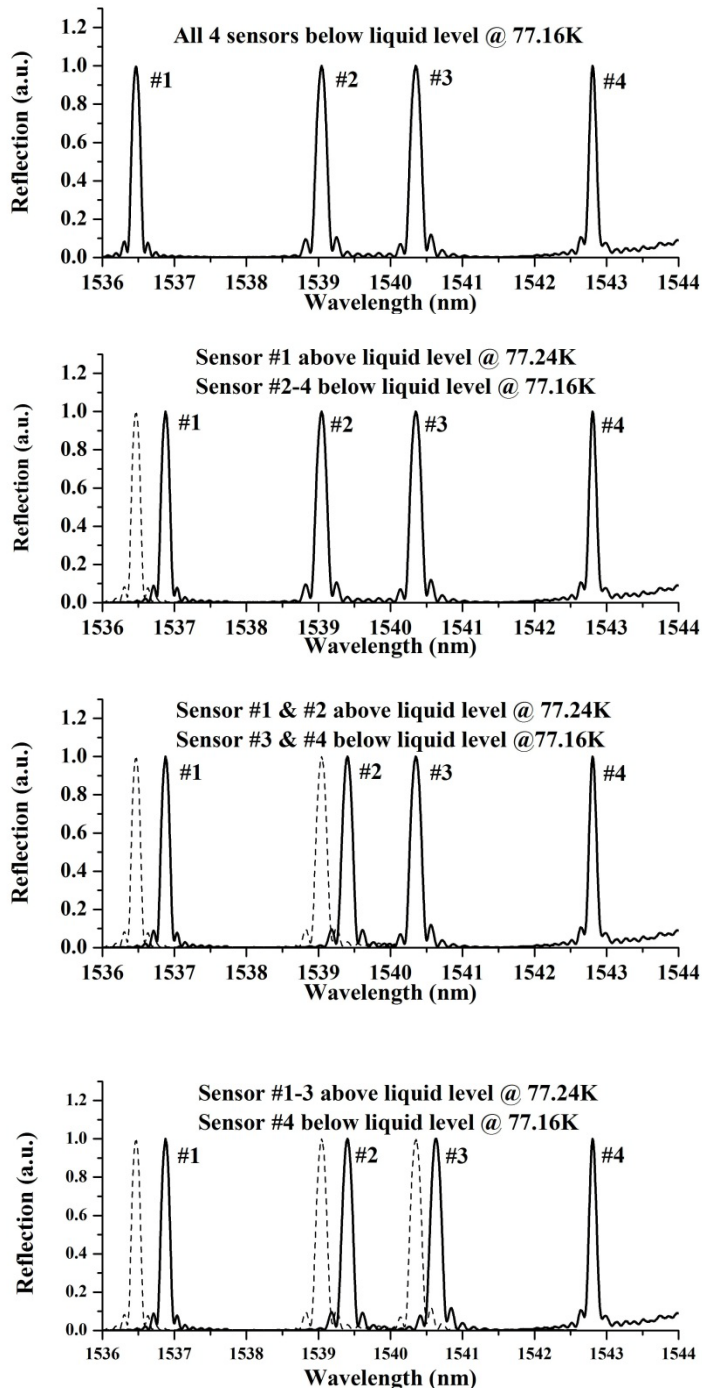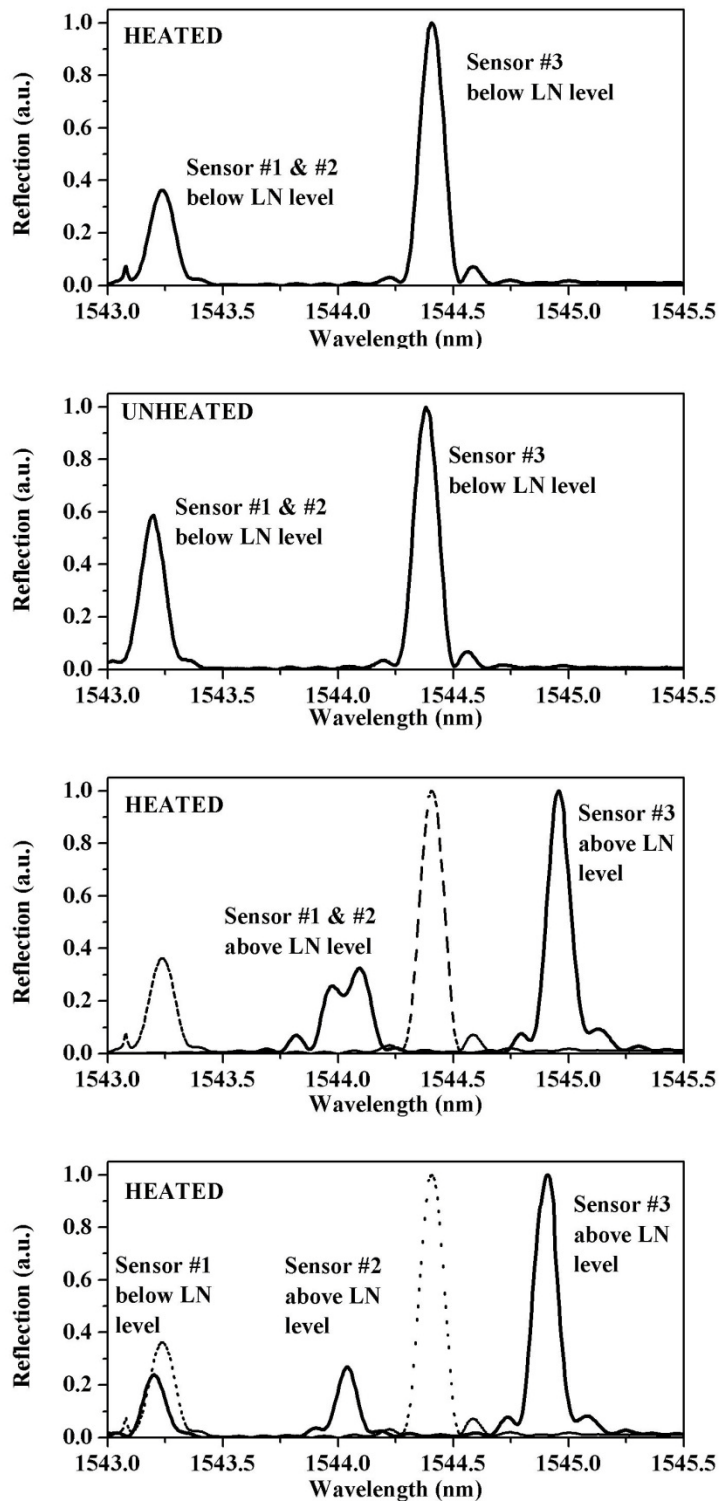
Figure 4.8 Spectral response of a three sensor array pulling out of the LN2

(cont'd next page)
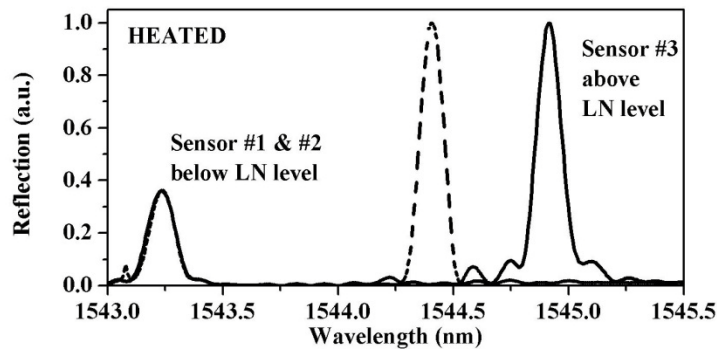
Fig 4.8, Spectral response of a three sensor array pulling out of the LN2. (following last page)

Figure 4.8 details the spectral responses during the pulling. With all three sensors below the LN level, the heated peak position of each sensor is recorded as the reference (in black). The peaks from sensor #1 and #2 overlap with each other. Once a sensor is pulled out of LN and above the liquid level, the heated peak immediately shifts away from its reference position. Finally with all three sensors above the LN level, every heated sensor shows significant amount of wavelength shift due to the optical heating. Compared with previous report [18], minimal peak chirpings and distortions were observed. It is also noted that the overlapped peaks of sensor #1 and #2 split up at above the LN level. This is because sensor #1 is further away from the heating source than sensor #2, and after 10% of the heating power been absorbed by sensor #2, the heating power absorbed in sensor #1 is slightly lower. With the splitting, identical sensors with same Bragg wavelength can be multiplexed for multipoint interrogation. When we reverse the process, the sensor peak shifts back to its baseline position when the specific sensor is below the LN level again. The process is instant and highly reproducible, which demonstrates the feasibility for liquid level detection and sensor multiplexing. This sensor array with overlapping Bragg wavelength for further multiplexing has also been successfully interrogated by a more advanced interrogation method called "Frequency Shifted Interferometry" [37], with the help

from our collaborators in University of Toronto. The results has been published somewhere else [38].

In this section, we demonstrated the effective operation of an in-fiber level sensor array for multipoint cryogenic fluid level sensing. Each sensor employs a FBG inscribed in co-doped HAF to achieve precise and uniform heating of a FBG sensor. With shorter sensors, lower optical loss HAF, and advanced FBG interrogation approaches, tens of FBG sensors can be multiplexed in a single fiber to perform cryogenic fuel level/distribution sensing in extreme temperature and gravity environments. The sensing multiplexing capability was demonstrated in both a four FBG array with different Bragg wavelength and a three FBG array with overlapping Bragg wavelength. Using FBG in 1-cm section of 0.5-dB/cm HAF, less than 15% light in fiber core was absorbed by each sensor. To increase the number of sensors multiplexed in one fiber, HAF with less attenuation or shorter sections of HAF could be employed (e.g. FBG in 2-mm, 0.2dB/cm HAF) can be used. This is feasible since the heating of just a few Kelvin above ambient is sufficient for level sensing.

4.3   CONTINUOUS LEVEL SENSING USING RAYLEIGH SCATTERING

Liquid level sensors are usually divided into two categories: discrete level sensors and continuous level sensors. Discrete level sensor detects the liquid level at a single location and provides true/false information of whether the liquid level is above or below the sensing location. Numbers of discrete level sensors can be multiplexed at different positions on a single fiber to provide quasi-distributed sensing performance over long distance. But this capability is fundamentally limited by the multiplexing density of the discrete sensors and the consequent

high manufacturing cost. On the other hand, continuous level sensors detect the liquid level in a certain range and provide quantitative information of the percentage that the liquid of interest has continuously occupied in the sensing range. This fully distributed sensing capability makes continuous level sensor preferable in most level sensing applications.

A majority of continuous fiber level sensors are based on the optical discrimination between refractive index (RI) of liquid and gas phases. Current RI-based continuous fiber level sensors are able to provide sub-millimeter spatial resolution with very fast response time. But the sensing distance is fundamentally limited by the length of the optical tap, which is typically no more than 100-200 mm. The other issue with the refractometric approach is that for cryogenic fluids such as liquid hydrogen and liquid helium, their RI values are very close to their gaseous forms, which makes the RI discrimination impossible. Alternative sensing mechanism is needed for these low RI fluids. Guo *et al.* [28] reported a mechanical-optical method for continuous level sensing, in which the bending of cantilever due to liquid occupation was interrogated using a FBG sensor. This approach provides precise continuous level sensing over extendable distance and temperature independence around room temperature. But its cryogenic temperature performance is susceptible to large thermal expansions mismatch between optical fiber and metal cantilevers over wide temperature range.

In this section, we reported a continuous liquid level sensor for both room and low temperature fluids using self-heated fibers as sensing device. It is based on the Optical Frequency Domain Reflectometry (OFDR) measurement of in-fiber Rayleigh scattering. This technology has been applied to provide distributed sensing solution for in-fiber temperature and axial strain [6-7]. In this section, both electrically and optically heated optical fibers are used to extend its application for liquid level sensing. Distinct heating response of liquid is discriminated

from gas to measure the liquid level with millimeter spatial resolution. Level sensing operations were performed for pure water at room temperature, liquid nitrogen at 77K and liquid helium at 4K. The sensing distance can be extended to more than 70 meters. The employment of commercially available metal-coated fiber and high attenuation fibers as the sensing device completely avoids the difficulties and costs in manufacturing specialized fiber sensors. The proposed sensing system provides a low-cost, long working distance, high resolution and all-temperature solution to liquid level sensing applications.

Proof-of-concept liquid level sensing experiments were performed using deionized water at room temperature (24°C). The experimental setup is illustrated in Fig. 4.9a. A commercial OFDR unit from Luna Technologies (OBR 4600) was employed and butt-coupled with a piece of single-mode fiber with 20-µm thick Copper alloy coating (Oxford). Regulated current is applied to the metal surface of the fiber to generate resistive heating on the fiber, as shown with in the right of Fig. 2a. The heat is transferred into the fiber core and generate spectral shift of Rayleigh signal. The OFDR unit consists of a tunable laser source from 1520-1610nm and a pair of highly sensitive photodiodes with sampling rate of 2MS/s. According to the sensing principles described in the previous part, the spatial resolution of the Rayleigh signal is ~10-µm; the maximum sensing distance is ~70-m. The electrically heated fiber was folded and fixed with fiber holders on a translation stage and inserted into the ionized water.
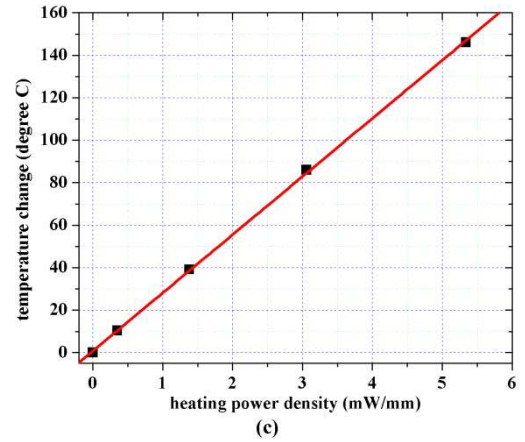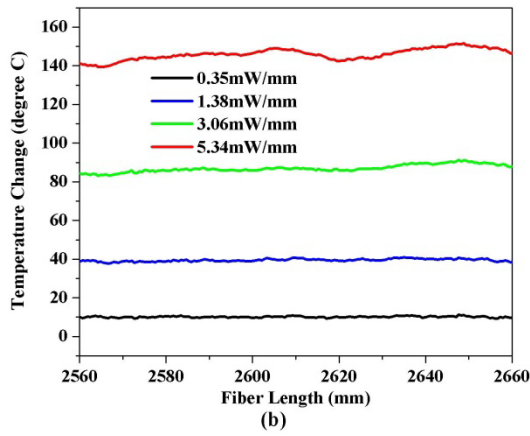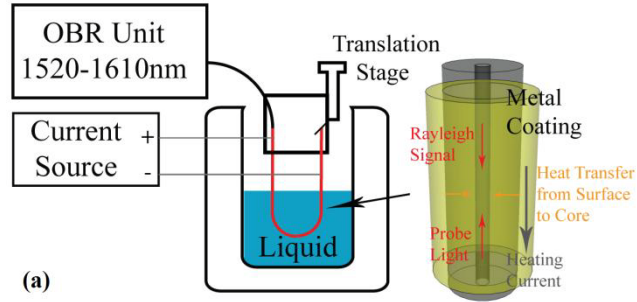
Figure 4.9 Electrical on-fiber heating for continuous liquid level sensing

(a) The schematic of electrical on-fiber heating for liquid level sensing; (b) The uniform temperature profile using different heating power measured by in-fiber Rayleigh scattering; (c) The maximum temperature rise vs. input electrical power density.

Fig. 4.9b and 4.9c shows the electrical on-fiber heating results in air derived from OFDR Rayleigh measurements. Thermal-optic coefficient of -1.6°C/GHz is used for the copper coated fiber [7], which is twice larger than the value for conventional Corning SMF-28 fiber. With low input power, for example 0.35mW/mm input power density for 613-mm long fiber with 0.214A current at 1V, the fiber core is heated up by 10°C uniformly along the fiber. When the input power on the fiber increases, the fluctuation in temperature profile became more pronouncing, which could be attributed to the coating imperfection and the influence of air flows. With 5.34mW/mm input power, the fiber core is heated up by 145±5°C. The linear dependence of temperature rise vs. input heating power density as shown in Fig. 4.9c, demonstrates both the precision and flexibility in electrical on-fiber heating using metal coated fiber.
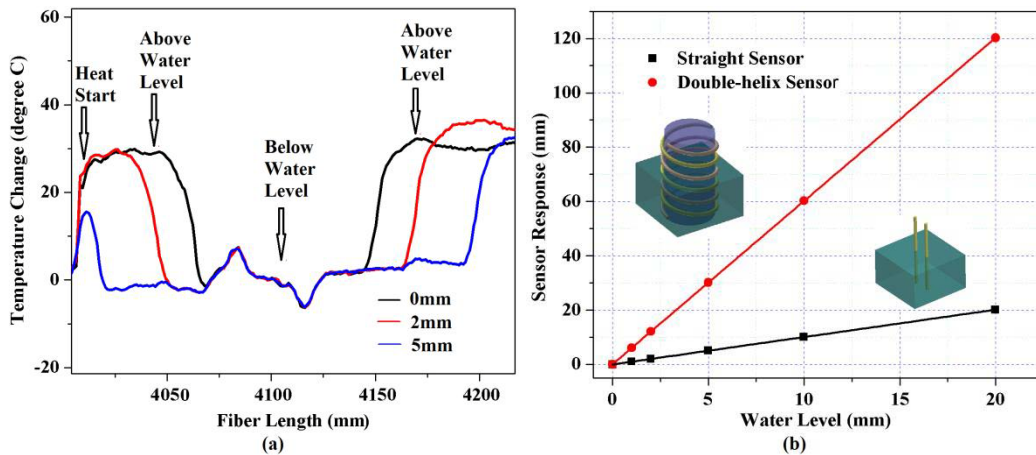
Figure 4.10 Continuous level sensing response.

(a) The temperature profile of the electrically heated fiber during level sensing; (b) The sensor response of both straight and double-helix sensor configuration.

When the heated fiber is dipped into water, abrupt temperature drops are observed in the heating profile, as shown in Fig. 4.10a. This is because the on-fiber heat is taken away from the fiber surface into the surrounding water with heat transfer rate about 1000 times faster than into the air. This abrupt temperature gradient vs. fiber position is interrogated by the in-fiber Rayleigh

signal and serves as the indicator for liquid level position. The temperature profile of the folded sensing fiber at water level of 0mm, 2mm and 5mm (relative to the sensing fiber, reading from the micrometers on translation stage) are shown in Fig. 4.10a. Fig. 4.10b shows the reliable operations of both straight and double-helix folded fiber sensors for water level from 0-20mm. By winding the sensing fiber in two folds on the surface of a 1.5-inch diameter cylindrical post with 2-cm pitch, the level sensing resolution is enhanced by 6 times. Longer level sensing distance is available using extended metal-coated fiber. The maximum probing length for the OFDR unit we use is ~70-m, which could be further extended using faster electronics and longer interrogation time.

In previous part of the paper, water level sensing was performed using double folded self-heated fibers. For both the double-straight and double-helix configuration, two temperature abruptions can be observed in the heating profile at positions symmetric to the fiber folding point. This provides redundancy to the liquid level detection, which can be utilized to interrogate more degrees of freedom in level sensing.

In a comprehensive liquid environment where there are accelerating forces applied to the liquid body other than the gravity, or when the liquid container itself is in motion, the liquid level can be tilted with respect to the level sensing system. Additional to the liquid level position z_T, there are two more parameters in measuring the tilting of liquid level, the tilting orientation θ_T and the tilting angle φ_T.

When the liquid level is tilted away from the normal plane of the level sensing cylinder, as is shown in Fig. 4.11a, the liquid level emposes a cross-section trace on the cylinder surface, which can be express as,

$$z_T = z_0 + x_T \sin\phi = z_0 + r(1 - \cos\theta)\sin\phi \qquad (4.1)$$

60

The curves are plotted on the cylinder surface for $(z_T, \varphi_T, \theta_T) = (0\text{-mm}, 0°, 0°)$, $(0\text{-mm}, 1°, 0°)$, $(0\text{-mm}, 5°, 0°)$, $(0.1\text{-mm}, 5°, 0°)$ and $(0.1\text{-mm}, 5°, 15°)$ as shown in Fig. 4.11b. Traces of an evenly pitched quarto-helix fiber sensor configuration is also plotted on the same figure as,

$$z = a - b\theta \qquad (4.2)$$

The four intersection points on the four fiber lines A, B, C and D with the level curve indicate the sensor responses with the tilted liquid level. Known at least 3 of the 4 response locations, we are able to solve for the three unknown parameters, liquid level position z_T, tilting orientation θ_T and the tilting angle φ_T. In the case of a double-helix sensor, thermal response on line A and C can be interrogated to solve two of the three unknowns.

Tilting experiments were done with tilting orientation fixed at $\theta_T = 0$ for $(z_T, \varphi_T) = (0\text{-mm}, 0°)$, $(0\text{-mm}, 1°)$, $(0\text{-mm}, 5°)$, $(2\text{-mm}, 0°)$, $(2\text{-mm}, 1°)$ and $(2\text{-mm}, 5°)$. The results are shown in Fig. 4c. Asymmetric thermal responses on fiber line A and C were measured to solve for the liquid level position and tilting orientation. The solved values are compared with the actual values in the inset of Fig. 4.11c and good agreements were found.
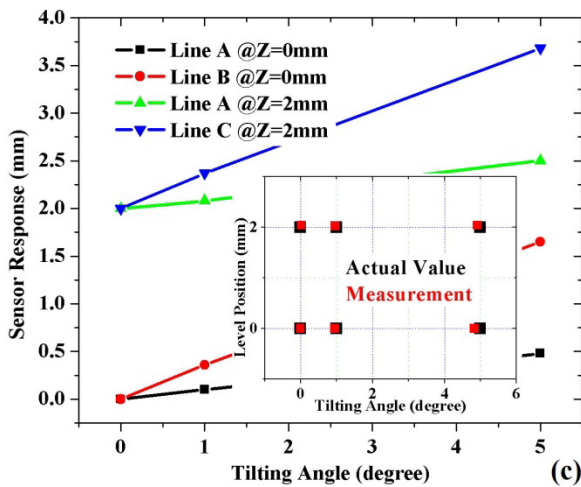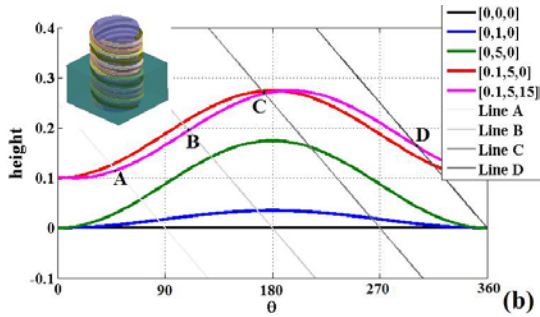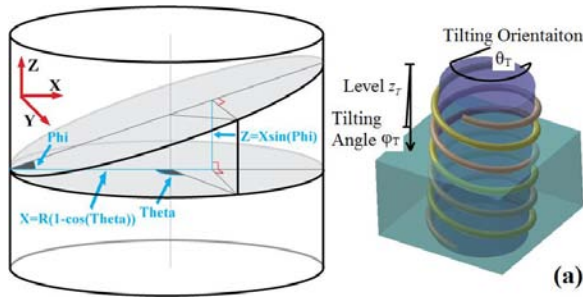
Figure 4.11 Tilted level sensing.

(a) The cross-section of tilted liquid level on cylinder surface and the illustration of the tilting measurement using double-helix sensor; (b) The solvation of measuring the tilting of liquid level z_T, the tilting orientation θ_T and the tilting angle φ_T. from the readings of a quadratic-helix sensor configuration (inset); (c) The experimental results of measuring the liquid level z_T and tilting angle φ_T using a double-helix senor at fixed tilting orientation $\theta_T=0$, inset: the comparison of actual value and measured value for liquid level z_T and tilting angle φ_T.

We have applied electrical current to the metal coating of optical fiber for on-fiber heating. The heating is uniform, low-cost, energy efficient and easy to tune. But there are several disadvantages of the electrical heating scheme for liquid level sensing applications. Firstly the electrical heating current is prone to a variety of environmental perturbations such as electromagnetic interferences (EMI) and environmental conductivity. The exposed electrical current also presents spark hazard in the case of flammable liquid applications. Secondly, although the metal coating serves as a good protection to the optical fiber for impact, stretching and temperature as high as 600°C, the coating is vulnerable to corrosive chemicals, which presents another limitation to the implementation of the level sensing method. Furthermore, at extreme low temperature environment, such as in liquid nitrogen at 77K and liquid helium at 4K, the resistivity of metal decreases dramatically, and more electrical power is needed to heat up the fiber. Thirdly, due to the good thermal conductivity of metal and the outside-in heating scheme, the steep thermal abruption sensed by the fiber core is neutralized by a moderate thermal gradient as wide as 1-cm (as shown in fig. 3a), which hinders further improvements on the spatial resolution of level sensing. Some of the disadvantages can be elevated by various methods including additional isolations outside metal coating and careful tuning of heating current. But other disadvantages are inherent to the electrical on-fiber heating principle, which can only be solved by the deployment of optical heating methods.

Optical on-fiber heating has generated widely interest in fiber sensing applications due to its coherence with the optical fibers. The heating power is delivered optically inside the optical fiber and release the designed sensing actuator region through optical taps. Different optical heating techniques were developed using multimode fibers [13], and more recently, single-mode high attenuation fibers (HAF) [22-23, 29]. Compared with the multimode fiber approaches, using

single-mode high attenuation fibers as the heat release transducer offers precise optical loss control and distributed optical heating capability.
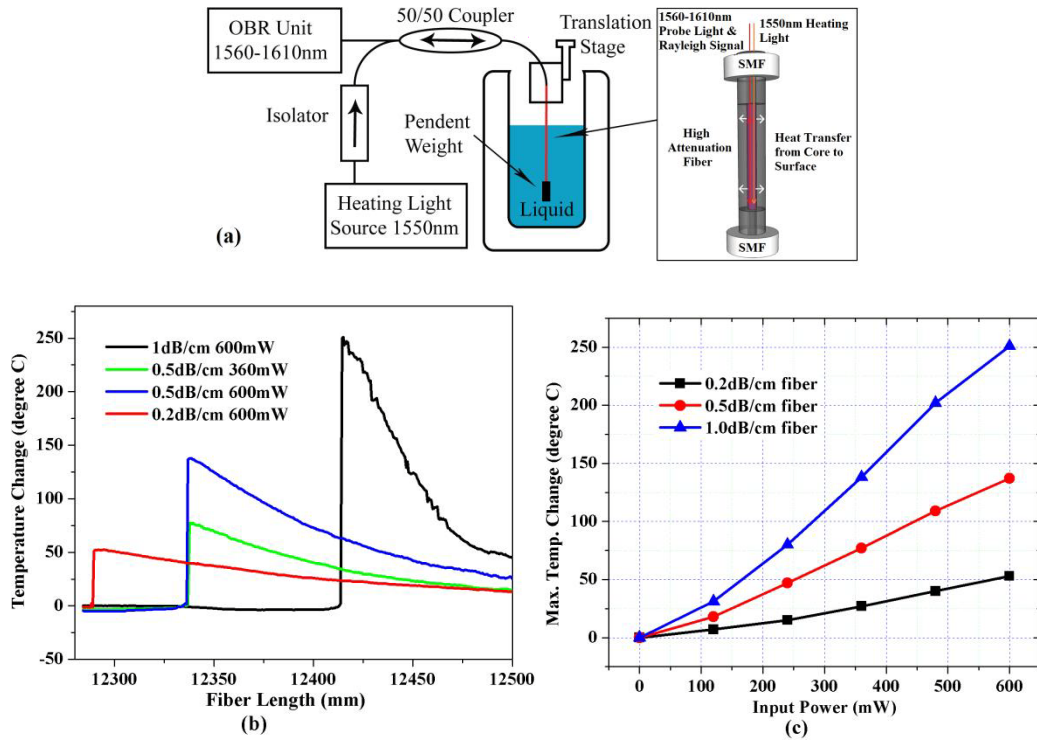
Figure 4.12 Optical heated continuous level sensing

(a) The schematic of level sensing using optically heated fiber; (b) The temperature profiles of different HAF with different heating power; (c) The heating efficiency of different HAF.

The schematic of optically heated fiber level sensor is illuminated in Fig. 4.12a. Light from a coherent CW laser at 1550nm was amplified up to 2-W using an Erbium-doped fiber amplifier (EDFA) as the heating light source. The heating light is combined with the tunable probe light at 1560-1610-nm from the OFDR unit using a bidirectional 50:50 fiber coupler and injected into a piece of HAF with 1dB/cm loss in the single-mode fiber core. Optical power is attenuated and transformed into heat power, which is transferred from the fiber core to the surface and served as the level indicator. The in-fiber heating profiles of HAFs with different loss at different optical heating power are interrogated with spatially resolved Rayleigh signal in

64

the air. The results are shown in Fig. 4.12b and 4.12c. Contrary to the uniform heating profile of electrically heated fiber, exponential decays of temperature are observed due to the core attenuation. With 600mW input power, 1dB/cm loss HAF can be heated up by 251°C at maximum. With a less lossy HAF of 0.2dB/cm, the fiber can be heated up by 30-50°C in a 30-cm long region.
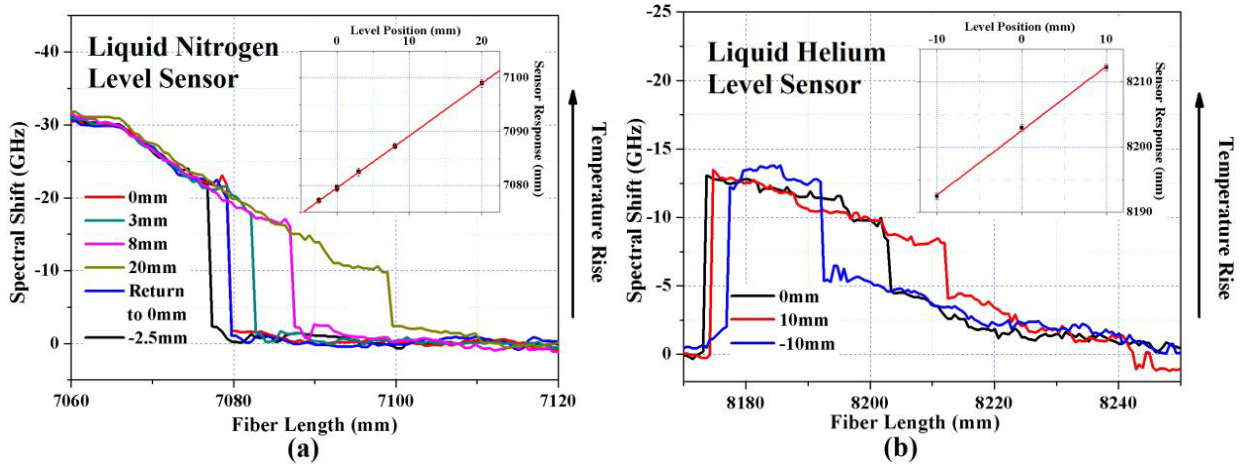
Figure 4.13 Level sensing response in liquid nitrogen and liquid helium

For cryogenic liquid level measurement, the HAF is suspended from a translation stage down to the cryogenic dewar. The fiber is kept straight using a 5g pendent weight. This eliminates the need of metal supporting structures and avoids any fiber bending caused by the thermal expansion mismatch between silica fiber and metals. When the optical heating is turned off, the temperature gradient around the liquid level is measured as the reference. With the optical power turning on, the temperature profile along the fiber is measured again and compared with the reference to eliminate any crosstalk from environmental temperatures. Because the thermal-optic coefficient of HAF at cryogenic temperature is unknown, we use the Rayleigh spectral shift values instead of temperature to describe the measured temperature changes. The level sensing results for liquid nitrogen at 77K and liquid helium at 4K are shown in Fig. 4.13a

and 4.13b respectively. For both liquid, the temperature changes at liquid levels are steeper than the case for electrically heated level sensor. The abruption width is ~1-mm for heated HAF, while with the value is ~10-mm for heated metal coated fiber. This is due to both the inside-out heating approach and the elimination of thick metal coating. The optically heated HAF level sensor demonstrates higher spatial resolution but shorter sensing range compared to the electrically heated metal coated sensor.

In summary, we present a continuous liquid level sensing system that is able to detect liquid levels for both room temperature and cryogenic fluids. The simplicity, low cost, wide application range, high sensitivity and long sensing distance of this technique make it a unique solution to liquid level sensing application.

5.0   GAS FLOW SENSOR

Measurements of the gas and liquid flow rates are essential to a wide range of applications, including weather and environmental monitoring, industrial process control, and gas/liquid pipeline operations. Among a variety of flow-meter designs, the classical hot-wire anemometry (HWA) is most widely adopted for industry applications due to its simple design and reliability. In a HWA, the flow rate is determined by interrogating the heat removal rate from hot wires/films by the blowing gas/liquid [39]. Thanks to the development of micro electro mechanical systems (MEMS) technology in the last 20 years, miniature HWAs can be fabricated on chip to perform single-point flow measurements with high sensitivity, fast response time, and minimum power consumption [40]. However, in many industrial setting, flow sensing applications such as detecting gas pipe leaks, or monitoring gas flows in combustion engines, the scale of the flow field and harsh working environments post significant challenges to the existing HWA flow sensors. For example, to fully characterize the three dimensional vector flow field, large amount of hot wire sensors are needed to measure both magnitudes and directions of the flow field. This incurs cost and wiring difficulties especially at cryogenic or high temperatures or in corrosive and radioactive environments.

As have been discussed in the previous chatpers, fiber optic sensors are well-known for both working under harsh environment and the capability of sensor multiplexing, thus become a good candidate for harsh environment flow measurements. Many fiber flow sensors have been

reported using different measurement schemes, including Doppler anemometer [41], bending flow sensor [42], and fiber HWAs [17, 43-45]. For fiber based hot-wire flow sensors, a variety of delicate on-fiber heating designs have been proposed, including using single-mode-multimode tap [17, 43], long period grating (LPG) [44], and high attenuation fibers [45]. Local gas flow rate is associated with the flow-induced temperature drop, which is measured by the Fiber Bragg gratings (FBGs) inscribed in the heat release area of the fiber. The sensitivity, response time and dynamic range of HWA can be controlled by changing the on-fiber heating profile. Efforts have also been made to obtain multi-dimensional flow information. An X-probe configuration using two multiplexed fiber HWAs was also reported for simultaneous measurement of flow magnitude and direction [17]. By multiplexing many heated FBG sensors in one fiber, flow rate at multiple locations can be interrogated for many harsh environment applications. However, the spatial resolution of the flow field measurement is limited by FBG sensor multiplexing density and the associated manufacturing cost.

To characterize the vector flow field using fiber optic sensors, it is required to perform truly distributed fiber sensing operations with high fidelity. Optical frequency domain reflectometry (OFDR) technology has been developed in the last thirty years for the purpose of ultra-fine resolution distributed sensing. Compared with optical time domain reflectometry (OTDR), the resolution of which is limited to ~0.1-1-m range by the temporal resolution of the system, OFDR provides superior spatial resolution down to ~10-µm with frequency-space conversion technique [46-47]. On the other hand, due to the sweep-wavelength interferometry nature of OFDR, inelastic in-fiber scattering processes such as Raman and Brillouin scattering cannot be used in OFDR scheme for distributed sensing. Recently, integration of in-fiber Rayleigh backscattering measurements with OFDR technology were reported by M. Froggatt, *et*

al., and has been employed for a variety of applications including fiber diagnosis [48] and distributed sensing of multiple parameters such as temperature [6-7], strain [27, 49], and pressure [50].

In this chapter, we proposed a multi-layer hot-wire grid anemometer using a single piece of self-heated fiber without the need of FBG sensors. By spatially resolving the in-fiber Rayleigh backscattering signal in the heated fiber using the OFDR technique, temperature profiles along all sections of the heated fiber grid are measured and synthesized to generate a comprehensive picture of the gas flow vector field, including the rate, position and direction of the flow field with millimeter spatial resolution. By using a single piece of fiber as the sensing device, the proposed sensor design completely eliminates the needs and associated costs for large number of FBG point sensors, thus provides a low-cost, reliable and powerful tool for comprehensive flow sensing applications for all environments.
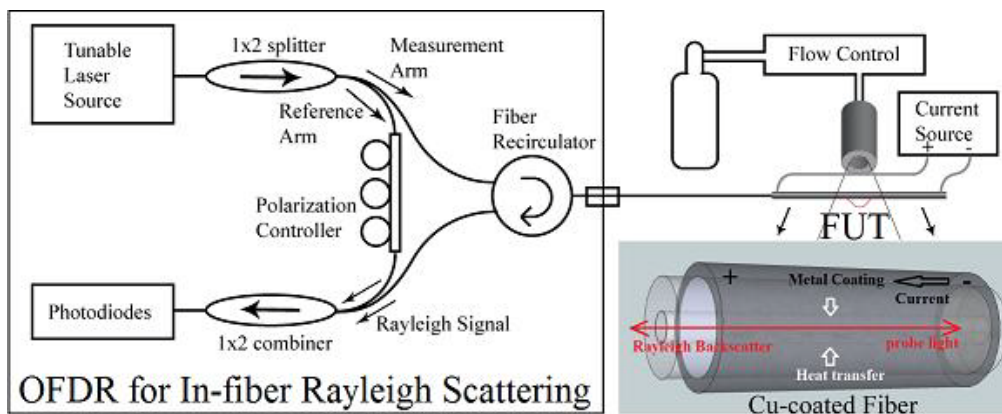
Figure 5.1 Schematic of in-fiber Rayleigh scattering measurement for flow sensing.

The principle of flow sensing using spatially resolved Rayleigh scattering in self-heated fiber is illuminated in Fig. 5.1. The basic principle has been discussed in chapter 2. To apply the OFDR technique for flow sensing, a commercial OFDR unit (Luna Technologies, OBR 4600) is butt coupled to a piece of metal-coated fiberas the FUT. With 90-nm wavelength tuning range at

1560-nm central wavelength and 2MB/s sampling rate, the maximum interrogation fiber length and spatial resolution are 70-m and 10-µm respectively according to the formula in Chapter 2. When a 1-cm long cross-correlation window is applied for the measurement and reference Rayleigh spectra, local temperature can be measured with 0.1°C accuracy with conventional optical fibers. The FUT was a piece of single-mode telecom optical fiber with 9-µm diameter Ge-doped core and 125-µm cladding, coated with 20-µm thick of Copper alloy, which is commercially available from Oxford Electronics (SM1300-125CB). Electrical current is applied to the metal surface of the fiber to generate resistive heat along the fiber, which can be spatially interrogated using the in-fiber Rayleigh scattering unit. When gas flow is blowing on a section of the FUT, the OFDR Rayleigh measurement is taken and compared with the first measurement without the gas flow. The magnitude and position of flow-induced heat loss is determined by the temperature drop along the heated fiber.

5.1   FLOW SENSING WITH ELECRICAL HEATED FIBER

Fig. 5.2a shows the temperature profile of a piece of electrically heated fiber from OFDR Rayleigh measurements without the gas flow with various input electrical heating power. Effective temperature response coefficient of -0.67GHz/°C [7] is used for the 20-µm thick copper-alloy coated fiber to correlate the measured Rayleigh spectral shifts with distributed temperature changes. The non-uniform temperature profile can be attributed to the coating imperfection. When the input power increases, the imperfect coating causes similar temperature profile along the fiber. The tunability of electrical on-fiber heating is further demonstrated with the dependence plot of on-fiber temperature rise vs. input power density in Fig. 5.2b. The

temperature dependence of fiber resistance is shown in Fig. 5.2c, which explains the slight nonlinearity revealed by Fig. 5.2b.
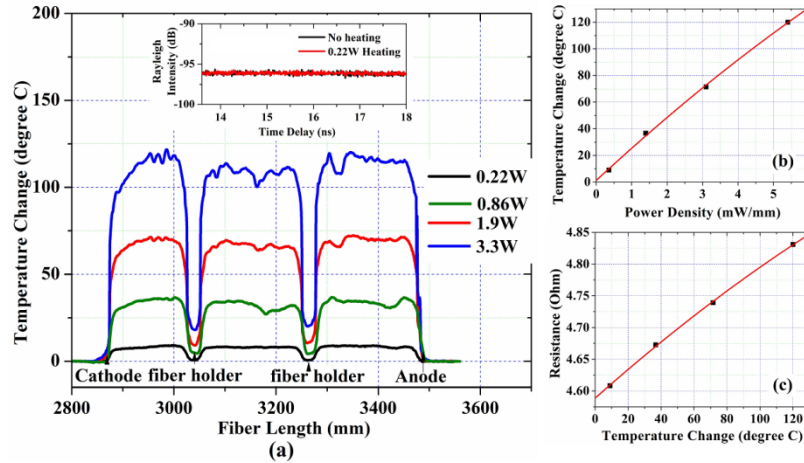
Figure 5.2 Temperature profile of electrically heated fiber

(a) The heating profiles along the FUT for different input power, derived from the cross-correlation between unheated and heated Rayleigh spectra; Inset: unheated and 0.22W heated Rayleigh spectra (b) The heating efficiency vs. input power density, values obtained at fiber length of 3470mm in 2a; (c) The temperature dependence of resistance.

To simultaneously determine the magnitude and direction of the gas flow, a single heated fiber is folded into two parallel hot optical wires spaced 10-mm apart as shown in insets of Fig. 5.3. In this configuration, gas nozzles were arranged in the same plane of the two hot wires. This allows the determination of flow direction in the same plane as the hot optical wires. The optical fiber is electrically heated to ~110°C above the ambient temperature. Multiple flow parameters are interrogated using this configuration, which include flow rate, transverse position and tilting angle of the flow vector, and multiple flows.

71
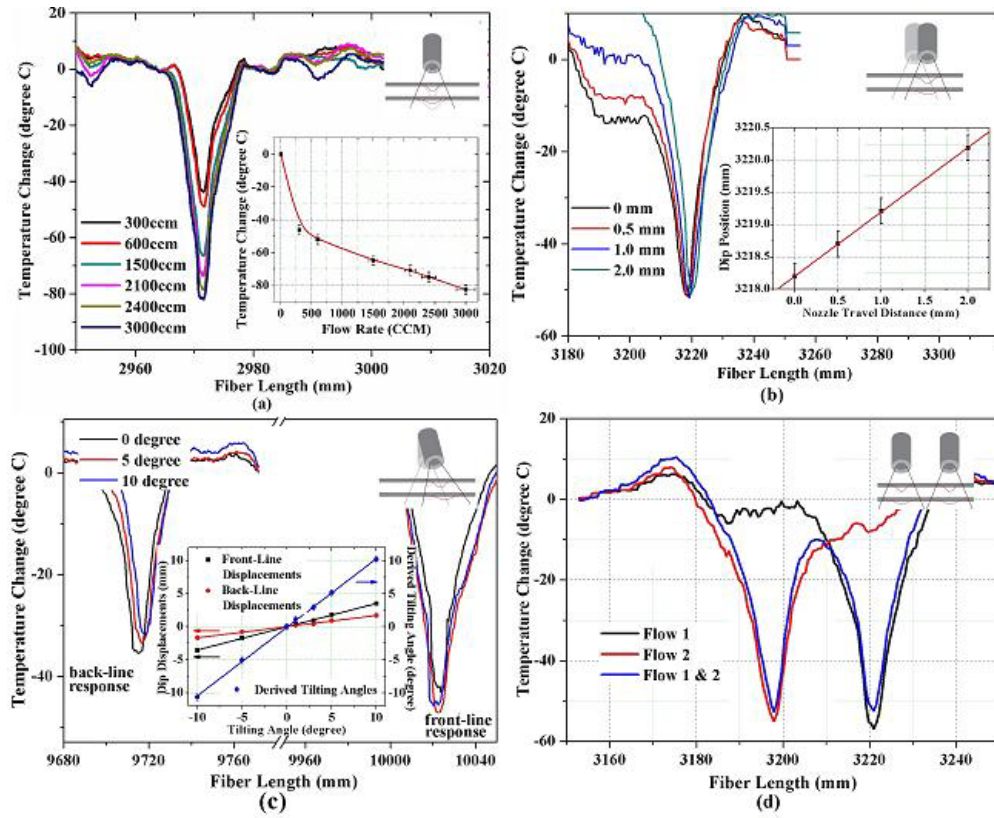
Figure 5.3 Single fiber HWA responses

The heat loss profiles and sensor responses of (a) flow rate measurement; (b) flow transverse position measurement; (c) flow direction measurement (d) two gas flows measured simultaneously.

Fig. 5.3a shows the thermal response of the front-line hot optical wire to 300-3000-ccm (cubic centimeter per minute) gas flows blown from a ¼-inch nozzle 5-mm away. Flow rate of nitrogen gas is regulated with a calibrated mass flow controller, with 1000-ccm corresponding to 0.527m/s at the nozzle. To simplify the model, we assume laminar flow in our discussion. According to the HWA theory [39], the heat loss H_{loss} can be related to the flow rate v as,

$$H_{loss} = \Delta T \left(A + B \sqrt{v} \right) \qquad (7)$$

where ΔT is the temperature rise on the HWA, A and B are empirical coefficients. For flow rates increased from 300-3000-ccm (0.158-1.58-m/s at the nozzle), the inset of Fig. 5.3a shows the

72

decreasing of dip temperatures from -46°C to -80°C. With electrical heating power density of 5.4-mW/mm, A = -0.026-mW/mm/°C and B = 0.011-mW/mm/°C/(m/s)$^{1/2}$ were obtained from curve fitting. The flow sensitivity at 0.263-m/s (500-ccm) is 0.014-m/s/°C.

In additional to the conventional flow rate measurement, transverse position of the flow can also be monitored with the thermal profile of the hot optical wires, as shown in Fig. 5.3b. The inset shows the 1:1 linear dependences of the Gaussian-fitted dip position on the hot optical wire to the reading on translation stage of the gas nozzle. Sub-millimeter transverse movements of the gas-blowing nozzle can be readily differentiated with ±0.2-mm resolution.

Furthermore, tilting of the gas-flow directions can be discriminated from transverse movements using the two parallel hot optical wires configuration. As is shown in Fig. 5.3c, with a tilting flow, the frontline heat loss profile is moving to the left positions and backline profile to the right due to the fiber folding. Tilting angle θ_x can be related to the deviation difference using basic trigonometric calculation as,

$$\theta_x = \arctan\left[\left(\Delta x_{back} - \Delta x_{front}\right)/d\right] \qquad (5.1)$$

where Δx_{front} and Δx_{back} are the deviation of front and backline dip position respectively, and d is the spacing between front and backline, set as 10-mm. The inset of Fig. 5.3c shows the measured Δx_{front} and Δx_{back}, and the derived θ_x for actual tilting angles from -10° to +10°. Good sensing accuracy with less than 5% error is obtained, which could be further enhanced with larger spacing d. Fig. 5.3c also shows that the temperature change and flow sensitivity decreases with larger nozzle-fiber distance. The sensitivity at the backline fiber is approximately 25% smaller than that of the frontline fiber.

Finally, multiple gas flows can be detected at the same time. We alternatively turned on and off two independent gas flows 23-mm apart from each other, and the measured thermal

profiles clearly verified our operations, as is shown in Fig. 5.3d. To measure flow directions in two-dimension (2D) simultaneously, a 15-section two-layer 2D grid is formed using a long piece of heated fiber in 4×4+3×4 configuration as shown in Fig. 5.4a and 5.4b. They are labeled as X1/Y1 front grid and X2/Y2 back grid separated by 10 mm. The X1 horizontal fiber lines are separated from the Y1 vertical fiber lines by 5-mm. So is the case for the X2 and Y2 fiber lines.The backlines are also interleaved between frontlines, as is shown in the insets of Fig. 5.4d and 5.4e. When a gas flow is applied to the grid, all 15 possible heat loss dips are monitored with a single scan, as is shown in Fig. 5.4c. The 2-D hot optical grid allows the determination of the 2D location of the gas nozzle (x, y) and the blowing directions (θ_x, θ_y) simultaneously. Fig. 5.4d-e presents an example of the calibration process. Fig. 5.4d shows the heat loss amplitudes with constant gas flow of 1200-ccm, when the flow is travelling in Y-axis direction from -5-mm to +10-mm, passing two frontlines and two backlines of optical hot wires along the x axis. Fig. 5.4e shows the same heat loss amplitude correction measurement for flow tilting angle from -10°C to 10°C in Y-axis. A flow attenuation matrix for $v_{measured}$ can be constructed using this calibration process for both X and Y axes. Using the calibration matrix, we took two measurements at actual 2-D positions of the nozzle and flow rates of (x=3.0 mm, y=3.0 mm, 1800-ccm) and (x=-2.0 mm, y=-4.0 mm, 1200-ccm) at (θ_x=0°, θ_y=0°) and retrieved the measured position and flow rate values, as are shown in Fig. 4f. Another two measurements were taken for actual 2-D tilting angles and flow rates of (θ_x=-3.0°, θ_y=-3.0°, 1800-ccm) and (θ_x=5.0°, θ_y=5.0°, 1200-ccm) at (x=0 mm, y=0 mm) and the measured values are also retrieved from the calibration, as shown in Fig. 5.4f. For both cases, the measured and actual values showed good agreements with maximum offsets <4% in the 3-D measurement spaces.
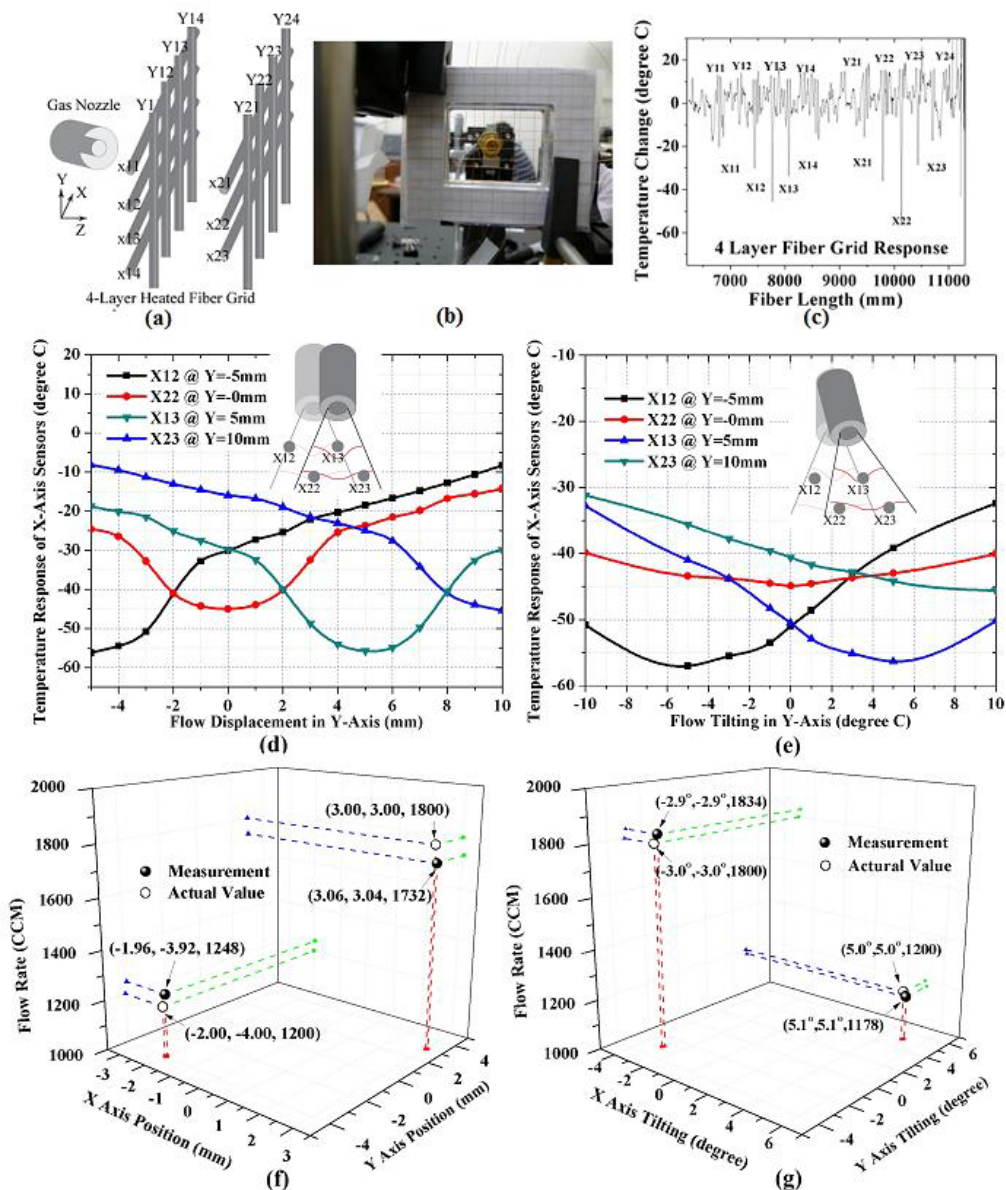
Figure 5.4 Fiber grid flow responses

(a) The schematic and (b) the picture and (c) the flow response of a 4-layer fiber hot-wire grid with 15 HWA sections; (d, e) The calibration curve of flow rate with longitudinal movements and angle tilting; (f, g) The comparison between measured and actual values of flow rate, positions and angles.

5.2   FLOW SENSING WITH OPTICAL HEATED FIBER

The electrical on-fiber heating is uniform, low-cost, and energy efficient. But several disadvantages limited its employments in advanced sensing applications. The electrical heating current is prone to electromagnetic interferences (EMI), and environmental conductivities. It also presents spark hazard with flammable gas. The metal coating is vulnerable to corrosive chemicals, and the resistivity of metal decreases dramatically at low temperature. To overcome these problems, we proposed replacing electrical heating with optical on-fiber heating using single-mode high attenuation fiber (HAF). The idea of heating a piece of single-mode fiber internally via the absorption of optical power in HAF was first proposed by Coric et al. [19], and was employed for a variety of fiber sensing applications including room and cryogenic temperature liquid level sensors [23, 29, 38], cryogenic hydrogen gas sensors [22], and gas flow sensors [45]. As illustrated in Fig. 5a, >1W amplified heating light at 1550-nm is combined with the tunable light at 1560-1610nm from OFDR unit using a bidirectional fiber coupler and injected into HAF under test. Optical power is attenuated in the HAF core and transformed into heat power and transferred to the fiber surface. Fig. 5c shows the temperature profile and heating efficiency of an optically heated 0.05-dB/mm loss HAF. Contrary to the uniform electrical heating, exponential decays of temperature changes along the HAF were observed due to optical attenuation. With 600-mW input optical power at 1550-nm, the HAF can be heated up by 50-140°C in 100-cm fiber length. The smooth and stable temperature profiles due to internal fiber heating provide an excellent test-bed for gas flow sensing. The sensor responses of 0-500-ccm (0-0.263-m/s) gas flows from a ¼-inch nozzle 5-mm away are shown in Fig. 5.5d. The dip temperatures decreased from -10°C to -31°C for flow rate from 50-500-ccm (0.0263-0.263-m/s). With optical heating power density of 6.8-mW/mm at fiber length position of 16-mm, A = 0.067-

mW/mm/°C and B = 0.19-mW/mm/°C/(m/s)$^{1/2}$ were obtained from curve fitting. The flow sensitivity at 0.263-m/s (500-ccm) is 0.020-m/s/°C. This value is slightly larger than the sensitivity obtained with electrical heating scheme.
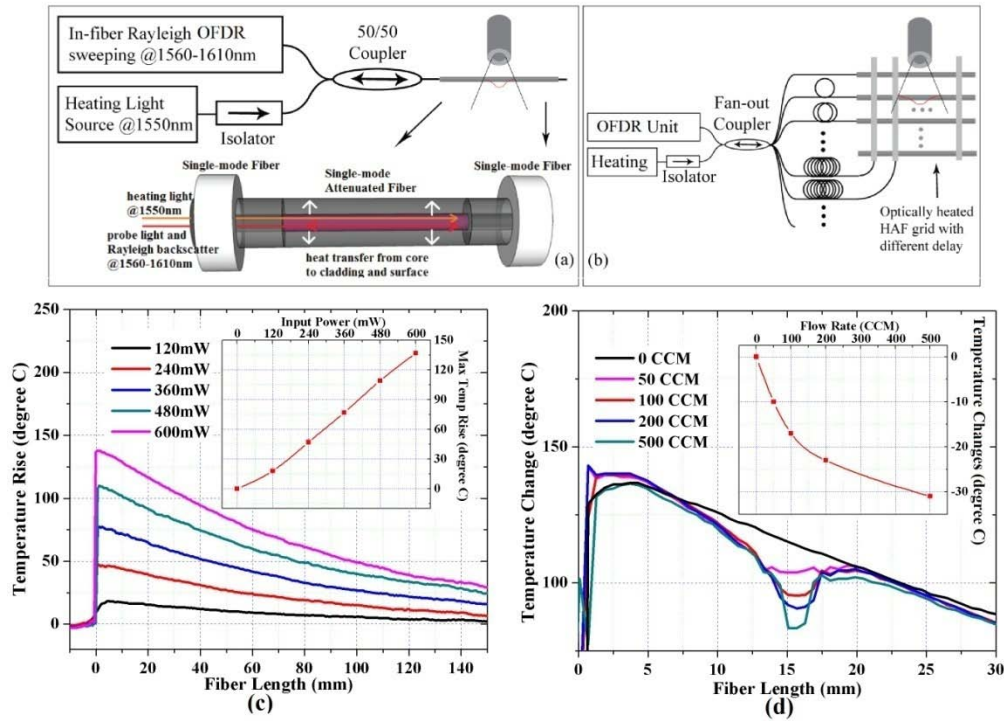
Figure 5.5 Optically heated fiber flow sensor

(a) The schematic of flow sensing using OFDR and optical on-fiber heating; (b) Proposed setup for optically heated HWA grid; (c) The temperature profile and heating efficiency (Inset) for optical heating using 0.05dB/mm-loss HAF; (d) The flow sensor response and rate dependence (inset) using optical on-fiber heating.

Due to the nature of optical attenuation, optical-heated fiber sensing grid cannot be formed in serial. A parallel grid is proposed as shown in Fig. 5.5b to perform comprehensive flow measurement. The OFDR unit and heating light are coupled into parallel-multiplexed HAF HWAs, each having different optical delays to avoid spatial overlapping in Rayleigh measurements. Compared with the electrical heating, the optical heating scheme fully exploited the advantages of fiber optic sensing, and are more suitable for flow sensing applications in

extreme environments such as strong EMI, conductivity and chemical corrosions. The parallel-multiplexed grid configuration is also more reliable than using a single piece of electrically heated fiber. On the other hand, the optical attenuation and consequent non-uniform heating profile associated with optical heating scheme limited the dimensions and dynamic range of the measurements.

In conclusion, this chapter presents a distributed fiber optical flow sensor using optical heated wire anemometry. The flow-induced heat loss profile on the fiber is spatially interrogated using OFDR Rayleigh scattering signals. By synthesizing the profile on every HWA section in the grid, comprehensive flow information including flow rate, position and direction was obtained with a single OFDR scan on a single fiber using one fiber feedthrough. Both electrical and optical on-fiber heated flow sensing were demonstrated to suit different sensing environments. Discrete gas flows and non-uniform flow fields can be identified with 1-cm resolution, while the displacement and tilting of individual flow can be tracked with sub-millimeter special resolution and <1° angular resolution. The high spatial resolution, simple installation, and wide adaptability to wide ranges of harsh environments make this sensing scheme useful for a wide range of industrial sensing applications.

6.0   HIGH TEMPERATURE PRESSURE SENSING

6.1   REGENERATED GRATING

As was have discussed in previous chapters, FBG sensors are the primary choice for real-time distributed sensing systems, for monitoring different environmental parameters spontaneously. But the conventional type I FBG with hydrogen photosensitization and UV inscription is not stable at >500°C. High temperature annealing gradually erases the UV induced index modulation, which prevents the applications of type I FBG in high temperature environments such as oil field and chemical engineering.

The gratings inscribed by multiphoton excitation with high intensity ultrashort laser pulses are usually referred as the type II gratings. The type II gratings are damage written gratings with the laser intensity exceeding the damage threshold of silica. The amorphous network of the glass is usually transformed via the ionization and melting pathway to give either higher index changes or create, through micro-explosions, voids surrounded by more dense glass. Although the type II gratings have been successfully demonstrated its capability for high temperature use, its involvement of ultrafast laser in the fabrication makes them relatively complicated and costly in comparison with the type I gratings. Type I gratings are known as standard gratings and are manufactured in fibers of all types under hydrogenation conditions. These gratings can in principle operate up to 300 $^{\circ}$C as aforementioned. It is desired to produce

high temperature gratings using type I gratings, thus to retain the best features of the current fabrication capabilities imposed on telecommunications.

The recently reported regenerated grating technique is promising way to extend the working range of the type I gratings into high temperature region [51-55]. The regenerated gratings grow through processing at high temperatures after the seed grating written by UV light is erased. In 2007, Zhang and Kahrizi reported for the first time that the fiber Bragg gratings can be regenerated through high temperature annealing treatment [51]. The germanium doped fiber was used and the FBG was fabricated through the conventional hydrogen loading process. By annealing the gratings at around 1000 ^{o}C, the highest erasing temperature reached 1100 ^{o}C. In 2008, Canning et al. fabricated the regenerated gratings in boron-codoped optical fiber written with 193 nm UV laser which can withstand temperature beyond 1000 ^{o}C[52]. They further pushed the temperature up to 1295 ^{o}C by using a modified ultrahigh temperature micro heater to anneal the gratings [53]. This thermal regeneration technique was also applied the complex gratins such as Moire gratings [54]. Although in the aforementioned reports the hydrogen loading was applied, the described processes are unlikely to be confined to silica fiber with hydrogen as some recent results indicated. For example, some German researchers reported regenerated gratings in non-hydrogen-loaded photosensitive fiber [55].

The implication of this regeneration process is that the index change of silica can be engineered by glass structure transformation using high temperature processing rather than relying on a diffusive interpretation as the basis for grating writing. This approach implies that the lifetime and operational thresholds of the conventional gratings can be extended to a level not previously thought possible.
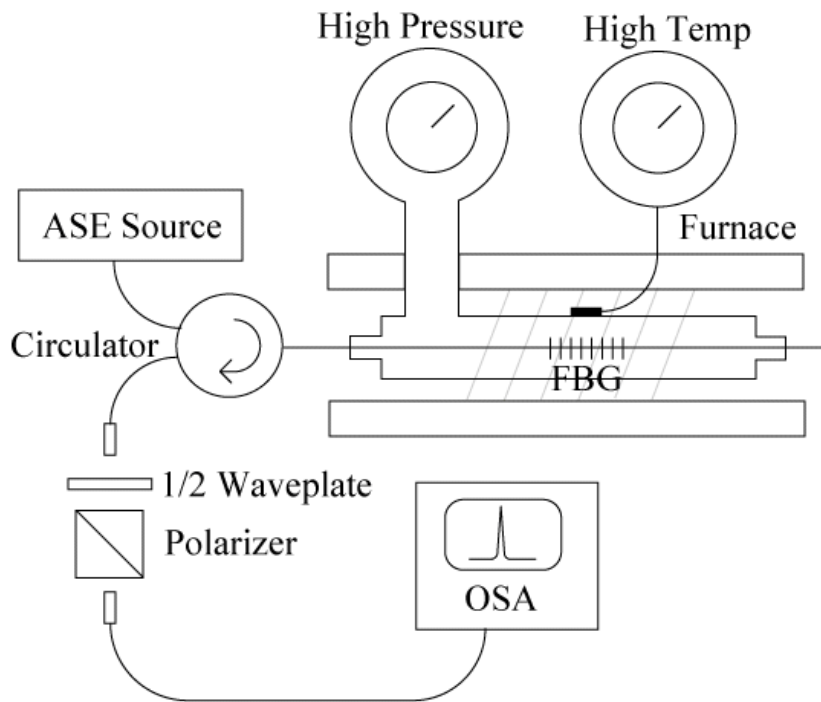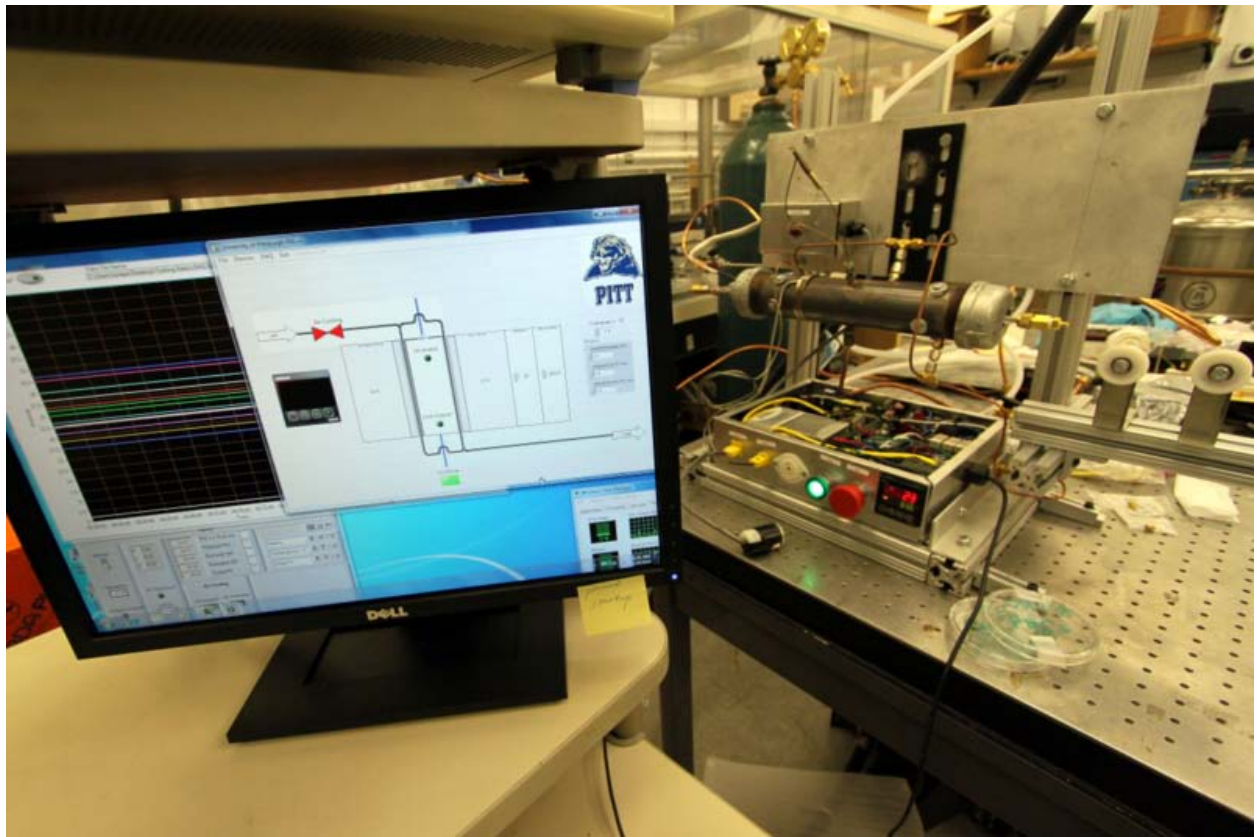
Figure 6.1 home-made furnace setup for fiber annealing and high pressure test.

We have developed two fiber heating and high temperature testing setup in our lab. And the latest one is shown in figure 6.1. The home made furnace is able to heat up to 1100°C, and reaches 800°C in less than 4 minutes with minimum temperature overshot and rippling. A pressure sealed fiber tube is placed inside the furnace for possible temperature, pressure and chemical dependent testing. The operation of the furnace and the interrogation of FBGs are fully automated with Labview program on a personal computer.
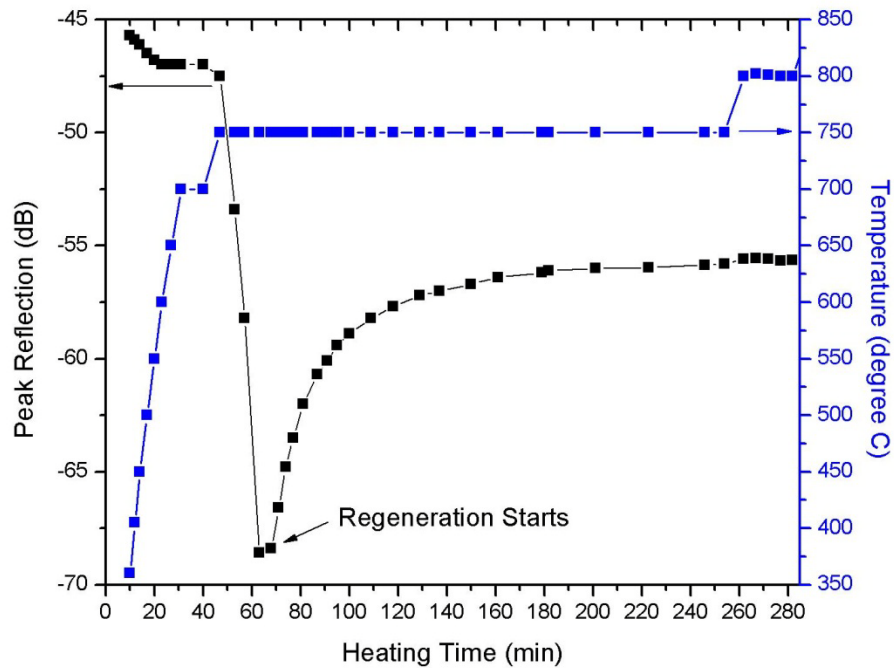
Figure 6.2 Regeneration of FBG with isochronal annealing.

Figure 6.2 and 6.3 shows the thermal regeneration of a type-I FBG using our heating furnace. A strong FBG was inscribed in Corning SMF-28e fiber. The details of FBG fabrication process was described in Chapter 2 of this thesis. A 0.23nm wide flat-top FBG with reflection >99.9% was put into the high temperature testing chamber. After ramping up the temperature to 750°C, the FBG intensity diminished to background in less than 15 minutes. And then a

regenerated FBG peak appears in longer Bragg wavelength, and was stabilized in about 3 hours.

The regenerated FBG is 12dB weaker than the original one, and is tested stable at 800°C.
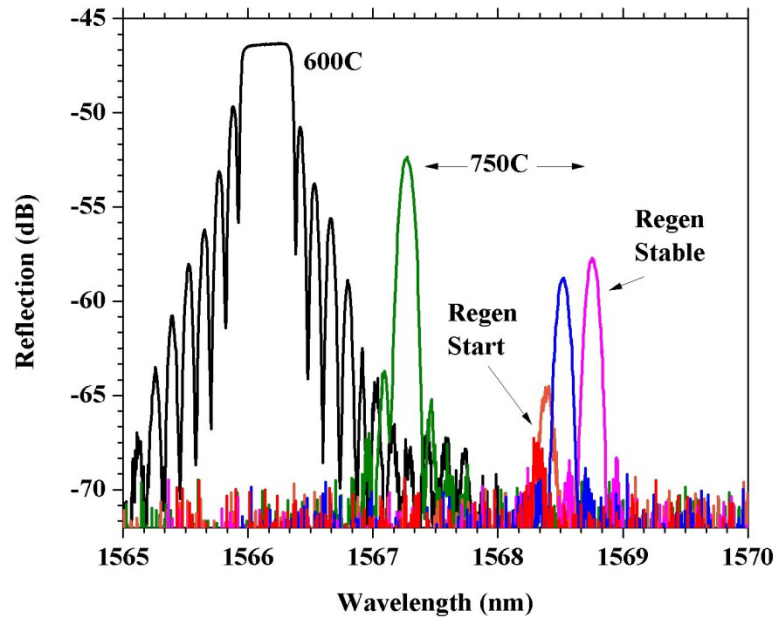
Figure 6.3 Evolution of FBG peak during thermal regeneration

6.2   TWIN-HOLE FIBER FOR PRESSURE SENSING

Hydrostatic pressure measurements for high temperature environments are uniquely demanding and challenging for a wide range of applications in energy industry. Fast, accurate and reliable interrogation of gas pressure information ensures safe and efficient operations of gas turbine, coal boilers, power plants, and etc, where the operating temperatures range from 400°C to more than 1000°C. Fiber optical sensors have always been considered as good candidates for harsh environment applications. In the past few years, high temperature pressure sensors based on Fabry-Peròt interferometry (FPI) have been successfully demonstrated [56-58]. On the other

hand, fiber Bragg-grating (FBG) based sensors, in which Bragg wavelength shifts are interrogated with respect to environmental changes, have small in-line loss, good sensing resolution and wavelength and temporal multiplexing capability compared with FPI type sensors. Hundrends of type-I FBGs with same or different Bragg wavelength can be inscribed into a single fiber feedthrough to perform distributive sensing measurements. Different sensing parameters, such as temperature, strain, pressure and refractive index can be discriminated with advanced grating sensor designs. There have been lots of efforts in elevate the survival temperature of FBGs. It may involve different technical procedures in changing the chemical composition of fiber glass [59], Nitrogen-doping [60], fiber photosensitization [61], and also permanent damage grating written including type-II grating with ultrafast laser [62] and type-IIA grating with IR laser [63]. Recently, the development of regenerated grating shines new light on the high temperature implementation of conventional type I gratings, which has becoming the industry standard with their low manufacturing costs and excellent sensing performances. By carefully tuning the fiber doping, seeding grating strength, and annealing schedule, relatively strong high-temperature gratings with ~35% reflectivity can be manufactured with well-defined spectral shape, narrow linewidth and low in-line loss [64]. The ultrahigh temperature stability, good grating qualities and relatively simple procedures make the regenerated gratings technique attractive to multiplexible high-temperature sensing applications.

The invention and rapid development of microstructure fiber in the last 15 years revolutionized a wide range of scientific and engineering research fields. The wide flexibilities in the geometry and optical properties of microstructure fibers, provide numerous opportunities in both novel designs and performance enhancements to fiber sensors. Traditional FBG sensor made in solid silica fibers shows good sensitivity in measuring axial strains. But when transverse

84

stress such as directional force or hydrostatic pressure is applied to the fiber, the sensor response is very limited. Moreover, by merely measuring the Bragg wavelength shift, it is difficult to discriminate the temperature influence on the FBG sensor from transverse stress responses. Small cross-sensitivity and high transverse stress resolution cannot be achieved simultaneously [65]. This problem can be overcome by making fiber sensors using side air-holes microstructure fibers [66-69]. When a directional force or hydrostatic pressure is applied to the air-hole fiber, the deformation of air holes transfers the external perturbation into internal stress in the fiber core. The induced internal stresses in x and y transverse directions are different due to the side-hole geometry, and this external stress dependent birefringence can be interrogated through the separation of FBG resonant peaks in x and y polarizations. The transverse stress and pressure response of air-hole microstructure fibers can be numerically simulated with Finite element analysis (FEA) model. New fiber geometries can be designed with optimized size, sharp and positions for fiber core and air-holes, to achieve better transverse stress and pressure response and lower cross-sensitivities [70-71].

Previously, a high temperature pressure sensors inscribed in air-hole microstructure fiber with an ultrafast laser [72] was demonstrated by our research group. The type-II FBG shows stable and reproducible sensing operation over 800°C. But the grating linewidth and strong laser induced birefringence need to be further optimized to allow better pressure sensing range and accuracy. The relatively large in-line loss with the type-II permanent damage also makes sensor multiplexing more difficult.

6.3   REGENERATED GRATING PRESSURE SENSOR

In this section, we apply thermal regeneration technique toair-hole microstructure fiber gratings, and present a multiplexible high-temperature pressure FBG sensor. The regenerated grating is stable at 800°C, and presents ultrasharplinewidth and minimum intrinsic birefringence. Hydrostatic gas pressure from 15 to 2400 psi is interrogated with the regenerated grating at 800°C, and the sensing resolution can reach 15 psi with a 1-pm resolution tunable laser. The temperature and pressure responses can be differentiated with a 2x2 response matrix. Multiplexed regenerated grating sensors in a single fiber can serve as a single device for multipoint and simultaneous measurement of wide ranges of temperature and pressure, which provides a simple and reliable sensing solution in high temperature harsh environment.

Air-hole fibers used in this work have cladding diameter of 220-µm. Two large air holes with 90-µm diameter are placed 20-µm apart in ±x direction. The fiber core is 9.7-µm × 7.5-µm in size and 4.5-µm away from the geometric center of the fiber. The microscopic cross-section image of the fiber is shown in the inlet of Fig. 6.4a, where the fiber core and cladding are illuminated air holes and surrounding. A piece of 20-cm long air-hole fiber was stripped, end-cleaved and fusion spliced at both end with 1550-nm telecom single-mode fiber (Corning SMF-28). The telecom fiber has smaller cladding diameter of 125-µm. In order to seal the air-holes from ambient pressure, multiple re-splices are needed after the initial splice, as shown in fig. 6.4b. The transmission power is monitored during fusion splice to ensure best optical coupling and splicing strength. Less than 1dB loss is achieved with the splice, and the fiber is proved durable under hydrostatic pressure up to 2400 psi.
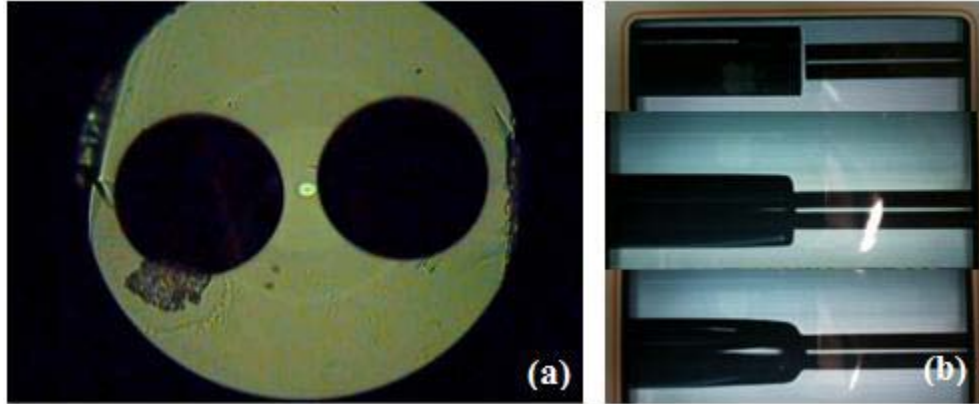
Figure 6.4 Twin-air-hole fiber

(a)the microscope cross-section image of the twin-air-hole fiber with elliptical off-center core; (b) the fusion splice and hole sealing of the large diameter twin-air-hole fiber with Corning SMF-28 fiber.

The spliced fiber was loaded in a hydrogen chamber at 2400-psi and room temperature for 2 weeks before UV writing. 3-cm long seeding FBG with Bragg wavelength at 1545-nm was inscribed into the fiber core with 248-nm KrF Excimer laser and 1070-nm pitch phase mask. Due to the large cladding diameter, rapid escape of loaded hydrogen from the fiber core to the air holes, and UV light diffraction in the air holes, it is difficult to write strong FBGs in the twin-air-hole fiber. Excessive UV exposures were applied in the inscription process to obtain strong AC index contrast, which inevitably induced $>10^{-3}$ DC index change and shifted the grating peaks more than 1.5-nm to longer wavelength during the UV radiation. With ~22500 UV exposures at ~50mJ/cm^2 radiation intensity, relatively strong FBGs can be inscribed into the twin-air-hole fiber. The transmission and reflection spectra of the inscribed FBG are shown in figure 6.5a. The resonant transmission dip is more than 30dB deep, and reflection peak is 15dB high with flat-top spectral shape and >1-nm spectral width. The evolution of seeding FBG during UV writing is shown in figure 6.5b. The reflective peak intensity saturated after 6 minutes of radiation, while the peak wavelength continued shifting to the longer wavelength, and the peak width continued broadening. No blueshift was observed during 15 minutes of UV radiation (~22500 exposures at

87

25Hz laser repitition rate), which confirmed that the grating is still type-I. The over-saturated UV exposure of seeding gratings proved to be critical for the regeneration process in high temperature annealing. No regeneration was observed with 6 minutes of UV radiation (~9000 exposures).
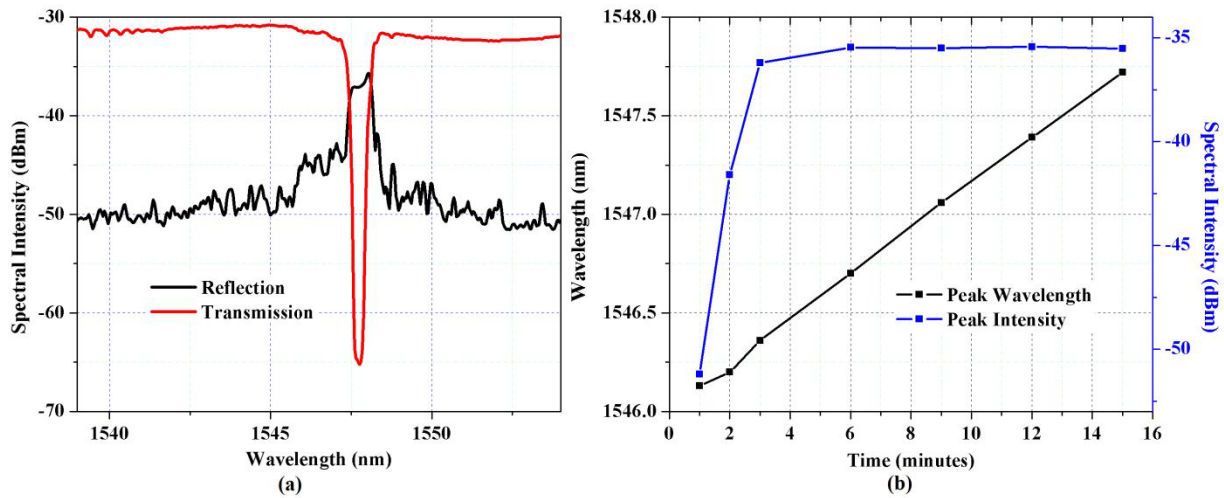
Figure 6.5 Seeding FBG

(a)The transmission and reflection spectra of seeding FBG in twin-hole fiber; (b) The peak wavelength and intensity evolution of seeding FBG during 15 minutes of 25Hz 248-nm UV radiation.

The fiber grating is then put into a stainless steel tube for thermal regeneration and high temperature pressure test. The fiber tube is embedded in a PID controlled furnace that is able to change and maintain temperature from room temperature up to 850°C with ramp rate of 200°C/min. The fiber under test is pressure sealed at both ends with carbon ferrules. The tube can be pressurized with Nitrogen gas tank and pressure regulator. The reflective spectra of the gratings are interrogated with a broadband light source (BBS, MPB EBS-7210, 1520-1610nm) and an optical spectrum analyzer (OSA, Ando 6317B, 20-pm resolution) behind a fiber recirculator. The schematic of the experimental setup is shown in figure 6.6.
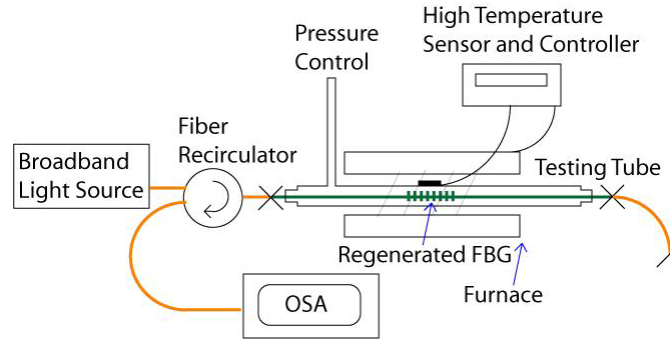
Figure 6.6 Schematic of pressurized furnace

The seeding FBG was annealed at 800°C for regeneration. Maximum ramp rate of 200°C/min was used in the temperature rise. The fiber tube temperature reached the grating erasing point of 700-750°C in 5 minutes, and gradually stabilized to 800°C in 8 minutes. This fast ramp rate annealing recipe is different from previous reports, in which the slow ramp rate and ~1 hour pre-annealing is applied to on single-mode fiber regeneration and benefits the regenerated grating strength [64]. When the slow ramp rate recipe was applied to twin-air-hole fiber grating, no regeneration was observed. We believe this is due to the relatively weaker strength of our seeding grating and lower erasing temperature. The evolution of grating spectra in the annealing process is shown in figure 6.7a. Blue shift in grating wavelength was observed during regeneration, which is different from previous report on conventional single-mode fiber [52-54]. This could be attributed to the gradual relaxation of UV induced DC index in high temperature. The regeneration started before the seeding grating was completely erased. Double peaks were also observed during the process, as is shown with the green curve in figure 6.7a. It is still not clear to us whether this peak separation is due to the co-existence of seeding and regenerating grating, or the thermal enhancement of twin-hole fiber intrinsic birefringence. Figure 6.7b shows the evolution of grating wavelength and strength in a 65 hours regeneration cycle at 800°C. Five distinct regions were identified in the regeneration process. The erase of seeding was followed by the reborn of the grating in the first 4 hours, labeled as region A and B

in figure 3.30. After the regenerated grating reached its maximum strength, the next 15-20 hours is labeled as region C, in which the DC index relaxation and peak blueshifting occurred. Both the grating strength and wavelength was stabilized for 40 hours in region D. In region E, the testing tube and fiber grating were cooled down to room temperature in less than 2 hours. After cooling down, 2.6dB boost in grating strength was observed at 24°C.
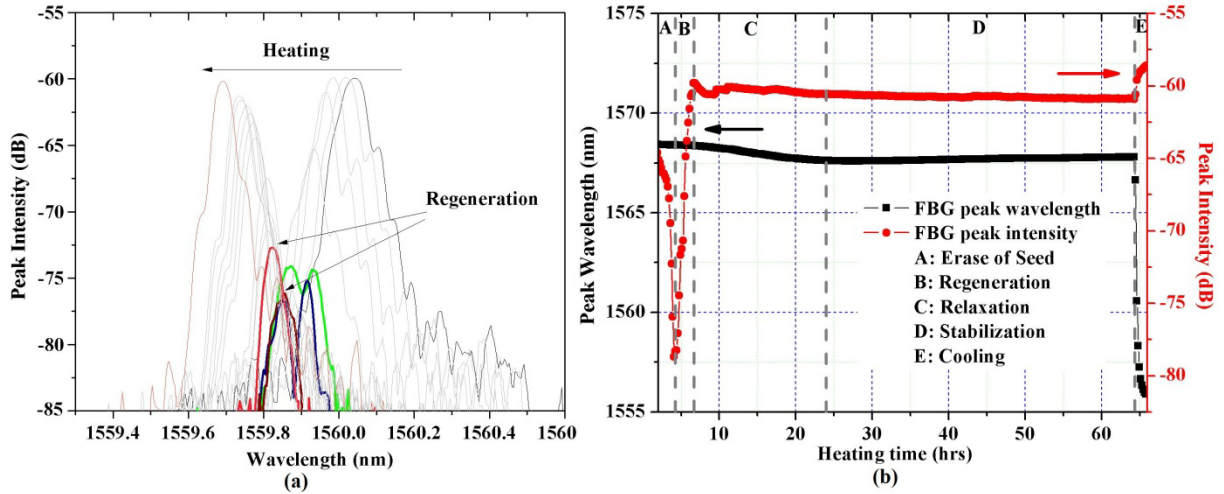
Figure 6.7 Grating regeneration in twin-hole fiber

Evolution of (a) grating reflection spectra, (b) grating strength and resonate wavelength during the regeneration at 800°C.

The temperature and hydrostatic pressure responses of the regenerated grating in twin-hole fiber were tested in the same experimental setup. The detailed results are shown in figure 6.8 and 6.9. Figure 6.8a shows the heating of grating at room pressure of 15-psi. Several heating and cooling cycles were carried out from 24°C to 800°C and no hysteresis was observed. In temperature range from 400-800°C, the FBG peak shifts linearly as a function of temperature at a slope of 0.01518nm/°C, which is consistent with previous results on ultrafast laser written gratings in the same fiber [60]. The slope is slightly smaller for temperature from 24-400°C due to the smaller thermal-optic coefficient of silica at lower temperature. Both spectral shape and strength of the grating were not significantly changed during the heating, as shown in inset of

figure 6.8a. At 800°C the regenerated grating shows a FWHM of <40pm and minimal intrinsic birefringence under room pressure of 15-psi, as shown in figure 6.8b.
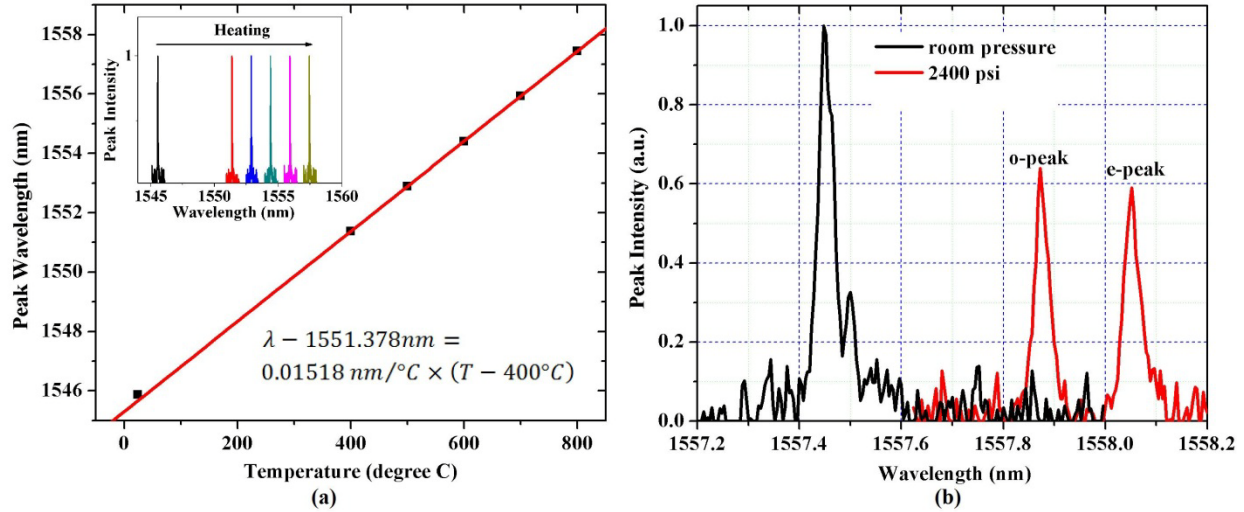
Figure 6.8 Reflective spectra of the regenerated grating under pressure and temperature.

When hydrostatic pressure of 2400-psi was applied, the grating shifted to longer wavelength and split into two distinct peaks 180-pm apart. The separated peaks are attributed to o and e polarizations, which can be confirmed by inserting a polarization beamsplitter before the OSA. This grating peak separation $\lambda_x - \lambda_y$ is generated by the birefringence in applied transverse strain $\varepsilon_x - \varepsilon_y$. And the induced birefringence is given by,

$$\frac{\lambda_x - \lambda_y}{\lambda_0} = \frac{n_{eff}^2}{2}(p_{12} - p_{11})(\varepsilon_x - \varepsilon_y)$$

$$(6.1)$$

Where p_{11} and p_{12} are strain-optic tensor component of the fiber, and n_{eff} is the effective refractive index in the fiber core. Linear dependence of the birefringence upon applied hydrostatic pressure is expected. The slope is expect to vary with ambient temperature due to the temperature dependences of n_{eff}, p_{11} and p_{12}.
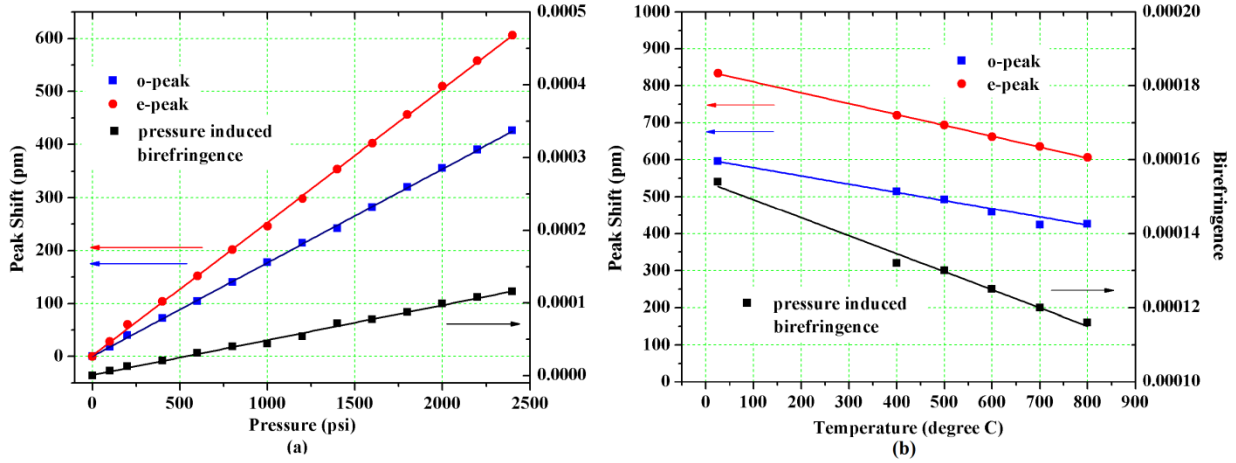
Figure 6.9 Pressure response of the regenerated grating

Fig. 6.9: The regenerated grating wavelength vs. (a) external pressure from 15-psi to 2400-psi at 800°C; (b) temperature from 24°C to 800°C under external pressure of 2400-psi.

The peak separation and induced birefringence are studied under pressure from 15-2400 psi at 800ºC, and at temperature from 24-800ºC under 2400 psi. The results are shown in figure 6.9a and 6.9b respectively. The resonant wavelengths for both polarizations show linear dependences to the external pressure over the entire testing range of pressure. Thanks to the sharp grating linewidth and minimal intrinsic birefringence, the splitting between peaks can be identified as small as 100 psi. The pressure sensitivity of the grating sensor is 13.3-psi per pm at 800ºC, which is also consistent with the results from ultrafast laser written type–II gratings [72]. Under 2400 psi, the pressure response and induced birefringence is 25% smaller at 800 ºC than at 24ºC, which indicates the glass softening and decrease of strain-optic coefficients at high temperature. The temperature and pressure responses of the regenerated grating sensor can be summarized as,

$$\begin{pmatrix} \Delta\lambda_o \\ \Delta\lambda_e \end{pmatrix} = 1.518 \times 10^{-2} \, nm/^\circ C \, \Delta T + \begin{pmatrix} 2.521 \times 10^{-4} \, nm/psi - 9.185 \times 10^{-8} \, nm/^\circ C/psi\Delta T \\ 3.526 \times 10^{-4} \, nm/psi - 1.232 \times 10^{-7} \, nm/^\circ C/psi\Delta T \end{pmatrix} \Delta P$$

$$\Delta\lambda_{o,e} = \lambda - 1551.378nm, \Delta T = T - 400^\circ C, \Delta P = P - 0\,psi$$

(6.2)

Both temperature and pressure can be measured simultaneously according to the response matrix above. With a tunable laser of 1-pm resolution, the temperature resolution is less than 0.1ºC from 400-800 ºC and the pressure resolution is less than 1 atmosphere pressure (15-psi) from 1-160 atmosphere pressure (15-2400 psi).

The maximum pressure used to test the FBG sensor was limited by our N_2 tank pressure. It is believed that air-hole silica fiber has potential to sustain much higher pressure up to 10,000-psi according to our simulation. The tested temperature of 800 ºC is also limited by our homemade pressurized high temperature furnace. By further optimization of the writing of seed grating and annealing schedule, it is possible to push up the survival and operating temperature of the regenerated pressure sensor to higher than 1000 ºC [53]. On the other hand, the fiber geometries can also be further optimized with FEA simulations, to achieve higher pressure sensitivity and lower temperature/pressure cross-sensitivities [70-71]. In comparison with the previous results using type-II FBG [72], better measurement sensitivity and accuracy, better multiplexing capability and the capability of temperature/pressure discrimination are achieved with the type-I regenerated FBGs in twin-hole fiber.

In summary, this section applies the thermal regeneration technique to twin-hole microstructure fibers, and presents high-temperature stable fiber pressure sensor for industry applications. The sensor shows accurate and reliable operation from 24-800ºC for hydrostatic pressure from 15-2400 psi. Compared with interferometer based fiber pressure sensors, the regenerated grating sensor in air-hole microstructured fibers can be multiplexed. A high temperature and pressure sensing network can be formed with large numbers of these sensors on a single fiber feedthrough, and interrogated with a single optical sensing unit.

6.4   DISTRIBUTED HIGH TEMPERATURE PRESSURE SENSING

As has been stated in the previous sections of this chapter, for sensing at high temperature beyond $800^{\circ}C$, fiber sensors are probably the only option due to their excellent thermal resistivity and immunity to electromagnetic noise and corrosion. In the past few years, point sensors such as Fabry-Perot interferometry (FPI) devices have been successfully developed for high temperature applications [56-58]. A more challenging issue is to develop multiplexing technology so the entire power system can be monitored using a single fiber. This is very important given the challenging of wiring tens or hundreds of sensors for extreme environment applications. Quasi-distributed pressure sensing can be realized with fiber Bragg-gratings (FBGs) multiplexed in pressure sensitive fibers. However, FBG based distributed sensing capability is fundamentally limited by the multiplexing density of the FBGs and the consequent high manufacturing cost. Moreover, special grating treatments such as femtosecond laser direct writing and grating regeneration are needed to elevate the survival temperature of FBGs [72-73].

In this section, we reported for the first time truly distributed pressure sensing at room and high temperature using pressure sensitive fibers. It is based on the Optical Frequency Domain Reflectometry (OFDR) measurement of in-fiber Rayleigh scattering. This technology has been applied to provide distributed sensing solution for temperature, axial strain and transverse stress measurements [7, 26, 27, 49]. In this section, air-hole microstructural fibers are used to extend its application for pressure measurement at high temperature. By simultaneously measuring the in-fiber Rayleigh scattering of two orthogonal polarizations, hydrostatic gas pressure applied upon the fiber under test (FUT) are spatially interrogated in sub-centimeter resolution over several meters long of optical fibers. Pressure distributions of up to 13.8-MPa

(2000-psi) are measured in temperature range from 24°C to 800 °C. The technique demonstrated in this letter completely eliminates the use of high-temperature stable FBG sensors and the challenge and cost associated with the manufacturing process.
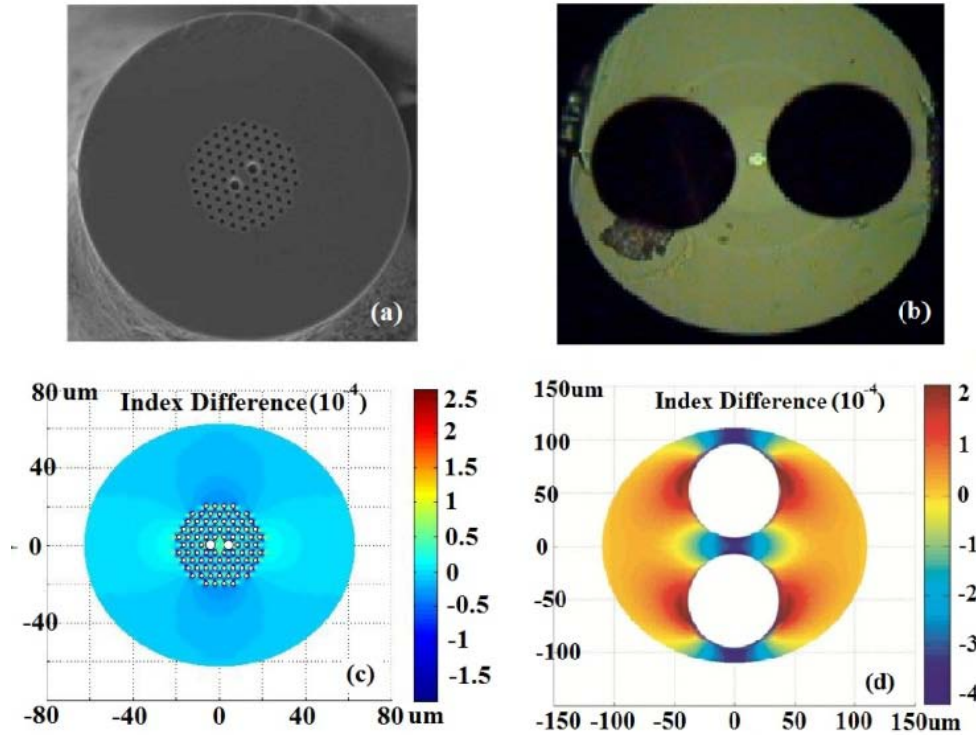
Figure 6.10 Pressure sensitive fibers

The microscope cross-section image of (a) the PM photonic crystal fiber (Fiber A) [9] and (b) the twin-air-hole fiber (Fiber B); FEA (Finite-Element Analysis) simulations on 200-bar pressure-induced birefringence of (c) Fiber A and (d) Fiber B.

Two polarization-maintaining pressure sensitive fibers were investigated in this paper. **Fiber A** is all-silica polarization-maintaining photonic crystal fiber (Blaze Photonics PM-1550-01), with pitch Λ = 4.4-µm, hole diameter d =-2.2 µm and large hole diameter d_1 = 4.5-µm. The cladding diameter of the fiber is 125-µm and the diameter of holey area is ~ 40-µm. The microscopic image of the fiber cross-section is shown in Fig. 6.10a. Due to the anisotropic geometry of the holey structure around the pure-silica core, the fiber birefringence in the core

area is sensitive to transverse stress and external pressure. The pure silica core ensures ultra-low thermal-optic coefficient and ultra-high operating temperature, both of which are ideal for high temperature sensing applications [58]. **Fiber B** is 220-µm diameter side-hole fiber with two 90-µm air holes, as shown in the Fig. 6.10b. The fiber core is 9.7-µm × 7.5-µm in size and 4.5-µm away from the geometric center of the fiber. When external pressure is applied, the large twin-hole structure focuses the induced birefringence into the bridge area, which significantly enhances the pressure sensitivity of **Fiber B** compared with **Fiber A**. **Fiber B** has also proved its long-term stability in temperature as high as 850°C [72-73]. The lower two sub-figures in Fig. 6.10 shows the finite element analysis (FEA, ©ANSYS) simulation of pressure induced birefringence for both fibers under 20-MPa (2900-psi). According to the simulation, the calculated pressure sensitivity of **Fiber B** is ~12.0-µε/MPa (0.083-µε/psi) or ~18.7-pm/MPa (0.129-pm/psi) at 1550-nm, which is ~4-5 times higher than the value for **Fiber A**. Via further optimization of the fiber holey structure, it is possible to further elevate the pressure sensitivity to ~1-pm/psi, so that 1-psi resolution can be achieved with a commercial tunable laser source with 1-pm resolution at 1550nm [7].

Proof-of-concept experiments were first performed at room temperature (24°C) for both fibers using a commercial optical backscatter reflectometer (OBR) from Luna Technologies (OBR 4600). The basic sensing principle of frequency domain in-fiber Rayleigh backscattering has been introduced in chapter 2 of this thesis. Here we briefly revisit it for illumination purposes. A tunable laser source that continuously sweeps from 1520-1610-nm is split before launch into the FUT. The excited Rayleigh scattering and possible discrete reflections in the FUT is reflected back and recombined with the split reference light onto photodiodes with sampling rate of 2MS/s. For each Rayleigh scattering location along the FUT, the path difference between

the two arms results in wavelength difference upon the mixing, and a unique beating signal is generated with location information encoded. After the wavelength-swept measurement, this encoding can be retrieved through fast Fourier transform upon the sweeping time/wavelength [6]. By cross-correlating with a pre-measured reference, Rayleigh spectral shifts induced by external perturbations along the FUT can be spatially interrogated. The spatial resolution is determined by the wavelength sweeping range and the size of cross-correlating window [7]. 1-cm long cross-correlating window is chosen to obtain ~1-pm spectral resolution.
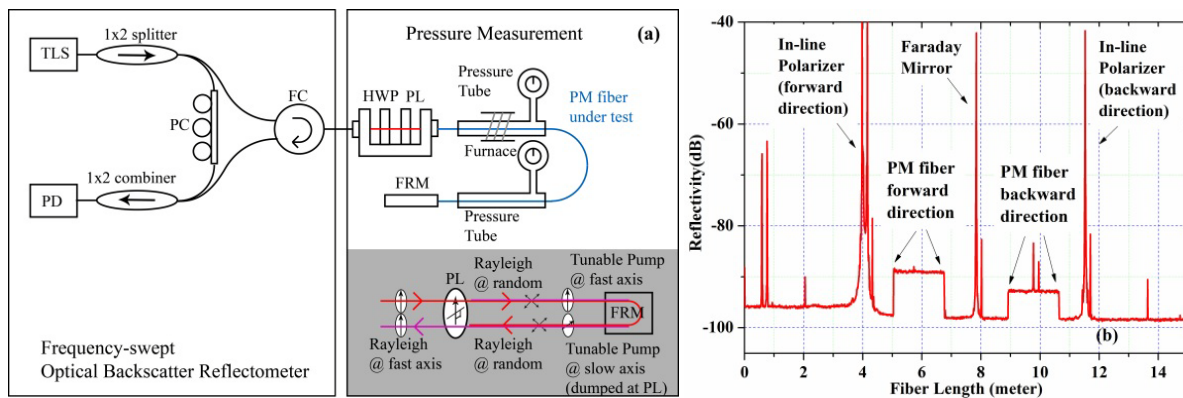
Figure 6.11 Schematic of experimental setup and measured reflectivity along the fiber.

TLS: tunable laser source; PD: photodiode; FC: fiber circulator; HWP: half waveplate; PL: polarizer; FRM: Faraday rotation mirror; PM fiber: polarization-maintaining fiber.

The schematic of experimental setup is shown in Fig. 6.11a. Polarization of the tunable pump signal is aligned with the fast axis of the pressure-sensitive PM fibers using a half waveplate and a linear polarizer. The other end of the PM fiber is fusion spliced with a Faraday Rotation mirror (FRM), so that the polarization of the tunable pump signal in backward propagation is aligned with the slow axis of the PM fiber, and this slow-axis pump light is fully attenuated by the linear polarizer on the way back to the OBR to avoid any interference with the Rayleigh signal. In this configuration, Rayleigh scattering excited by both polarizations along the FUT can be measured within a single scan [9], as is shown in the OBR trace in fig. 6.11b. Birefringence responses at

97

certain PM fiber location can be interrogated by folding the trace along the symmetric axis at the FRM.
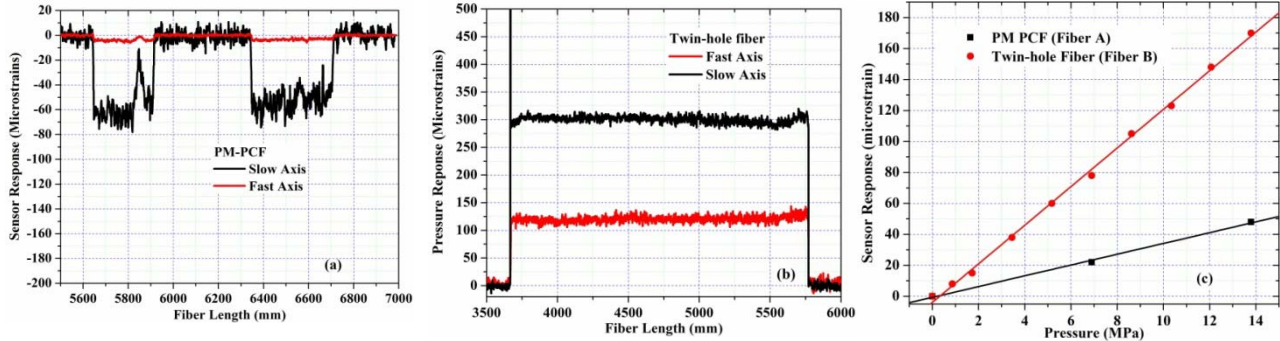
Figure 6.12 Distributed pressure responses at room temperature

13.8-MPa (2000-psi) distributed pressure responses of (a) Fiber A; (b) Fiber B; (c) The induced-birefringence of Fiber A and Fiber B vs. different pressure at room temperature of 24°C.

The room temperature pressure responses of both fibers are measured from 0-13.8-MPa (0-2000-psi) and the results are shown in figure 6.12. Pressure induced birefringence is calculated from the difference between Rayleigh spectral shifts of two orthogonal polarization. Pressure sensitivity of **Fiber A** is 3.48-µε/MPa (0.024-µε/psi) or 5.51-pm/MPa (0.038-pm/psi) at the central sweeping frequency of 1565-nm. And two pressure distribution regions are measured simultaneously, showing the distributed sensing capability. Pressure sensitivity of **Fiber B** is 12.5-µε/MPa (0.086-µε/psi) or 19.6-pm/MPa (0.135-pm/psi) at 1565-nm, which is 3.6 times larger than that of **Fiber A**, and <5% larger than the calculated value. When the spatial resolution of the cross-correlation process is set at 1-cm, the pressure resolution of **Fiber B** is ~7.4-psi. Higher pressure resolution is available for more relaxed special resolution requirements.

The high temperature pressure response of **Fiber B** is investigated within a high temperature furnace. The heating region inside the furnace is approximately 50-cm long. Figure 6.13a shows the spatial resolved Rayleigh spectral shifts for both fast and slow axis polarizations and the derived birefringence at 800°C. It is observed that the pressure induced birefringence is immune

98

to the temperature induced fluctuations in the fast and slow axis. Figure 6.13b shows the Rayleigh spectral response of slow axis, fast axis and the birefringence vs. different pressure from 0-13.8-MPa at 800°C. Good linearity of pressure dependence was observed.
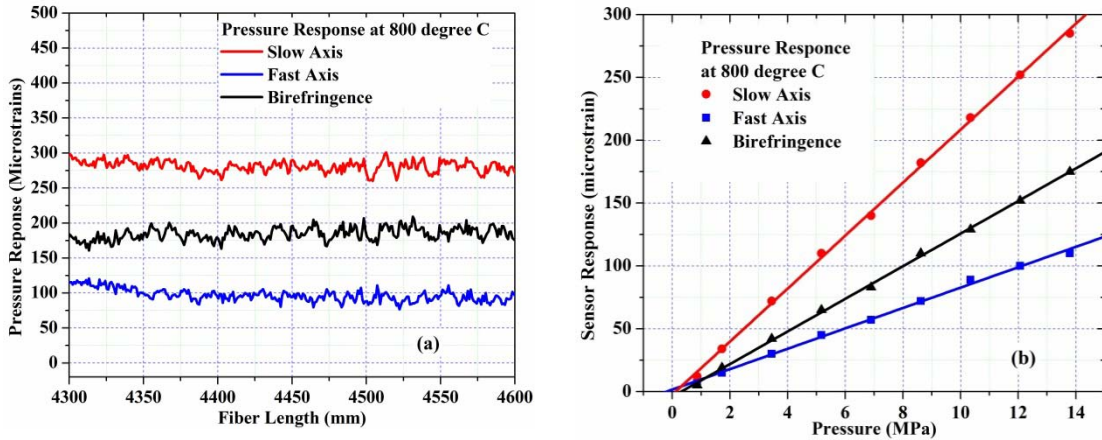
Figure 6.13 Distributed pressure response at high temperature

 (a) 13.8-MPa (2000-psi) distributed response of twin-hole fiber (Fiber B) at 800°C; (b) The Rayleigh sensor responses vs. different pressure at 800°C.

In summary, we present in this section a true distributed fiber optic sensing technique for high temperature pressure measurement. Polarization resolved Rayleigh scattering signals are interrogated along several meters long pressure-sensitive PM fibers to obtain sub-centimeter sensing resolution for pressure up to 13.8-MPa (2000-psi) and temperature as high as 800°C. The simplicity, low cost and high fidelity of this technique make it a unique solution to high temperature sensing applications.

7.0   CONCLUTION AND FUTURE WORK

In this Ph.D. dissertation, I exploited a variety of fiber optic sensing technologies including on-fiber optical heating, high temperature grating regeneration, in-fiber Rayleigh scattering and in-fiber single-beam Coherent Anti-Stoke Raman Spectroscopy, and developed a series of fiber optic sensors for different sensing applications in extreme environments. Multiplexible and distributed hydrogen gas sensors were developed for room and low temperature operations (Chapter 3). Discrete and continuous liquid level sensors were developed for cryogenic fluid testing (Chapter 4). Gas flow sensor was developed for full characterization of comprehensive flow velocity vectors (Chapter 5). Multiplexible point sensors and distributed sensors were developed for high temperature pressure sensing. And finally, preliminary results on in-fiber single-beam CARS were presented for gas trace detection.

There are still a lot to be done to further improve the sensitivity, response time, functionality and lifetime of the different sensors reported here. For example, to operate the self-heated hydrogen sensor at liquid hydrogen temperature (20.2K), both the self-heating efficiency of the fiber and the Pd-hydrogen response needs to be greatly enhanced. Possible approach includes using D-shaped attenuation fiber chemically etched down to the fiber core and precise control over the thickness of Pd coating plus possible assistance from surface plasma resonance effects.

For liquid level sensors, preliminary results of level sensing of liquid helium at 4K were demonstrated in chapter 4. But the sensing range is limited to ~ ten centimeter due to the strong absorption of attenuation fiber and the exponential decay of light signal along the active fiber. New types of fibers with gradually changing attenuated doping can be developed to provide a moderate and uniform heating profile, so that meters range level sensing are feasible for extreme low temperatures. The hot wire fiber grid flow sensors could also benefit from new attenuation fibers with customized attenuation. A more uniform heating profile of the optically heated fiber ensures wide dynamic range for the flow sensing. The current electrical heating can be completely replaced by optical heating, so that the full advantages of all-fiber optic sensing could be exploited.

In Chapter 6 of this thesis, regenerated gratings were reported in pressure sensitive fibers to measure temperature and pressure at 800°C. With further optimization of the fabrication and regeneration process, it is possible to elevate the operating temperature of the fiber pressure sensor to more than 1000°C. For even higher temperature, all silica fiber and sapphire fiber are preferred due to the high temperature diffusion of the doping ions in conventional silica fiber. However, grating inscription in all-silica and non-silica fibers turn out to be expensive and unreliable. For type IIA damage gratings written with ultrafast laser pulses, there are still a lot to be accomplished before the stage of large-scale and low-cost commercial manufacturing. Another very promising approach would be in-fiber scattering sensing, as is shown in the second part of chapter 6. Both Rayleigh scattering in frequency domain and Brillouin scattering in time domain have been employed in extreme environmental sensing applications. Using the op5tical fiber itself as the sensing element, these scattering based technology avoid the costly and fragile fabrication of in-fiber sensing structures, and allow true distributed sensing anywhere along the

fiber. Further optimization of the microstructure sensing fiber to enhance the sensitivity, and further development of the scattering interrogation unit to lower the cost and speed up the measurement time, would eventually make these in-fiber sensing technologies feasible for industry and consumer sensing applications.

In the appendix A, preliminary results on single-beam CARS were reported for in-fiber sensing of propane gas. By using spatial filtering technique, we were able to filter out the strong silica signal, but the anti-stoke efficiency is still relatively low considering the ultralong interacting length in the hollow core fiber. To fully utilize the fiber length and get ppm concentration sensitivity, both flat dispersive fibers and more powerful dispersion compensation is needed. Also the fully discriminate the resonant anti-stoke signal from the non-resonant broadband signal, polarization maintaining hollow core fiber is needed for polarization resolved CARS measurements.

APPENDIX A

IN-FIBER SINGLE-BEAM CARS FOR GAS SENSING

Coherent Anti-Stoke Raman Scattering (CARS) spectroscopy is a powerful tool to detect and image vibrational modes of gas, liquid and solid objects of interest with great sensitivity and accuracy. CARS is a four-wave-mixing process, which requires precise phase matching between involved beams. Traditionally, efficient generation of the anti-Stoke signal involves comprehensive alignment of the pump, Stoke and probe beams to ensure the spatial and temperal overlap between different light components. The invention and development of ultrabroadband femtosecond laser source in the last 10 years provide a new solution to CARS measurements. The ultra-broad bandwidth provides pump, Stoke and probe simultaneously for possible detection of multi-modal vibrational modes. The ultrashort pulse duration of the beam automatically ensures temporal overlap between pump, Stoke and probes. Single-beam CARS in free space and bulk gas cells have been reported recently [74-76] using broadband laser and pulse shaping techniques.

To accurately measure and retrieve Raman signature from a broadband multi-species CARS measurement, it is critically important to precisely control temporal and spectral shape and phase of the ultrafast laser pulse. As was described in previous chapters, it is possible to introduce an artificial notch in the broadband laser spectrum. By comparing the notches in the

resulted anti-stoke spectrum at shorter wavelength, vibration frequencies from different test species can be identified.

In this section, we introduced our preliminary results on in-fiber single beam CARS measurements for gas sensing. Hollow-core photonic crystal fiber (HCPCF) is chosen as the gas cell due to the ultralong interaction length, small cross-section for Raman measurement and the support for single-mode operation of broadband lights. Raman and stimulated Raman spectroscopy of different gas species have been reported in HCPCF for the last ten years [77-79]. Due to its all-silica nature and ultrastable thermal properties, HCPCF is also an ideal sensing elements for high temperature sensing applications. To the best of our knowledge, no CARS measurement has been performed in HCPCF. Combining the single-beam CARS technique with HCPCF gas cell, we are expecting significant enhancement of CARS efficiency to detect ppm level gas concentration in hostile environments.

The experimental setup for single-beam in-fiber CARS measurement is shown in figure A1.1a. A mode-locked Ti:Sapphire laser oscillator is constructed to provide 13fs laser pulse in 740-820nm wavelength. The pulse is sent into a pulse shaper, which consists of two pairs of identical diffractive gratings, two pairs of concave mirrors, and two 128-pixel liquid-crystal phase masks, in 4-f configurations as shown in Figure A1.1b. The first diffractive grating and concave mirror disperse the broadband spectrum evenly onto the phase masks. The liquid-crystal phase mask array is essentially an array of independently controllable retarders. By align the crystal axis of first phase mask 45° to the polarization of incident light and combining with a linear polarizer, the first phase mask work as an intensity modulator able to individually changing the intensity of different spectral components. The crystal axis of the 2nd phase mask is aligned to the polarization of the incident light, and the phase mask array served as a phase
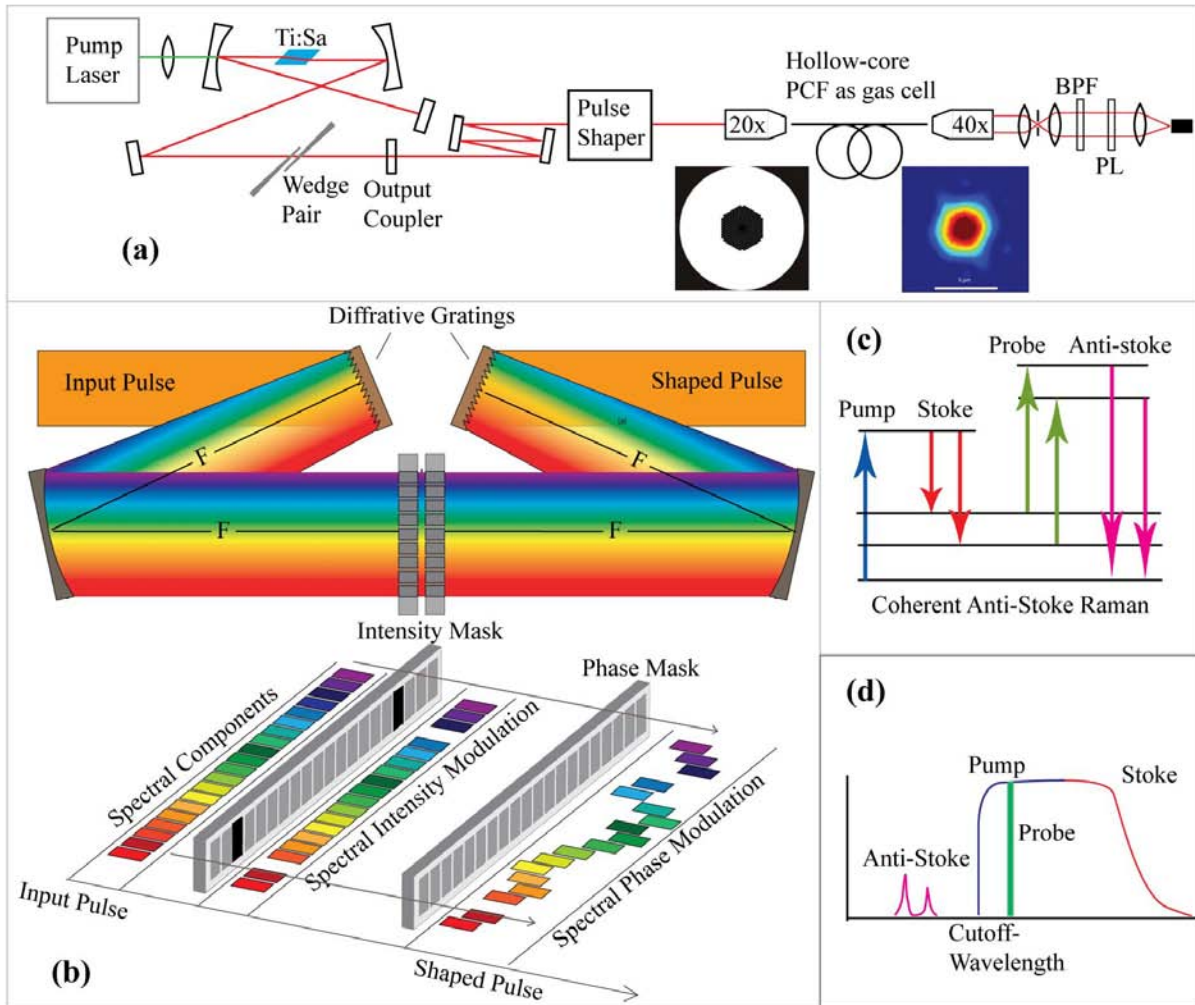
Figure 7.1 Schematic of in-fiber single-beam CARS

(a) In-fiber single-beam CARS setup consists of ultrafast oscillator, pulse shaper, hollow core photonic crystal fiber gas cell, and spatial filtering anti-stoke light collections; (b) The pulse shaper consists two 128-bit liquid crystal phase mask (intensity and phase) at the Fourier plane of a 4-f pulse shaping configuration; (c) Four-wave-mixing energy diagram of multi-modal CARS using broadband light; (d) Pump beam is notched out of the broadband spectrum with phase and polarization shifts.

modulator able to individually change the spectral phase of different spectral components. The light is then dispersed again in the 2nd concave mirror and diffractive gratings, converted back to collimation for CARS measurements. The light is then focused into the HC-PCF using a 20x objective with 80% coupling efficiency. The generated anti-stock signal is collected at the other end of the HC-PCF using another 20x objective. The HC-PCF is pressure sealed at both end with gas chambers and optical windows. A short pass filter is inserted behind the collecting objective to block the original broadband spectrum and pass the anti-stoke components at shorter wavelength. A spatial filter is inserted at the first imaging plane to block the silica Raman signal from the supporting structure of the HC-PCF [79]. A secondary imaging system collected the short-passed and spatially filtered anti-Stoke signal with CCD camera and spectrometer.
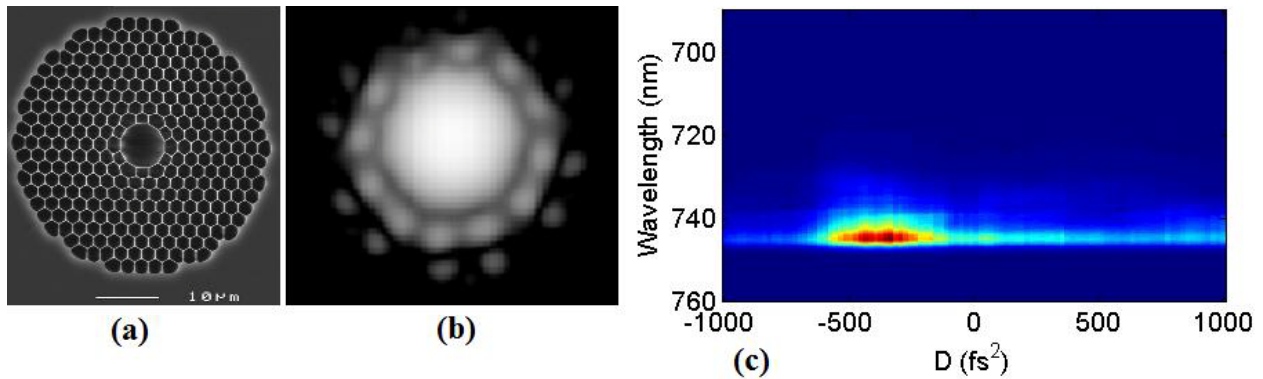
Figure 7.2 Fiber gas cell and dispersion compensation.

(a) cross-section image and (b) 800-nm output mode profile the hollow core photonic crystal fiber [80]; (c) Anti-stoke spectra vs. different linearly chirped single-beam pulse.

Cross-section image and the 800-nm output mode profile of the HC-PCF (Blaze Photonics, HC-800-02) used in our experiments are shown in Figure A1.2a and A1.2b. The fiber has a core diameter of 6.8-µm, mode-field diameter of 5.0-µm at 840nm wavelength. The 2nd order dispersion of the fiber is 0-ps/nm/km at 825nm with a dispersion slope of 15.3-pm/nm^2/km. The fiber dispersion and the material dispersion from previous bulk material from the laser oscillator and the focusing optics need to be compensated using the pulse shaper. Figure A1.2c

shows the intensity of anti-stoke signal vs. different dispersion compensation provided by the pulse shaper. The anti-stoke signal is at its maximum for dispersion compensation of 400-500-fs^2. Because the pulse chirping is accumulated along the HC-PCF, the pulse shaper is only able to compensate pulse chirping in a certain range of HC-PCF. After that, the broadband pulse will be heavily chirped and out of phase for CARS process. To fully utilize the ultralong interaction length of the fiber for enhanced CARS sensitivity, new HC-PCF with flat zero dispersion is needed.

Figure A1.3 shows the Raman spectrum of propane (C_3H_8) gas and fiber silica measured in the HC-PCF with a 800nm CW light from the non-mode-locked Ti:Sapphire laser oscillator. Sharp propane Raman line at 870-cm^{-1} and 1060-cm^{-1} can be identified from the broadband silica Raman background. With a proper spatial filter, the silica Raman background can be greatly eliminated [79].
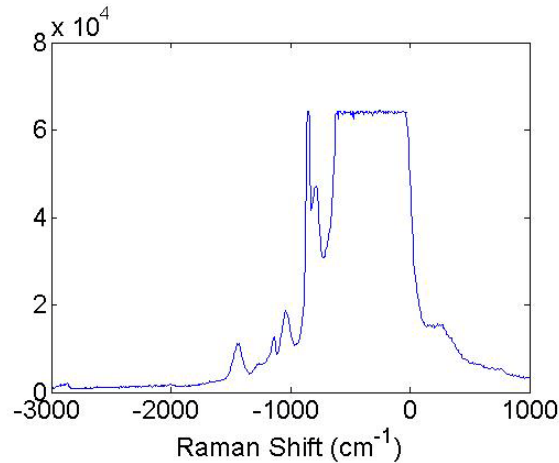
Figure 7.3 Raman spectrum of propane gas and silica measured in HC-PCF.

With a mode-locked ultrabroadband spectrum from 760-840nm, we provide small amount of dispersion compensation and phase notched the probe beam to measure the anti-stoke signal of propane in 700-760nm wavelength. Figure A1.4 shows the results with a sweeping phase notch with and without spatial filtering of silica signal.
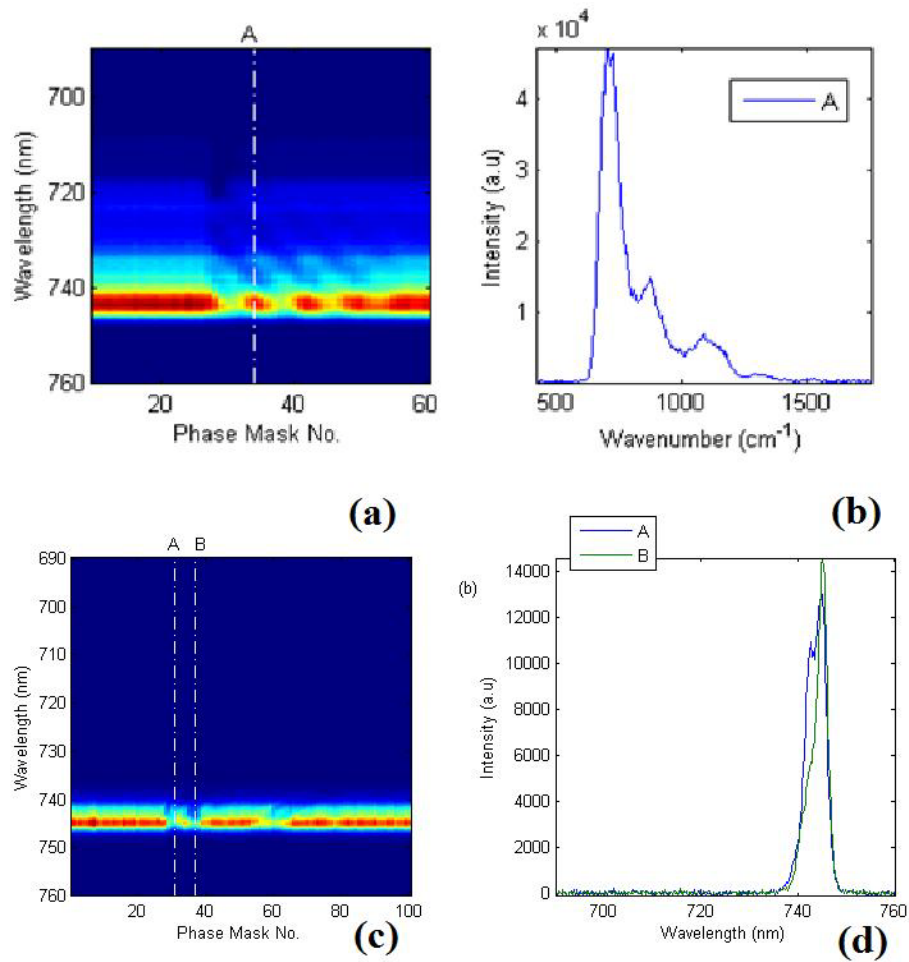
Figure 7.4 Anti-stoke Raman spectra of propane (a, b) with silica (c, d) without silica.

As have been discussed in chapter 2, a sharp phase notch on the broadband spectrum generated a picoseconds pump signal, which is separated from the femtosecond pump and stoke signal with a phase delay. The interference between the femtosecond broadband and picoseconds sharp pulse generated a corresponding notch in the broadband non-resonant, which combined with the notch position in the broadband spectrum, provides information of the Raman shift. With a phase notch sweeping from shorter to longer wavelength, a corresponding sweeping notch will be observed in the anti-stoke spectrum for each Raman line, as is confirmed Figure A1.4a for the silica Raman signal. Linearly tilted dips can be identified for silica Raman lines in the anti-stoke wavelength vs. probe notch wavelength plots. With a spatial filter to block the strong silica signal, linearly tilted dips can also be roughly identified for propane Raman lines at 870-cm^{-1} and 1060-cm^{-1}, as shown in Figure A1.4c. The phase mask starts from 720nm with resolution of 1.3nm/pixel. Raman shift are obtained from the difference between probe notch wavelength and anti-stoke notch wavelengths.
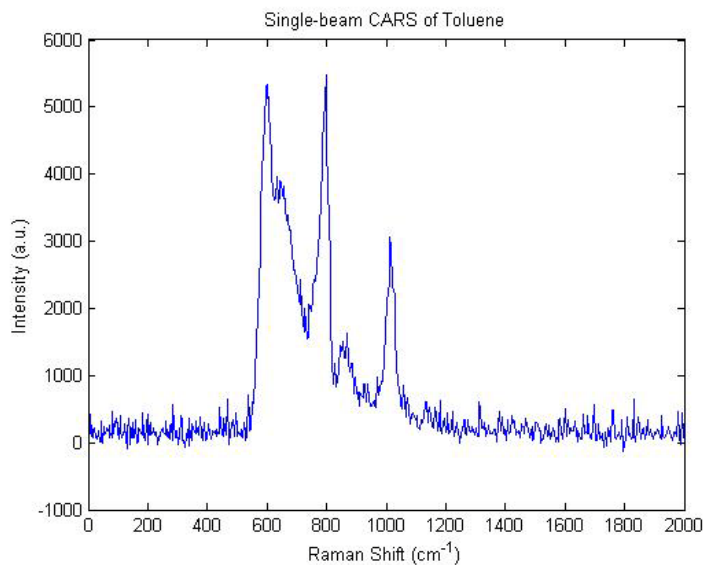
Figure 7.5 Free-space CARS of toluene liquid using polarization and phase shaping.

To further enhance the resonant anti-stoke signal, we can use the intensity modulator to rotate the polarization of the notched probe by 90° so that the four-wave-mixing occurs in xx-yy polarization configuration for the pump, Stoke, probe and anti-Stokes [74-76]. By inserting a linear polarizer in y direction before the receiving end, we can completely filter out any non-resonant anti-Stoke signals that is not generated by the y-polarized probe signal. Figure A1.5 shows our results in free-space on Toluene ($C_6H_5CH_3$) liquid. Sharp anti-stoke peaks instead of dips can be indentified for different Toluene Raman lines. Employment of this polarization and phase shaped scheme has not been successful due to the unpolarized nature of our HC-PCF. Currently we are in the process of seeking polarization-maintaining HC-PCF to fulfill the requirements and carry out the polarization resolved measurements.

APPENDIX B

PUBLICATIONS

B.1   PEER-REVIEWED JOUNAL PUBLICATIONS

1.   T. Chen, et al., "Distributed liquid level sensors using self-heated optical fibers for cryogenic liquid management", in preparation.

2.   T. Chen, et al., "Distributed flow sensing using optical hot wire grid," Accepted for publication on Optics Express, 2012.

3.   T. Chen, et al., "Distributed hydrogen sensing using in-fiber Rayleigh scattering," Accepted for publication on Applied Physics Letters, 2012.

4.   T. Chen, et al., "Distributed high-temperature pressure sensing using air-hole microstructure fibers," Optics Letters, 37, 1064-1066 (2012).

5.   T. Chen, et al., "Tapered fiber Mach-Zehnder interferometer for simultaneous measurement of liquid level and temperature", Electronics Letters, 47, 1093-1094 (2011).

6.   T. Chen, et al., "Regenerated fiber Bragg grating sensors for high temperature pressure sensing", Optics Letters, 36, 3542-3544 (2011).

7.   T. Chen, et al., "Self-heated optical fiber sensor array for cryogenic fluid level sensing", IEEE Sensors Journal, 11, 1051, (2011).

8.   T. Chen, et al., "Self-heated all-fiber sensing system for cryogenic environments", Meas. Sci. and Technol., 21, 094036, (2010).

9.   C. Jewart, T. Chen, et al., "Bending Insensitivity of fiber Bragg grating in suspended core fiber", Optics Letters, 36, 4491-4493 (2011).

10.   Q. Wang, T. Chen, et al., "All-fiber Passively Mode-locked Thulium-doped Fiber Ring Oscillator operated at solitary and noise-like modes," Optics Letters, 36, 3750-3752 (2011).

11.   C. Jewart, T. Chen, et al., "Suspended core fiber Bragg grating sensor for directional dependent transverse stress monitoring", Optics Letters, 36, 2360-2362 (2011).

12.   F. Yei, T. Chen, et al., "Cryogenic fluild level sensor multiplexed by frequency-shifted interferometry", Applied Optics, 49, 4898, (2010).

13.   M. Buric*, T. Chen*(* Co-first author, equal contribution), et al., "Multiplexible low-temperature fiber Bragg grating hydrogen sensors", IEEE Photonics Technology Letters, 21, 1594-1596 (2009).

B.2   CONFERENCE PROCEEDINGS

1.   T. Chen, et al., "Distributed sensing using self-heated fiber", accepted for CLEO 2012, San Jose, CA.

2.   T. Chen, et al., "Waveguide Saturable Absorbers in Chalcognide Glass Fabricated by Ultrafast Lasers", CLEO 2011, Baltimore.

3.   T. Chen, et al., "Regenerated fiber Bragg-gratings in air-hole microstructure fibers for high-temperature pressure sensing", SPIE DSS 2011, invited talk, Orlando.

4.   T. Chen, et al., "Self-heated all-fiber sensing system for cryogenic environments", SPIE DSS 2010, invited talk, Orlando.

5.   T. Chen, et al., "Active fiber hydrogen sensors for low-temperature operation", CLEO 2009, Baltimore.

6.   C. Jewart, T. Chen, et al., "Fiber Bragg grating transverse load sensors using suspended core fibers for directional dependent strain measurement", Optical Fiber Sensors, Ottawa, Canada, 2011.

7.   K. P. Chen, B. McMillen, Q. Wang, B. Zhang, T. Chen, et al., "Influence of Pulse Width in Ultrafast Laser Fabrication of Embedded Waveguides in Chalcogenide Glasses", CLEO 2011, Baltimore.

8.   D. Xu, T. Chen, et al., "Laser-assisted chemical vapor deposition of siliton nano-layers in air-hole microstructure fibers," CLEO 2010, San Jose.

9.   Q. Wang, T. Chen, et al., "Mode-locked ultrafast Thulium fiber laser with all-fiber dispersion compensation," CLEO 2010, San Jose.

10.	D. Xu, T. Chen, et al., "Silicon long period grating grown in hollow fiber by laser-assisted chemical vaper deposition," SPIE Europe 2010, Brussels.

11.	K.P. Chen, T. Chen, et al., "All-fiber low-temperature hydrogen sensing using a multifunctional light source", OFS20 2009, Edinburg.

## B.3	BOOK CHAPTERS

T. Chen, M.P. Buric and K.P. Chen, Self-heating fiber bragg grating sensor, Trends in Photoincs, Transworld Research Network, 2010: 169-208.

BIBLIOGRAPHY

1. K.O. Hill, Y. Fujii, D. C. Johnson, B.S. Kawasaki, "Photosensitivity in optical waveguides: Application to reflection filter fabrication", Appl. Phys. Lett. 32 (10) (1978) 647.

2. G. Meltz, W.W. Morey, W.H. Glenn, "Formation of Bragg gratings in optical fibres by transverse holographic method", Opt. Lett. 14 (15) (1989) 823.

3. P.J. Lemarie, A.M. Vengsarkar, W.A. Reed, and V. Mizarhi, "Refractive index changes in optical fibers sensitized with molecular hydrogen", in Technical Digest of Conf. on Opt. Fiber commun., OFC '94, pp. 47-48, 1994.

4. http://www.eaeeie.org/theiere_bratislava/5-1.html

5. B.J. Soller, M. Wolfe and M.E. Froggatt, "Polarization resolved measurement of Rayleigh backscatter in fiber-optic components", OFC Technical Digest 2005, paper NWD3.

6. S. T. Kreger, D. K. Gifford, M. E. Froggatt, B. J. Soller, M. S. Wolfe, "High resolution distributed strain or temperature measurements in single- and multi-mode fiber using swept-wavelength interferometry", Optical Fiber Sensors, ThE42 (2006).

7. A. K. Sang, M. E. Froggatt, D. K. Gifford, S. T. Kreger, and B. D. Dickerson, "One centimeter spatial resolution temperature measurements in a nuclear reactor using Rayleigh scatter in optical fiber," IEEE Sensor J. 8, 1375-1380 (2008).

8. Katz, J. M. Levitt, E. Grinvald, and Y. Silberberg, "Single-beam coherent Raman spectroscopy and microscopy via spectral notch shaping," Opt. Express 18, 22693-22701 (2010)

9. S. G. Chalk, J. F. Miller, "Key challenges and recent progress in batteries, fuel cells, and hydrogen storage for clean energy systems," Journal of Power Sources, vol. 159, pp. 73-80, (2006).

10. B. Sutapun, M. Tabib-Azar, A. Kazemi, "Pd-coated elastooptic fiber optic Bragg grating sensors for multiplexed hydrogen sensing," Sens. Act., vol. B 60, pp. 27–34, (1999).

11. A. Trouillet, E. Marin, C. Veillas, "Fibre gratings for hydrogen sensing," Measurement Science & Technol., vol. 17(5), pp. 1124-1128, (2006).

12. Rogers, J.A., Eggleton, B.J., Pedrazzani, J. and Strasser T., "Distributed on-fiber thin film heaters for Bragg gratings with adjustable chirp," Appl. Phys. Lett. 74, 3131, (1999).

13. M. P. Buric, K.P. Chen, M. Bhatterai, P. Swinehart, and M. Maklad, "Active Fiber Bragg Grating Hydrogen Sensors for All-Temperature Operation", IEEE Photonic Technology Letters, vol. 19, no. 5, March, (2007).

14. Limberger, H.G. Ky, N.H., Costantini, D.M., Salathe, R.P., Muller, C.A.P and Fox G.R., "Efficient miniature fiber-optic tunable filter based on intracore Bragg grating and electrically resistive coating," IEEE Photonics Technol. Lett. 10, 361, (1998).

15. X. Bevenot, A. Trouillet, C. Veillas, H. Gagaire, and M. Clement, "Hydrogen leak detection system using an optical fibre sensor for aerospace applications," Sensors and Actuators B, vol. 67, 1-3, pp. 57-67, (2000).

16. B. McMillen, C. Jewart, M. Buric, W. Xu, Y. Lin, and K. P. Chen, "Fiber Bragg grating vacuum sensor" Appl. Phys. Lett., vol.87, pp. 234101, (2005).

17. C. Jewart, B. McMillen, S. K. Cho, and K. P. Chen, "X-Probe flow sensor implemented through the use of active fiber-Bragg gratings", Sensor and Actuator A, vol. 127, pp. 63-68, (2006).

18. K. P. Chen, B. Mcmillen, M. Buric, C. Jewart, and W. Xu, "Self-heated Bragg grating sensors," Applied Physics Letters, 86, 143502, (2005).

19. D. Coric, R. Chatton, Y. Luchessa, H.G. Limberger and R.P. Salathe, "Light-controlled Reconfigurable Fiber Bragg Gratings Written in Attenuation Fiber," Optical Fiber Communication and the National Fiber Optic Engineers Conference, 2007. OFC/NFOEC 2007. Conference on, 25-29 March 2007.

20. K. S. Park, Y. H. Kim, J. B. Eom, S. J. Park, M-S. Park, J-H. Jang, and B. H. Lee, Optics Express, 19, 18190-18198 (2011).

21. C. Caucheteur, M. Debliquy, D. Lahem, and P. Megret, Optics Express, 16, 16854-16859 (2008).

22. M. Buric, T. Chen, M. Maklad, P. R. Swinehart, and K. P. Chen, IEEE Photonic Technology Letters, 21, 1594-1596, (2009).

23. T. Chen, D. Xu, M. Buric, M. Maklad, P. R. Swinehart, and K. P. Chen, Measurement Science & Technology, 21, 094036-094043 (2010).

24. S. Sumida, S. Okazaki, S. Asakura, H. Nakagawa, H. Murayama, and T. Hasegawa, Sensors & Actuators B, 108, 508-514 (2005).

25. D. Y. Wang, Y. Wang, J. Gong, and A. Wang, IEEE Photonic Technology Letters, 23, 733-735 (2011).

26. S. T. Kreger, D. K. Gifford, M. E. Froggatt, B. J. Soller, and M.S. Wolfe, "High resolution distributed strain or temperature measurements in single- and multimode fiber using swept-wavelengh interferometry," Optical Fiber Sensors, ThE42 (2006).

27. R. R. J. Maier, W. N. MacPherson, J. S. Barton, S. McCulloch, and B. J. S. Jones, "Distributed sensing using Rayleigh scatter in polarization-maintaining fibres for transverse load sensing," Meas. Sci. Technol., 21, 094019 (2010).

28. T. Guo, Q. Zhao, Q. Dou, H. Zhang, L. Xue, G. Huang, and X. Dong, "Temperature-insensitive fiber Bragg grating liquid-level sensors based on bending cantilever beam," IEEE Photonics Technology Letters, 17, 2400-2402, (2005).

29. T. Chen, M. Maklad, P. R. Swinehart, and K. P. Chen, "Self-heated optical fiber sensor array for cryogenic fluid level sensing", IEEE Sensors Jounal, 11, 1051-1052 (2011).

30. S. Khaliq, S. W. James, and R. P. Tatam, "Fiber-optic liquid-level sensor using a long-period grating", Optics Letters, 26, 1224–1226 (2007).

31. B. Yun, N. Chen, and Y. Cui, "Highly sensitive liquid-level sensor based on etched fiber Bragg grating," IEEE Photonics Technology Letters, 19, 1747-1749 (2007).

32. Z. Tian, S. Yam, J. Barnes, W. Bock, P. Greig, J. M. Fraser, H. Loock, and R. D. Oleschuk, "Refractive index sensing with Mach-Zehnder interferometer based on concatenating two single-mode fiber tapers", IEEE Photonics Technology Letters, 21, 161-163 (2009).

33. Y. Li, E. Harris, L. Chen, and X. Bao, "Application of spectrum differential integration method in an in-line fiber Mach-Zehnder refractive index sensor", Optics Express, 18, 8136-8143 (2010).

34. P. Lu, L. Men, K. Sooley and Q. Chen, "Tapered fiber Mach-Zehnder interferometer for simultaneous measurement of refractive index and temperature," Applied Physics Letters, 94, 131110 (2009).

35. S. M. Chandani, N. A. F. Jaeger, "Optical Fiber-based liquid level sensor", Optical Engineering 46(11), 114401, (2007).

36. K. Romo-Medrano and S. N. Khotiaintsev, "An optical-fibre refractometric liquid-level sensor for liquid nitrogen", Meas. Sci. Technol. 17 998, (2006).

37. Ye, F., Qian, L., Liu, Y., Qi, B., "Using Frequency-Shifted Interferometry for Multiplexing a Fiber Bragg Grating Array", IEEE Photonics Technology Letters, Vol 20, 1488, (2008).

38. F. Yei, T. Chen, D. Xu, K.P. Chen and L. Qian, Cryogenic fluild level sensor multiplexed by frequency-shifted interferometry, Applied Optics, 2010.

39.   H. H. Bruun, Hot-Wire Anemometry: Principles and Signal Analysis (Oxford University Press, 1995) Chap. 2.

40.   Y-H. Wang, C-P. Chen, C-M. Chang, C-P. Lin, C-H. Lin, L-M. Fu, and C-Y. Lee, "MEMS-based flow sensors," Microfluid Nanofluid, 6, 333-346 (2009)

41.   G. D. Byrne, S. W. James, and R. P. Tatam, "A Bragg grating based fibre optic reference beam laser Doppler anemometer," Meas. Sci. Technol. 12(7), 909-913 (2001)

42.   Frazão, P. Caldas, F. M. Araújo, L. A. Ferreira, and J. L. Santos, "Optical flowmeter using a modal interferometer based on a single nonadiabatic fiber taper," Opt. Lett. 32, 1974-1976 (2007)

43.   L. J. Cashdollar and K. P. Chen, "Fiber Bragg grating flow sensors powered by in-fiber light," IEEE Sensors J., 5, 1327-1331 (2005).

44.   P. Caldas, P. A. S. Jorge, G. Rego, O. Frazao, J. L. Santos, L. A. Ferreira, and F. Araujo, "Fiber optic hot-wire flowmeter based on metallic coated hybrid long period grating/fiber Bragg grating structure," Appl. Opt. 50(17), 2738-2743 (2011)

45.   S. Gao, A. P. Zhang, H. Tam, L. H. Cho, and C. Lu, "All-optical fiber anemometer based on laser heated fiber Bragg gratings," Opt. Express, 19, 10124-10130 (2011).

46.   W. Eickhoff, and R. Ulrich, "Optical frequency domain reflectometry in single-mode fiber," Appl. Phys. Lett., 39, 693-695 (1981).

47.   U. Glombitza, and E. Brinkmeyer, "Coherent frequency-domain reflectometry for characterization of single-mode integrated-optical waveguides," J. Lightwave Technol., 11 (8), 1377-1384 (1993).

48.   B. Soller, D. Gifford, M. Wolfe, and M. Froggatt, "High resolution optical frequency domain reflectometry for characterization of components and assemblies," Opt. Express 13, 666-674 (2005).

49.   M. Froggatt, and J. Moore, "High-spatial-resolution distributed strain measurement in optical fiber with Rayleigh scatter," Appl. Opt., 37 (10), 1735-1740 (1998).

50.   T. Chen, Q. Wang, R. Chen, B. Zhang, C. Jewart, K. P. Chen, M. Maklad and P. R. Swinehart, "Distributed high temperature pressure sensing using air-hole microstructural fibers," Opt. Lett., 37, 1064-1066 (2012).

51.   B. W. Zhang and M. Kahrizi, "High-temperature resistance fiber Bragg grating temperature sensor fabrication," Ieee Sensors Journal, vol. 7, pp. 586-591, Mar-Apr 2007.

52.   S. Bandyopadhyay, et al., "Ultrahigh-temperature regenerated gratings in boron-codoped germanosilicate optical fiber using 193 nm," Optics Letters, vol. 33, pp. 1917-1919, Aug 15 2008.

53.   J. Canning, et al., "Extreme Silica Optical Fibre Gratings," Sensors, vol. 8, pp. 6448-6452, Oct 2008.

54.   J. Canning, et al., "Regenerated gratings," Journal of the European Optical Society-Rapid Publications, vol. 4, 2009.

55.   E. Lindner, et al., "Arrays of Regenerated Fiber Bragg Gratings in Non-Hydrogen-Loaded Photosensitive Fibers for High-Temperature Sensor Networks," Sensors, vol. 9, pp. 8377-8381, Oct 2009.

56.   Xiao. H., Deng, J., Wang, Z., Huo, W., Zhang, P., Luo, M., Pickrell, G. R., May, R. G., and Wang, A., "Fiber optic pressure sensor with self-compensation capability for harsh environment applications", Opt. Eng. 44, 054403 (2005).

57.   Zhu, Y., Cooper, K. L., Pickrell, G. R., and Wang, A., "High-Temperature Fiber-Tip Pressure Sensor", J. Lightwave Technol. 24, 861 (2006).

58.   Wu, C., Fu, H.Y., Qureshi, K.K., Guan, B. and Tam, H.Y., "High-pressure and high-temperature characteristics of a Fabry-Perot interferometer based on photonic crystal fiber", Optics Letters, 36, 412, (2011).

59.   Fokine, M., "Formation of thermally stable chemical composition gratings in optical fibers," J. Opt. Soc. Am. B, 19(8), 1759-1765 (2002).

60.   Butov, O.V., Dianov, E.M., and Golant, K.M., "Nitrogen doped silica-core fibres for Bragg grating sensors operating at elevated temperatures," Meas. Sci. Technol, 17(5), 975-979 (2006).

61.   Aslund, M., and Canning, J., "Annealing properties of gratins written into UV-presensitized hydrogen-outdiffused optical fiber," Optics Letters, 25(10), 692-694 (2000).

62.   Grobnic, D., Smelser, C.W., Miharlov, S.J., and Walker, R.B., "Long-term thermal stability tests at 1000°C of silica fibre Bragg gratings made with ultrafast laser radiation", Mea. Sci. Technol. 17(5), 1009-1013 (2006).

63.   Groothoff, N., and Canning, J., "Enhanced type IIA gratings for high-temperature operation," Optics Letters, 29(20), 2360-2362 (2004)

64.   Bandyopadhyay, S., Canning, J., Biswas, P., Stevenson, M. and Dasgupta, K., "A study of regenerated gratings produced in germanosilicate fibers by high temperature annealing", Optics Express, 19, 1198, (2011).

65.   Yamate, T., Ramos, R.T., Schroeder, R.J., and Udd, E., "Thermally insensitive pressure measurements up to 300 degree C using fiber Bragg gratings written onto side hole single mode fiber," SPIE Proceddings, Vol. 4185, pp. 628-630, 2000.

66.   Xie, H. M., Dabkiewicz, P., Ulrich, R.,"Side-hole fiber for fiber-optic pressure sensing" Opt. Lett. 11, 333-335 (1986).

67. Kreger, S., Calvert, S., and Udd, E., "High pressure sensing using fiber Bragg gratings written in birefringent side hole fiber" in Optical Fiber Sensors Conference 2002 (Optical Society of America, 2002)

68. Silva-Lopez, M., Li, C., MacPherson, W. N., Moore, A. J., Barton, J. S., Jones, J. D. C., Zhao, D., Zhang, L., and Bennion, I., "Differential birefringence in Bragg gratings in multicore fiber under transverse strain" Opt. Lett. 29, 2225-2227 (2004).

69. Jewart, C., Chen, K. P., Mcmillen, B., Bails, M. M., Levitan, S. P., Canning, J., and Avdeev, I. V., "Sensitivity enhancement of fiber Bragg gratings to transverse stress by using microstructural fibers" Opt. Lett. 31, 2260-2262 (2006).

70. Jewart, C., Xu, D., Chen, K.P. and Canning, J., "Structure optimization of air-hole fibers for high-sensitivity fiber Bragg-grating pressure sensor", SPIE 7004, 2008.

71. Jewart, C., Quintero, S. M., Braga, A. M. B., and Chen, K. P., "Design of a highly-birefringent microstructured photonic crystal fiber for pressure monitoring, " Optics Express, 18(25), 25657 (2010).

72. Jewart, C, Wang, Q., Canning, J., Grobnic, D., Miharlov, S. J. and Chen, K. P., "Ultrafast femtosecond-laser-induced fiber Bragg gratings in air-hole microstructured fibers for high-temperature pressure sensing", Optics Letters, 35, 1443 (2010).

73. T. Chen, R. Chen, C. Jewart, B. Zhang, K. Cook, J. Canning, and K. P. Chen, "Regenerated gratings in air-hole microstructure fibers for high temperature pressure sensing", Opt. Lett. 36, 3542 (2011).

74. D. Oron, N. Dudovich, and Y. Silberberg, "Femtosecond Phase-and-Polarization control for background free Coherent Anti-Stokes Raman Spectroscopy," Physics Review Letters, 90, 213902 (2003).

75. Katz, A. Natan, Y. Siberberg, and S. Rosenwaks, "Standoff detection of trace amounts of solids by nonlinear Raman spectroscopy using shaped femtosecond pulses," Applied Physics Letters, 92, 171116 (2008)

76. S. Roy, P. Wrzesinski, D. Pestov, M. Dantus, and J. R. Gord, "Single-beam coherent anti-stoke Raman scattering (CARS) spectroscopy of gas-phase $CO2$ via phase and polarization shaping of a broadband continuum," Journal of Raman Spectroscopy, 41, 1194-1199 (2010).

77. F. Benabid, J. C. Knight, G. Antonopoulos and P. St. J. Russell, "Stimulated Raman scattering in Hydrogen-filled hollow core photonic crystal fiber," Science, 298 (5592) 399-402 (2002).

78. F. Benabid, F. Couny, J. C. Knight, T. A. Birks, and P. St. J. Russell, "Compact, stable and efficient all-fibre gas cells using hollow-core photonic crystal fibres," Nature, 434, 488-491 (2005).

79.   M. P. Buric, K. P. Chen, J. Falk, and S. D. Woodruff, "Enhanced spontaneous Raman scattering and gas composition analysis using a photonic crystal fiber," Applied Optics, 47, 4255-4261 (2008).

80.   www.nktphotonics.com